CALCULATION OF ADSORPTION ENERGIES IN SLIT-LIKE AND WEDGE SHAPED MICROPORES

J. K. Floess and Yolanda VanLishout
Department of Chemical Engineering
University of Illinois at Chicago
Chicago, Il 60680

Keywords: microporous carbons; adsorption energies; adsorption isotherms

Introduction

The analysis of the structure of microporous carbons has been undertaken using a wide range of techniques. The results of these studies suggest that microporous carbons consist of lamellae present singly or in stacks of two or three turbostratic layers[1]. The lamellae are apparently curved forming larger micropores in the shape of a triangle and small ultra-micropores between adjacent curved lamella or stacks of lamellae. The average diameter of the lamellae is a function of the heat treatment temperature and presumably also the extent of carbon conversion.

The physisorption of gases, although experimentally tedious, probably remains the most versatile method of analysis, and the results of such studies, in large part, form the basis of our understanding of the pore structure of these materials. In our work, we have undertaken to measure[2] the isosteric heats of adsorption of different gases on microporous carbons with the objective of obtaining information on pore size. As is well known, the physisorption of molecules in small pores is enhanced over that of a single surface due to the added attractive force of the second surface. This effect, though, is appreciable only in pores smaller than about 10Å. Consequently, it is possible to use heat of adsorption data to determine the size of the ultramicropores. This approach has been previously used by Everett and Powl[3], who considered adsorption in both slit-like and cylindrical pores, by Stoeckli[4], and by Chihara et al.[6] to determine pore widths in microporous carbons.

The problem with this approach, as pointed out by Wickens[6], is that it is necessary to assume a monosize pore distribution in order to obtain a pore spacing from the isosteric heat. The intention of this study was to determine the adsorption energies for a range of probable pore configurations with the objective of determining a site energy distribution for physisorption. The basic model used in the calculations assumes that the pores are formed by finite sized lamellae having 1 to 3 turbostratic layer planes per surface. Calculations were done as a function of lamellae diameter, pore spacing, the position of the adsorbate molecule, the number of turbostratic layers, and the pore angle.

Model Development

Adsorption energies were calculated by numerically summing the Lennard-Jones potential for the interaction of an adsorbate molecule with each carbon atom in a microcrystallite. The calculations assume that the total adsorption energy can be obtained from the sum of the pair-wise interaction energies between the adsorbate molecule and the individual atoms in the solid. The adsorbate molecule and each atom in the solid are assumed to act as single force centers.

The positions of the carbon atoms in the basal plane were calculated, in polar coordinates, relative to the center of a hexagonal unit in the basal plane. The size of the lamella (the basal plane) is measured by the number of hexagon rings around a central hexagon. A maximum of eight hexagon rings was considered in these calculations. This corresponds to a maximum lamellae (area equivalent) diameter of 38Å. Usually three basal planes were included in the calculation of the adsorption potential for a surface. The position of carbon atoms in the normal direction to the basal plane is not specified for crystallites in a microporous carbon since adjacent basal planes are turbostratically stacked. It was assumed in these calculations that carbon atoms in adjacent layers are stacked directly on top of each other. However, because of the large spacing between adjacent layers (3.4Å) compared to the spacing between atoms in a basal plane (1.42Å along a hexagon edge), the specific stacking arrangement has a negligible effect on the calculated adsorption energy.

Calculations were done for three positions of the adsorbate molecule: above the midpoint of a hexagon (position s); directly over a carbon atom (position c); and above a bond between 2 carbon atoms (position cb).

The Lennard-Jones potential model for the pair-wise interaction is:

$$u(r) = 4\varepsilon_{gs}[(\sigma_{gs}/r)^{12} - (\sigma_{gs}/r)^{6}] \qquad (1)$$

where r is the distance between the adsorbate molecule and a carbon atom in the solid; ε_{gs} is the depth of the potential energy minimum for the pair-wise interaction; and σ_{gs} is the distance at which the pair-wise interaction potential is zero. Values[7] of 7.98×10^{-15} ergs and 3.45 Å were used for ε_{gs} and σ_{gs} in the calculations. Here σ_{gs} is the arithmetic mean of the spacing between basal planes and the distance parameter in the Lennard-Jones potential for the adsorbate molecule (Argon) in the gas phase.

Results

Figure 1 gives the interaction energy of an adsorbate molecule with a single carbon surface of three basal planes as a function of the basal plane size (given in terms of the number of hexagon rings around the central hexagon) and for the three positions of the adsorbate molecule above the surface. For lamella as large or larger than that formed by 4 rings (~20Å in diameter), the adsorption energy is independent of lamella size. Below 20Å, however, the adsorption potential decreases significantly with lamella size. The difference in adsorption energies between the *s* and *c* or *cb* positions is less than 4%, while between the *c* and *cb* positions there is only a very

small difference in adsorption energy. As a result, energy barriers to translational motion of the adsorbate molecule across the surface are small so that physisorbed molecules exist as a mobile film on a graphite surface. Also shown in figure 1 are the interaction energies obtained by integrating the Lennard-Jones potential over a single basal plane and by summing the contribution of individual planes in the direction normal to the basal plane. Steele[7] has shown that the adsorption energy obtained by integration over a single layer plane is nearly the same as summation, provided that $\sigma_{gg}/\sigma_{ss}>1.5$. (Here σ_{ss} is the spacing between atoms in the crystal surface.) However, because of the different atomic spacings in the normal and parallel directions to the basal plane in a graphite crystal, integration in the normal direction does not give an adsorption energy that agrees with summation unless the adsorbate molecule is 1.5 times larger than basal plane spacing. Agreement between the integration and summation calculation and the discrete summation is excellent for lamella larger than ~11Å. Integration, however, does not yield information on the magnitude of energy barriers to translational motion of the adsorbate across the solid surface.

Increasing the number of layers from 1 to 2 layers increases the adsorption energy by less than 10%. Additional layers beyond 2 increase the adsorption energy by approximately 3%.

Figure 2 gives the adsorption energy as a function of pore spacing for a slit-like pore. There are two pore spacings, on each side of the maximum adsorption energy spacing, at which the adsorption energies are equal. These are referred to here as the tight and loose configurations. The maximum interaction energy is obtained at a pore spacing of 6.8Å. For pores wider than 7.7Å, the adsorption potential is a maximum in the pore at two positions, each located 3.4Å from a surface. This is shown in Figure 3, where the adsorption energy is plotted as a function of position in an 8.6Å pore. In pores smaller than 7.7Å, the equilibrium position of the adsorbate molecule will be at the center of the pore.

The adsorption energy in a 6.4Å pore, as a function of the radial position of the adsorbate (i.e. in a direction parallel to the surface) in the pore, is plotted in Figure 4. The calculations show an ~10% difference in the adsorption energies between the *s* and *c* or *cb* positions. Consequently, even in a tight pore configuration, physisorbed molecules are largely mobile. Furthermore, there is no preference for movement over the *c* or *cb* positions. At a slightly wider width of 6.8Å, the difference in adsorption energies between the *s* and *c* or *cb* configurations is 4%, so that adsorbed molecules are almost fully mobile in pores of this size or larger.

Calculations were also done for wedge shaped pores at small angles and for an angle of almost 90°. Figure 5 shows the adsorption energies in a 10° pore for a molecule equidistant from each surface as a function of the lateral position of the molecule in the pore. If the pore angle is small, the maximum interaction energy occurs at the point where the surfaces are ~6.8Å apart (the actual vertical separation between the two surfaces at the maximum interaction energy is 6.9Å). The maximum interaction energy is 2% less than in a parallel pore. The uneven variations in adsorption energy (near the maximum value) occur because the molecule position changes among the *s*, *c*, and *cb* configurations as it is moved into the wedge. The change in adsorption energy with lateral position will depend

on the angle between planes; however, there will always be a position where the interaction energy is at a maximum. This point, though, can reside in a fairly shallow energy well (if the pore angle is small) so that a molecule in a wedge shaped pore may retain a significant degree of lateral mobility. For large pore angles, the adsorbate molecule will not be as mobile; however, the adsorption energy will be less than for a small angle pore since the adsorbate will interact with the edge of least one plane. If the pore angle is formed by the edges of both surfaces, the interaction energy is approximately 25% lower than for the small angle case.

Discussion

The calculations show that the adsorption energy in a micropore depends on a range of factors: the lamella size, the pore spacing and angle, and the number of turbostratic layer planes per surface. The adsorption energies calculated by summation show that physisorbed molecules retain their mobility even in tight pores and that there is a significant degree of lateral mobility in small angle wedge shaped pores. For most other cases, however, the discrete summation method has no particular advantage over the integration method used in previous studies[3,4].

The determination of an average adsorption energy for a molecule in a microporous carbon requires both an estimate of the site energy distribution and information on the fraction of sites of a given energy that are occupied. Presumably, slit-like pores will be uniformly distributed with respect to pore spacing, so that a site energy distribution could be obtained from the data in figure 2. Such a distribution will be skewed towards the maximum adsorption energy. Similarly, small angle wedge shaped pores will also skew the distribution towards the maximum adsorption energy. A site energy distribution calculated from the data in Figure 5 is shown in Figure 6. Large angle wedge shaped pores will only contribute sites with energies some 25% lower than the adsorption energy in small angle pores.

In order to determine the fraction of sites with the same energy that are occupied, the Volmer isotherm equation[8] was evaluated at a number of different adsorption energies. (The pre-exponential factor for the equilibrium constant was obtained from the data of Floess et al.[2]). As shown by the isotherms in figure 7, adsorption in the Henry's Law regime (at 184 K) occurs predominantly on sites with energies above 3.6 kcal. (At lower temperatures, low energy sites will be occupied to a greater extent in the Henry's Law regime.) Nevertheless, since the site energy distribution is also skewed towards high energy sites, adsorption in the Henry's Law regime will occur predominantly in slit-like pores that are approximately 6.8Å wide and in small angle wedge shaped pores. The heat of adsorption in the Henry's Law regime will therefore be principally due to adsorption in these pores, and an average pore spacing calculated from heat of adsorption data will be a weighted average pore spacing for the pores that have the highest adsorption potential.

The calculations also showed that adsorbate molecules are mobile on a carbon surfaces and that they retain a high degree of lateral mobility even in a tight pore configuration. As a result, diffusion in a microporous carbon will depend on the rate of transport from one microporous slit to an adjacent one and not on the rate of

transport in a micropore itself. Therefore, if diffusion is modeled[9] as a molecule jumping from energy well to energy well over a potential barrier, the potential barrier will be that for adsorption in a micropore and the distance between energy wells will be proportional to the average lamella diameter in a microporous carbon.

References
1. McEnaney, B. *Carbon*, 1988, 26, 267.
2. Floess, J. K.; Kim, H. H.; Edens, G.; Oleksy, S. A.; Kwak, J., *Surface Area and Pore Size Measurements of Microprous Carbons*, paper presented at the AIChE National Meeting, Chicago, IL, November, 1990.
3. Everett, D. H.; Powl, J. C. *J. Chem Soc., Faraday Trans. I*, 619 (1976).
4. Stoeckli, H. F. *Helv. Chim., Acta*, 1974, 57, 2194.
5. Chihara, K.; Susuki, M.; Kawazoe, K. *J. Colloid and Interf. Sci.*, 1978, 64, 584.
6. Wickens, D. A. *Carbon*, 1990, 28, 97-101.
7. Steele, W. A., *The Interaction of Gases with Solid Surfaces*, Pergamon Press: Oxford, 1974.
8. Ross, S.; Olivier, J. P. *On Physical Adsorption*, John Wiley: New York,1964.
9. Boudart, M.; Djega-Mariadassou, G. *Kinetics of Heterogeneous Catalytic Reactions*, Princeton University Press: Princeton, NJ, 1984.

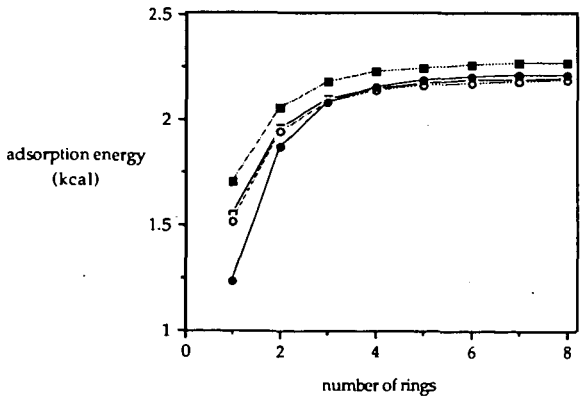

Figure 1. Adsorption energy as a function of lamella diameter: (■) s position; (○) c position; (□) cb position; (●) integral-sum calculation.

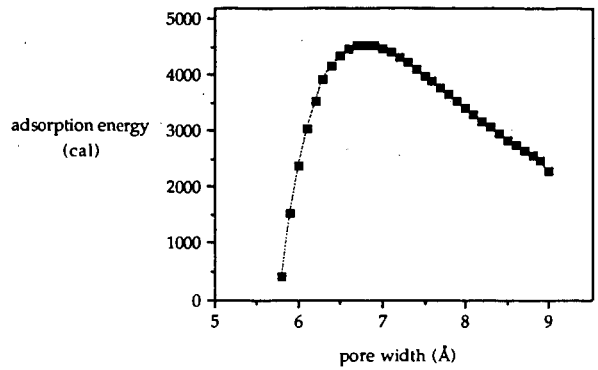

Figure 2. Adsorption energy as a function of pore width.

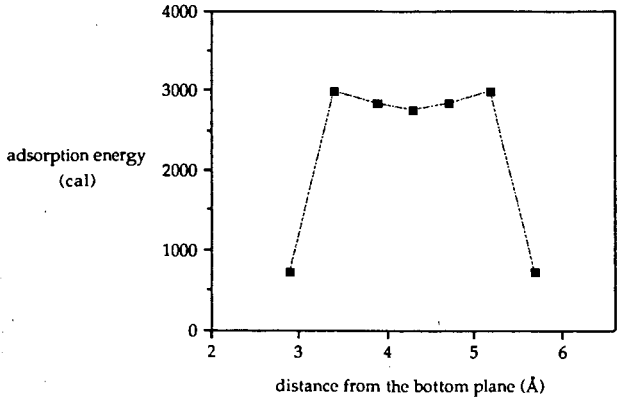

Figure 3. Adsorption energy as a function of adsorbate position in a 8.6 Å pore.

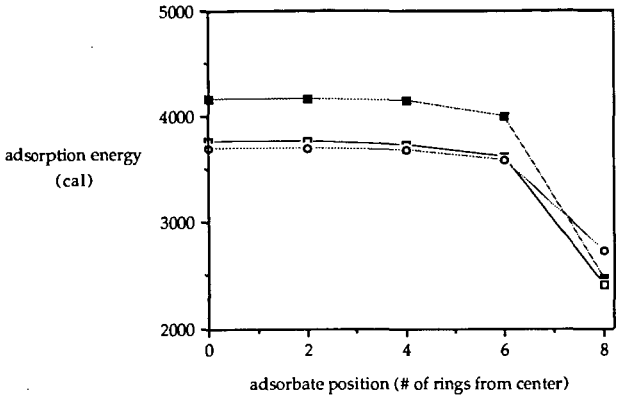

Figure 4. Adsorption energy as a function of the radial position of a molecule in a slit-like pore. Pore width: 6.4Å; (■) s position; (○) c position; (□) cb position.

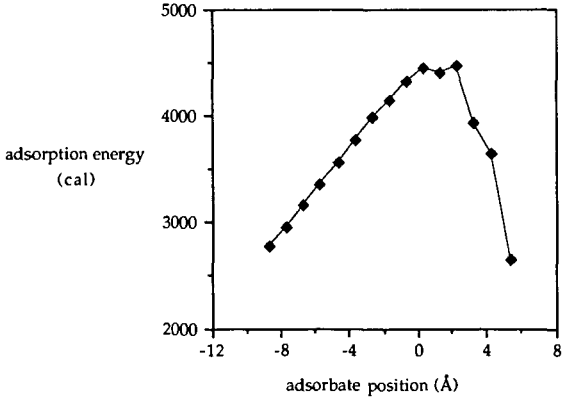

Figure 5. Adsorption energy as a function of position in a 10° pore. (0 = center of lamella; positive direction is into the angle; adsorbate equidistant from both planes.

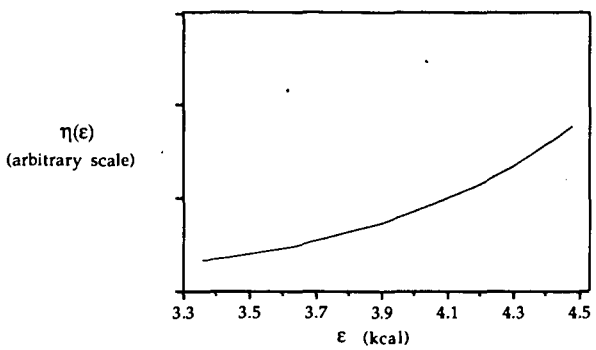

Figure 6. The density of the site energy distribution in a 10° wedge shaped pore.

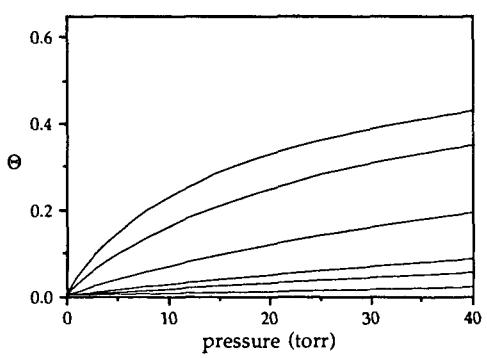

Figure 7. Volmer adsorption isotherms at 184 K for sites with adsorption energies of 4.4, 4.0, 3.6, 3.2, 3.0, and 2.6 kcal (curves from top to bottom).

A Transient Kinetic study of the Gasification of Carbon in CO_2.

F. Kapteijn, R. Meijer and J.A. Moulijn*.
Department of Chemical Engineering, University of Amsterdam
Nieuwe Achtergracht 166, 1018 WV, Amsterdam, The Netherlands.
* *at present: Department of Chemical Technology, University of Delft*

Keywords: transient kinetics, CO_2 gasification, carbon

ABSTRACT

A transient kinetic study, using labelled CO_2, has been conducted on the gasification of carbon in CO_2. Step-response (SRE) and temperature programmed desorption (TPD) experiments indicate that during steady state gasification at least two types of oxygen complexes are present at the carbon surface, both yielding CO. Upon exposure to an inert gas at gasification temperatures the decomposition of one of these complexes is fast and decays within seconds, whereas the other lasts for several minutes. However, both contribute to the overall gasification activity. Moreover, from the presence of ^{13}CO in both SRE and TPD experiments it is concluded that CO chemisorption or insertion takes place. A mechanism for the gasification reaction in CO_2 is proposed in which stable carbon-oxygen complexes can be transformed into the more reactive complexes, and in which CO insertion is included.

INTRODUCTION

The kinetics of carbon and coal gasification have been extensively studied. In most studies the rate of gasification is measured and interpreted under specified conditions. From both a practical and theoretical point of view it would be highly desirable if a method existed by which, independent of carbon type, heat treatment history or burn-off, the rate parameters which govern the gasification process could be determined.

Temperature programmed desorption (TPD) and step-response experiments (SRE), two commonly applied techniques in the field of heterogeneous catalysis, are increasingly used to determine the rate parameters and the total number and stability of active carbon-oxygen complexes present during steady state gasification of carbonaceous materials. Kapteijn and Moulijn [1] already outlined the possibilities of these transient techniques, compared to steady state measurements, in studies concerning (catalysed) carbon gasification. This experimental approach is gaining a lot of attention [2-7].

A step change in the gas phase composition at reaction temperatures, *i.e.* from a reactive to an inert gas flow and *vice versa* or from one reactive to another (labelled) reactive gas flow and analysis of the response curves of the sample under investigation, provides information on the reaction, *viz.* the amount and stability of carbon-oxygen complexes and rates of elementary processes.

An important feature of applying $^{13}CO_2$ is that it enables us to distinguish between ^{13}CO produced by gas phase oxidation of the active carbon sites and CO production originating from the carbon structure. The assumption in this two-step model (eqs.1,2) that equation (2) is the rate determining step can easily be confirmed by a gas phase step change from $^{13}CO_2$ to an inert at gasification temperature; a fast declining ^{13}CO production is accompanied by a long tailing CO production.

$$CO_2 + C_f \underset{k_{-1}}{\overset{k_1}{\rightleftharpoons}} CO + C(O) \qquad (1)$$

$$C(O) \xrightarrow{k_2} CO + C_f \qquad (2)$$

A gas phase step change from $^{13}CO_2$ to Ar will show if desorbing CO is capable of picking up a surface oxygen by reversed reaction (1) ($^{12}CO_2$ formation) and if during gasification insertion of gas phase CO has taken place, which is the case if a tailing ^{13}CO production is observed.

The most important feature of step-response experiments between $C^{18}O_2$ and CO_2 is that it provides a means to trace and quantify all reactive oxygen present on the carbon sample, while maintaining steady state gasification conditions.

The aim of this study was to obtain a more detailed description for the mechanism of the carbon gasification reaction, thus providing a sound basis for the selection of a kinetic model and its derived rate expression. In this paper results are presented of transient kinetic gasification experiments (1200–1250 K) with (labelled) CO_2, together with TPD experiments after partial gasification. These results and their implications with respect to the mechanism of the gasification reaction are discussed.

EXPERIMENTAL

Throughout this paper all labelled species are addressed with a prefix, *viz.* ^{18}O and ^{13}C, whereas in all cases C and O without prefix refer to ^{12}C and ^{16}O.

Reactants/samples

The model carbon used in this study is Norit RX1 Extra, an acid washed, steam activated peat char with a high specific surface area [6].
All gases used were of HP or UHP grade and are purified (O_2 and/or H_2O removal) before being fed to the gas mixing sections. $^{13}CO_2$ and $C^{18}O_2$ were used as received (99% pure ^{13}C and 90–91 % pure ^{18}O, MSD Isotopes) and mixed with Ar in lecture bottles. The O present in the $C^{18}O_2$ feed is present as $CO^{18}O$ (≈ 20% of the total CO_2).

Apparatus

The kinetic equipment, described in detail elsewhere [6], basically consists of three gas mixing sections. By means of a pneumatically actuated four-way valve in SRE two selected gas flow lines can be exchanged instantaneously and isobaric over the carbon sample.
The product gas is analysed by GC and by MS. Signal analysis, mass selection and sampling rate are controlled by a personal computer, equipped with Analog Devices RTI cards, through which data were collected and stored for further quantitative analysis. Up to 12 m/e values can be scanned consecutively with a minimum delay of 47 ms per m/e value. The raw MS data are corrected for background levels, fragmentation contributions (CO_2 to CO) and MS sensitivity for the different molecules. Quantitative interpretation of the step-response curves was performed by comparison with a gas phase step change performed over an inert SiC sample under exactly the same experimental conditions. These blanc runs exhibit the same response curves for CO_2 and showed that under reaction conditions the equipment had a time constant (the time to fall to 1/e of the inital step change) of less than 1 s. Thus the rate processes with larger time constants, *i.e.* with rate constants smaller than 1 s^{-1}, can be determined.

Experimental procedures

Step-response and steady state gasification experiments were performed at 1200 and 1250 K with, unless stated otherwise, a carbon sample of initially 100 mg and a flow rate of 20 $\mu mol.s^{-1}$. In order to obtain a reproducible carbon sample each sample was dried *in situ* (T = 423 K, He) and was gasified at 1200 K up to approximately 20 % burn-off.
All step-response experiments were performed several times in order to check their reproducibility. The response curves after a gas phase step change from CO_2,Ar to Ar and *vice versa* were investigated as a function of temperature (1200–1250 K), partial pressure of CO_2 (4 – 100 % CO_2) and carbon burn-off (20–50%).

In some cases at the end of the step-response or gasification experiment a temperature programmed desorption (TPD) in helium, in order to characterise the sample by its desorption products, was performed. TPD was done with a heating rate of 10 $K.min^{-1}$ up to 1273 K, followed by an isothermal period of 10 min at 1273 K. The amounts of CO released, expressed as mol CO.mol $C_a^{-1}.s^{-1}$, are plotted as a function of temperature. During TPD experiments none or a negligible amount of low temperature CO_2 desorption was observed, which, for clarity, is not shown in the figures.

RESULTS AND DISCUSSION

After a gas phase step change from 10% $^{13}CO_2$,Ar to Ar at 1200 and 1250 K, besides CO also ^{13}CO production is observed (figure 1). In both cases $^{13}CO_2$ disappears nearly instantaneously and the total CO production ($CO+^{13}CO$) immediately drops to about half the steady state value and exhibits a fast continuing decay in the first ten seconds, followed by a tailing that lasts for several minutes, which is mainly due to CO. This behaviour is observed after all gas phase step changes from a reactive to an inert gas phase at gasification temperatures.
These results indicate that ^{13}CO is inserted or chemisorbed at the carbon surface [9–11], and is released in two distinct ways. The CO production could only be described by two different parallel desorption processes. A single exponential decay or Elovich type desorption [8] were unable to do so.

In figure 2 the response curves for different gas phase step changes involving $C^{18}O_2$ at 1200 K are shown. A gas phase step change from $C^{18}O_2$ to Ar shows a tailing $C^{18}O$ production (figure 2B, insert), similar to the results of figure 1. A step change to CO_2 results in a sharp $CO^{18}O$ production peak and a decaying $C^{18}O$ production that disappears earlier (figure 2A) than upon exposure to an inert. The total $CO + C^{18}O$ production remains constant, indicating no disturbance of the steady state gasification. A blanc experiment with a SiC bed (figure 2C) shows that the sharp $CO^{18}O$ production peak in the initial seconds after the step change, when both $C^{18}O_2$ and CO_2 are present, must be ascribed to gas phase exchange through eq.(3).

$$CO_2 + C^{18}O_2 \rightleftharpoons 2\ CO^{18}O \qquad (3)$$

The longer tailing $CO^{18}O$ evolution in figure 2A compared to that in figure 2B indicates that CO, produced by CO_2 gasification, picks up ^{18}O from the carbon surface, confirming the reversibility of reaction (1). The faster disappearance of $C^{18}O$ by a step change to CO_2 instead of Ar is only partially explained by this removal, since it is also observed in the case of SRE with $^{13}CO_2$. Apparently, the presence of CO_2 speeds up the release of CO. The released amounts of CO are given in table 1 and 2.

TPD patterns obtained after steady state gasification at 1200 K in various CO_2,Ar mixtures and cooling to 673 K (figure 3), all show CO desorption above 1000 K, which can be ascribed to the decomposition of carbon–oxygen complexes from the carbon surface. In all cases the total amount of CO desorption observed during TPD upto 1273 K exceeds the amount of CO produced after a gas phase step to an inert at 1200 K (table 3).
From the CO desorption patterns after gasification in pure CO_2 at 1200 K and assuming irreversible first-order desorption, an activation energy of 213 kJ.mol^{-1} (k_0N_{CO} = 6.6 10^3 mol.mol C_a^{-1}.s^{-1}) is calculated (figure 3A), for the fractional coverage range between 0.3 to 0.9. If after TPD the carbon sample is exposed to CO at 373 K in a subsequent TPD (figure 3B) again a considerable CO desorption is observed, but with a lower activation energy (E_a = 160 kJ.mol^{-1}, k_0N_{CO} = 11.4 mol.mol C_a^{-1}.s^{-1}), indicating a weaker interaction.
It is striking that during TPD after gasification in $^{13}CO_2$ (figure 3C) above 1000 K ^{13}CO desorption is observed, indicating that during gasification in $^{13}CO_2$ insertion of ^{13}CO has taken place, confirming the SRE results. The $C^{18}O$ desorption, which is observed in TPD after gasification in $C^{18}O_2$ followed by that in CO_2 (figure 3D), indicates that not all oxygen present on the carbon surface is actively taking part in the gasification reaction. The amount of $C^{18}O$ desorption is higher after the reversed gasification order.

In summary the most important observations are *(i)* two CO desorption rates are operative, *(ii)* CO can be inserted or adsorbed on the carbon, yielding both types of desorption, *(iii)* oxygen is removed from the surface by reaction with CO, *(iv)* CO_2 enhances the CO desorption process.
This led us to the following tentative proposal for the gasification mechanism. Reaction (1) yields semiquinone structures [12,13] at the zig–zag (II) or armchair (V) edges of the graphitic carbon planes by interaction of the CO_2 with the active sites (unsaturated carbons, not terminated with hydrogen). Decomposition of this structure yields the slow desorbing CO. At the armchair edges an adjacent site can also be oxidised, yielding a diketone (IX). This is more unstable than the

semiquinone and readily breaks open resulting in two adsorbed CO molecules, carbonylic structures (X). These represent the faster CO desorption species. The release of the CO molecules is in both cases assumed to be reversible, accounting for the observed CO insertion or chemisorption. Only in the presence of CO_2 the diketone structures will be formed continuously, and part of the semiquinone structures on the armchair edges are transformed into the faster desorbing CO species. This process might explain the discrepancy that was noticed between steady state gasification rates and those calculated on the basis of rate constants and surface occupancy obtained from step response experiments [7].

The SRE results presented here agree with the TPD analysis of Magne and Duval [14], who observed four types of CO release: two easily and two less easily decomposing surface complexes, yielding CO. Apparently, our results can only discriminate between the two groups.

$$CO_2 + C_f \rightleftharpoons CO + C(O) \quad (1)$$

$$CO_2 + C_f\text{-}C(O) \rightleftharpoons CO + 2\,C\text{-}(CO) \quad (4)$$

$$C\text{-}(CO) \overset{k_a}{\rightleftharpoons} CO + C_f \quad (5)$$

$$C(O) \overset{k_b}{\rightleftharpoons} CO + 2\,C_f \quad (2)$$

II

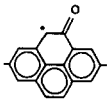

V

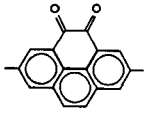

IX

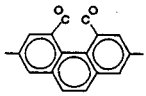

X

ACKNOWLEDGEMENT

The financial contribution of the Dutch Organization for the Advancement of Pure Research (NWO-SON), enabled the purchase of the labelled compounds.

These investigations have been executed within the framework of the Dutch National Coal research Programme (NOK), which is managed by the Project Office for energy Research (NOVEM) and financed by the Ministry of Economic Affairs.

REFERENCES

1. Kapteijn F., and Moulijn J.A., in *Carbon and Coal Gasification: Science and Technology*, eds. J.L. Figueiredo and J.A. Moulijn, NATO ASI Series E: Appl. Sci. vol. 177, Marinus Nijhoff Publ., Dordrecht, 291 (1986).
2. Huttinger K.J., *Carbon*, 28, 453 (1990).
3. Lizzio A.A., Jiang H., and Radovic L.R., *Carbon*, 28, 7 (1990).
4. Zhu Z.-B., Furusawa T., Adshiri T., and Nozaki T., *ACS Div. Fuel Chem. Prepr.*, 32, 132 (1987).
5. Huttinger K.J., and Nill J.S., *Carbon*, 28, 457 (1990).
6. Kapteijn F., Meijer R., and Moulijn J.A., in "*Fundamental Issues in Control of Carbon Gasification Reactivity*", eds. J. Lahaye and P. Ehrburger, NATO ASI Series E: Appl. Sci. vol. 192, Kluwer, 221 (1991).
7. Mc Enaney B., in "*Fundamental Issues in Control of Carbon Gasification Reactivity*", eds. J. Lahaye and P. Ehrburger, NATO ASI Series E: Appl. Sci. vol. 192, Kluwer, 1751 (1991).
8. Bonnetain L., *J. Chim. Phys.*, 34 (1961).
9. Bonner F., and Turkevich J., *J. Am. Chem. Soc.*, 73, 561 (1951).
10. Brown F., *Trans. Faraday Soc.*, 48, 1005 (1952).
11. Orning A.A., and Sterling E., *J. Phys. Chem.*, 58, 1044 (1954).
12. Marchon B., Tysoe W.T., Heinemann H. and Somorjai G.A., *J. Phys. Chem.*, 92, 5744 (1988).
13. Marchon B., Carrazza J., Heinemann H. and Somorjai G.A., *Carbon*, 26, 507 (1988).
14. Magne P. and Duval X., *Carbon*, 11, 475 (1973).

Table 1 : The total amount of CO production, relative to the amount of carbon actually present, observed after a gas phase step change from CO_2 to Ar at 1200 K as a function of carbon burn-off, together with the gasification rate, r_w, and the average rate constant for CO desorption

Burn-off (%)	N_{CO}/C_a mol.mol^{-1}	r_w mol.mol^{-1}.s^{-1} (* 10^4)	k_{mean} s^{-1}
20	0.0028	1.53	0.055
35	0.0026	1.55	0.060
45	0.0030	1.58	0.053

Table 2 : Total amounts of desorption products (μmol) observed after a gas phase step change from various CO_2,Ar mixtures to Ar at gasification conditions (sample sizes 30-80 mg carbon actually present).

gasification conditions		CO	^{13}CO	$C^{18}O$
CO_2	1200 K	20.8	-	-
$^{13}CO_2$	1200 K	17.4	4.3	-
10% $^{13}CO_2$,Ar	1250 K	4.7	1.4	-
	1200 K	2.4	0.4	-
4% $C^{18}O_2$,Ar	1200 K	-	-	6.2
$C^{18}O_2$	1200 K	-	-	11.1

Table 3 : Total amounts of desorption products, relative to the amount of carbon actually present (mol/mol), observed in TPD up to 1273 K after different treatment at 1200 K:

treatment	CO/C_a	$^{13}CO/C_a$	$C^{18}O/C_a$
SSG (CO_2)	0.0042	-	-
SSG ($^{13}CO_2$)	0.0038	0.0005	-
SSG (4% $C^{18}O_2$,Ar - 7% CO_2,Ar)	0.0010	-	0.0001
SSG (7% CO_2,Ar - 4% $C^{18}O_2$,Ar)	0.0007	-	0.0004
CO at 373 K after TPD	0.0015	-	-

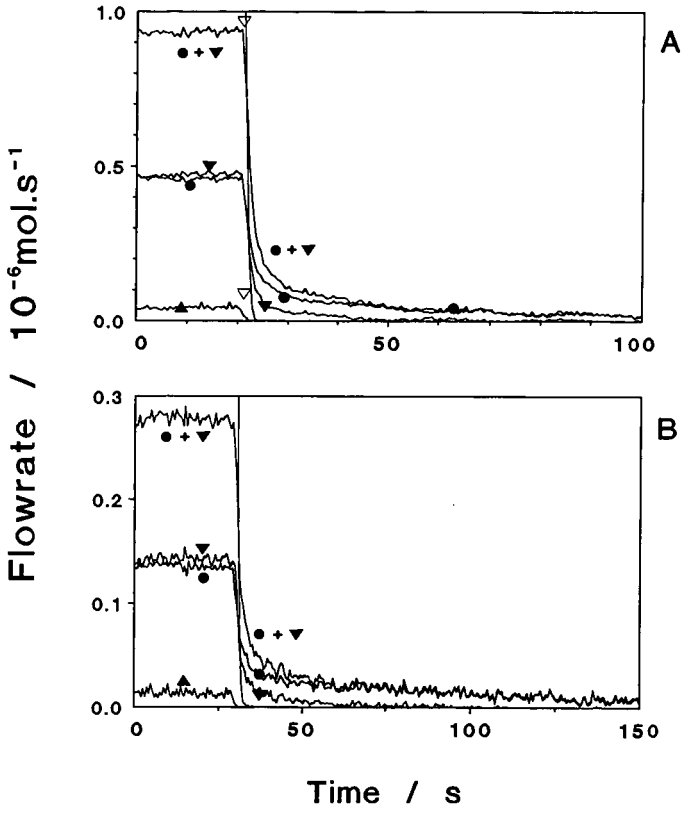

Figure 1 : Response curves after a gas phase step change from 10 % $^{13}CO_2$,Ar to Ar at different temperatures.
A. T = 1250 K; B. T = 1200 K.
Key: CO; ^{13}CO; $C^{18}O$; CO_2; $^{13}CO_2$; $CO^{18}O$; $C^{18}O_2$.

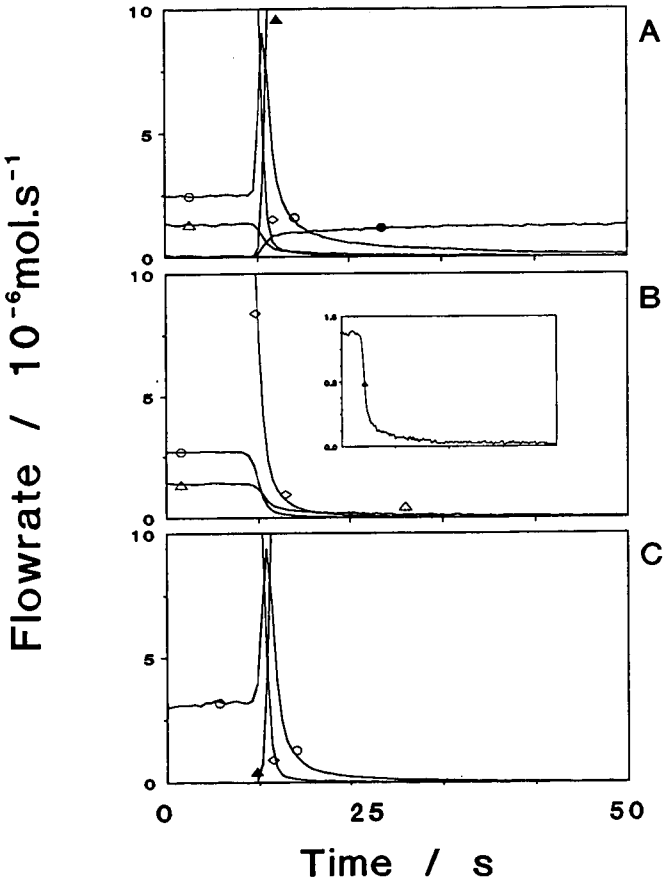

Figure 2 : Response curves after gas phase step changes at 1200 K:
A. $C^{18}O_2 \rightarrow CO_2$ (Norit)
B. $C^{18}O_2 \rightarrow Ar$ (Norit)
C. $C^{18}O_2 \rightarrow CO_2$ (SiC)
(key as in figure 1).

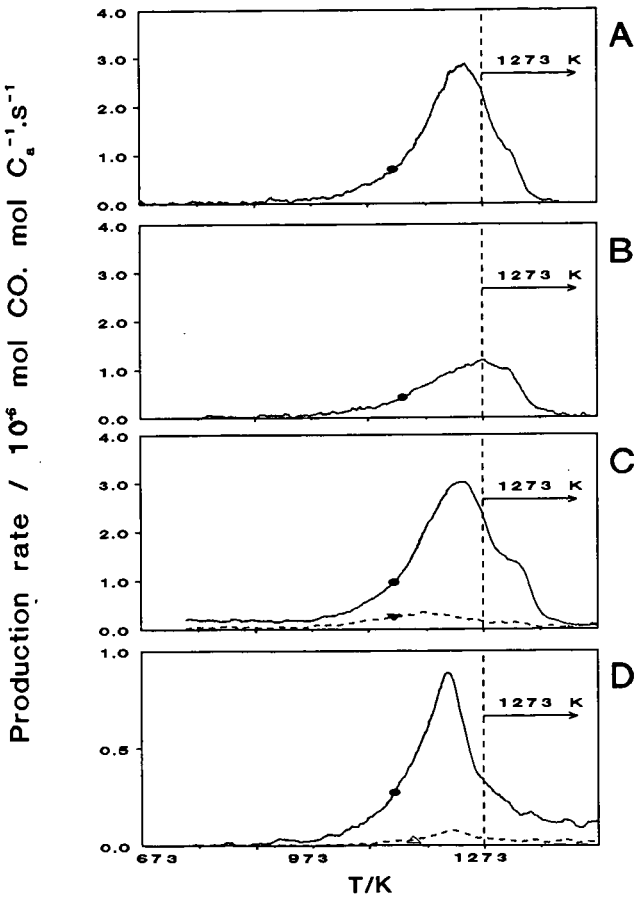

Figure 3 : TPD pattern after different treatments (key as in figure 1):
A. SSG 1200 K in CO_2;
B. TPD – CO at 373 K
C. SSG 1200 K in CO_2 followed by $^{13}CO_2$
D. SSG 1200 K in 4% $C^{18}O_2$,Ar followed by 7% CO_2,Ar.

THE ROLE OF ACTIVATED DIFFUSION IN THE GASIFICATION OF POROUS CARBONS/CHARS

J.M. Calo and M.T. Perkins
Chemical Engineering Program
Division of Engineering
Brown University
Providence, Rhode Island 02912

Keywords: Activated diffusion; mass transfer resistance; CO_2 gasification.

INTRODUCTION

The reaction rates of CO_2, steam, and hydrogen with carbonaceous solids are quite slow, such that the mass transport rate by ordinary bulk diffusion and/or Knudsen diffusion is usually more than sufficient to prevent the reaction from becoming mass transport-limited. Therefore, at first glance the issue of mass transport limitations seems to be relatively unimportant insofar as these reactions are concerned. However, the most reactive carbons are typically those with the highest internal surface areas, and thus it follows that transport in these materials must occur for the most part in pores of molecular dimensions; i.e., micropores. Transport of molecular species into or within micropores does not occur by ordinary bulk diffusion, nor even entirely by Knudsen diffusion. In this case, the energy of interaction between the solid and the gas phase species controls the process. This type of diffusion typically exhibits an Arrhenius-type temperature dependence, and in magnitude is usually slower than Knudsen diffusion. This behavior has been variously known as activated, micropore, intracrystalline, configurational, and surface diffusion [1]. Even though these terms are often used interchangeably in the literature, they may also refer to completely different mechanisms in different systems.

In the current paper we present some measurements of effective diffusion times in coal chars obtained using a transient technique, and analyze the results in terms of their potential effect on CO_2 gasification reactivity.

EXPERIMENTAL

The apparatus for measuring the effective diffusion times consists of: (1) a continuous gas flow, fixed solids, "gradientless" reactor, for carrying out the reaction under well-mixed conditions; (2) a solenoid/control valve network for generating step function changes in feed composition under conditions of constant flow rate, temperature, and pressure; (3) a supersonic molecular beam mass spectrometer system for measuring the transient response of the gas phase composition in the reactor effluent; and (4) a microcomputer for automated data logging and mass programming of the mass spectrometer [2]. In the current work, the highest operating temperature was 1273K and the highest pressure was 90 psig, although most of the data were obtained at a pressure of 30 psig. The reactor space time could be varied from about 0.01 to 2.0 min.

Sample Preparation.

Buller coal (New Zealand, medium volatile bituminous) activated char samples were supplied by Sutcliffe-Speakman Carbons Ltd. of Lancashire, England. The three other coals used in this study (PSOC-467 [Deadman #2] subbituminous, PSOC-833 [Fort Union Bed] lignite, and Wyodak subbituminous) were pyrolyzed in a tube furnace in ~50g batches at 1000°C under UHP nitrogen. Chars from the same coal produced in different batches were mixed. This large sample was divided up into reactor sample aliquots of 60-80g, and smaller characterization samples. The chars were sieved to a mean particle size of 1.6 mm. This size was selected primarily because it ensures complete retention

of the sample in the basket during operation, and yet provides minimal pressure drop through the sample bed. In addition, a mean particle size of 0.8 mm yielded results similar to those for 1.6 mm particles; i.e., ±5% for CO_2 diffusion in PSOC-467; therefore, additional particle size tests were not conducted. Once loaded in the sample basket, the chars were heated to 150°C for one hour to remove adsorbed water vapor.

Experimental Procedures.

A typical experiment was conducted as follows. The sample (60-80 cm^3) was placed in the sample basket, and positioned in the Berty reactor. A sheath-type thermocouple was inserted into the sample bed, and another was located in the free gas volume of the reactor. The reactor was then sealed and purged with argon. The reactor furnace was then turned on. After attaining operating temperature, the solenoid valve gas addition circuit was used to introduce the gas of interest as a step function change in concentration. The flow rates of the different gases were balanced such that the pressure in the reactor remained constant during the transient experiment. The reactor effluent concentration was then continuously monitored with the mass spectrometer, and the data were logged automatically. Runs typically required less than four minutes, following which the reactor was quickly refilled with argon using the gas addition flow circuit.

DATA ANALYSIS PROCEDURE

The experiment generates a time-concentration trace of the reactor effluent. A variety of analysis techniques were investigated to extract diffusion information from these data. A "difference" technique was finally selected. It is based on the "difference" variable, $\Delta C = C\text{-}C^*$, where C and C* are the time-dependent concentrations in a well-mixed reactor both without and with a porous material sink present. The corresponding differential mass balance is given by:

$$\frac{\partial \Delta C}{\partial t} = -\frac{\Delta C}{\tau} + 3\frac{D_e}{R^2}\frac{\partial C^\dagger}{\partial r}\left(\frac{V_s}{V_g}\right)(1-\varepsilon_b)(1-\varepsilon_m), \qquad [1]$$

where t is time, τ is the reactor space time at reactor conditions, R^2/D_e is the effective diffusion time within the char, $V_{s,g}$ are the solids bed and free gas volumes within the reactor, respectively, $\varepsilon_{b,m}$ are the external bed and intraparticle macropore void volumes, respectively, and $\partial C^\dagger/\partial r$ is the dimensionless concentration gradient at the surface of the microporous regions (assumed to be spherical). When ΔC is a maximum, $\partial \Delta C/\partial t = 0$, and Eq. [1] becomes:

$$\frac{\Delta C^{max}}{\tau} = 3\frac{D_e}{R^2}\frac{\partial C^\dagger}{\partial r}\left(\frac{V_s}{V_g}\right)(1-\varepsilon_b)(1-\varepsilon_m) \text{ at } t=t^{max} \qquad [2]$$

This expression requires the specification of $\partial C^\dagger/\partial r$ at the external surface of the "microparticle." This was estimated by the analytical expression for the gradient at the surface of a spherical particle driven by a "gradientless" reactor with the same space time [3]; *viz.*,

$$\frac{\partial C^{\dagger}}{\partial r}\Big|_{r=1} = e^{-t/\tau}\left(1 - \frac{R^2}{\tau D_e}\cot\left\{\frac{R^2}{\tau D_e}\right\}^{1/4}\right) - 2\left(\frac{R^2}{\tau D_e}\right)\sum_{n=1}^{\infty}(-1)^n \frac{e^{-D_e n^2\pi^2/R^2}}{\left(n^2\pi^2 - \frac{R^2}{\tau D_e}\right)} \qquad [3]$$

An iterative approach is required to solve the resultant Eq. [2] for R^2/D_e. Subsequently, the forcing function was generated from the data itself for an improved approximation.

In Figure 1 are presented some representative data for CO diffusing into PSOC-833 coal char at 285°C and 30 psig. The response of a hypothetical run at the same reactor space time with no porous char mass sink (i.e., C) is also presented, as well as the difference curve, ΔC. The maximum is located at $C/C_o = 0.25$ and t=33 s. Next, the data were fit to the expression $[1-\exp(-t/\tau_{eff})]$ to find τ_{eff}. For the data in Figure 1, the best fit is for $\tau_{eff} = 42.1$ s ($\tau = 25.9$ s). The resultant simple rising exponential expression is then used as the external forcing function to find the concentration gradient at the microparticle external surface. The best fit value of R^2/D_e is then found *via* an iterative search. For the data presented in Figure 1, the best fit value was $D_e/R^2 = 0.0134$ s^{-1}.

RESULTS AND DISCUSSION

Characteristic Diffusion Time Results.
All the results exhibited an increase in effective diffusivity with temperature. However, in general, the Arrhenius plots of the results were not very linear. Much of the data indicated a concave downward curvature which could be indicative of a change in mechanism of the transport mechanism with temperature. "Best fit" Arrhenius parameters over the entire temperature range are presented in Table I. As shown, the measured activation energies range from about 0.1 to 1.8 kcal/mole. The apparent activation energy of CO_2 was typically the largest of the gases studied in each coal char.

For a Wyodak coal char, Debelak [4] reported values for CH_4 varying from 0.9 - 3.2 kcal/mol, and values for CO_2, CO, and N_2 from 0.5-2.6 kcal/mol, over a temperature range of 50 to 250°C. A comparison of the current results for CO_2 diffusion in pre-oxidized (with air) Wyodak with the corresponding results of Debelak [4] is presented in Figure 2. Since high temperature surface cleaning, nor oxygen chemisorption in air were performed in the latter work, the actual state of the surface is uncertain. However, both sets of data still agree reasonably well. The observed differences are attributed to the different modes of burn-off (i.e., in CO_2 *vs.* O_2), which may have resulted in different porosity morphologies.

The magnitudes of the apparent activation energies from the current data are relatively low, which in some cases might be due to the influence of Knudsen diffusion. Arrhenius plots of Knudsen diffusivities ($D_K \alpha T^{1/2}$) exhibit a noticeable upward curvature, with the slope increasing with temperature. The PSOC-467 coal char had the largest mean pore radius of the coal chars examined. However, the Arrhenius plots for CO and CO_2 diffusion in PSOC-467 did not exhibit an increasing negative slope with temperature, characteristic of Knudsen diffusion. Thus, it is concluded that Knudsen diffusion was not dominant over the entire temperature range examined.

The Effect of Pressure.
Figure 3 demonstrates the effect of CO_2 pressure on the apparent diffusivity of CO_2 in PSOC-833 coal char at 285°C. As shown, there is a marked *decrease* in apparent diffusivity with increasing pressure for CO_2 pressure. In terms of classical models for activated diffusion, this is consistent with an

occluded gas model where diffusion occurs on the surface by jumping from one adsorption site to another [5]. Increasing pressure tends to populate the adsorption sites, thereby decreasing the diffusion rate.

The Effect of Burn-Off.
Samples of the Wyodak coal char were burned-off in an air fluidized bed at 300°C for intervals of about 2 hours. In between runs, the samples were weighed, and the burn-off determined. The effective surface areas for the Wyodak coal char increased with burn-off, attaining 518 m^2/g (by CO_2 BET; 450 m^2/g by N_2 BET) for the 30% burn-off sample.

As shown in Table I, E_D for the three gases generally seem to increase with burn-off, although this is not a universal trend. At the lower burn-offs in oxygen, the Wyodak coal char develops microporosity with burn-off, but the pore size distribution does not change radically [2]. However, simultaneously the remaining mineral matter is continually being concentrated at pore walls. This effect is known to enhance specific reactivity in chars with catalytic mineral matter impurities [6]. If a diffusing gas interacts strongly with the mineral matter, then this could explain the general activation energy increase with burn-off. This hypothesis is not supported by the slightly higher apparent activation energies observed for CO_2 and CH_4 in the "0% burn-off" demineralized Wyodak coal char. However, the demineralization procedure [7] is known to significantly affect the porosity, and thus a better comparison might be with a higher burn-off sample. Thus, it is noted that all three E_D values are higher for the 10.1% burn-off sample than the demineralized sample, although this result is not conclusive.

The sharp decrease in E_D for CO evident at 30% burn-off may be due to the measured shift of the pore size distribution towards larger pore radii for this char sample [2]. CO, being the smallest of the three molecules may be the most sensitive to the microporosity morphology.

Mass Transfer Limitations.
In order to explore the potential effect of mass transfer resistance on reactivity, a classical "effectiveness factor" (η) analysis was performed. CO_2 gasification reactivities were measured for the four coal chars investigated in a thermogravimetric apparatus (TGA) under 0.1 MPa of CO_2. A simple first order rate expression was assumed for the rate form. Initially, assuming no mass transport resistance (i.e., $\eta = 1$), the Thiele modulus, $\phi = [\{k_1/(D_e/R^2)\}^{1/2}]/3$ (k_1 is the first order rate constant), can be calculated from the measured reaction rate and the effective diffusion time. (For temperatures higher than those for which data were obtained, D_e/R^2 values were extrapolated using the measured apparent activation energy.) Knowing ϕ, η can be determined from the well-known analytical expression, $\eta = 1/\{1/\tanh(3\phi) - 1/(3\phi)\}$. This value can then be used to correct ϕ, and the process is iterated until η and ϕ agree.

The resultant effectiveness factors determined for the coal chars investigated, over a temperature range of 1073-1173K, are presented in Figure 4. As shown, $\eta < 1$ for all the coal chars, and $\eta \ll 1$ at 1173K, indicating almost complete mass transport control under the latter conditions. The most severely transport-limited char is the Buller (activated) coal char, while the least affected are the PSOC-833 and PSOC-467 coal chars. This is consistent with the fact that the activated Buller coal char was the most microporous, while the PSOC samples were the least microporous, since they experienced little burn-off. As might be expected, the Wyodak samples at progressive burn-offs were intermediate between these two extremes.

CONCLUSIONS

Activated transport through microporous coal chars does not appear to be generally describable by a single simple model. The behavior depends on the diffusing species and char porosity morphology and composition, as well as surface site occupancy [2]. For the results that exhibited a pressure effect, the occluded phase model appears to be more applicable. However, some of the results exhibited a decrease in apparent activation energy at high temperatures that is characteristic of two-phase model behavior. Most of the results exhibit behavior somewhere in between these two extremes. Thus, the actual mechanism is likely to be a combination of these two processes, and, possibly, others (e.g., Knudsen diffusion) as well.

The reaction of CO_2 with coal char should be mass transport-controlled in the microporosity for all the coal chars examined at temperatures greater than about 800°C, with $\eta < 0.2$ for all the samples under these conditions. In addition, the the CO_2 reactivity of Wyodak coal char would still appear to be mass transport-limited up to 30% burn-off.

Acknowledgements. This work was supported by the Department of Energy under Grant No. DE-FG22-86PC90529 from the Pittsburgh Energy Technology Center. The authors also wish to thank Sutcliffe-Speakman Carbons Ltd. of Lancashire, England for providing activated carbon samples.

REFERENCES

1. Ruthven, D.M., *Principles of Adsorption and Adsorption Processes,* Wiley, NY, 1984.
2. Calo, J.M., and M.T. Perkins, *Micropore Diffusion in Coal Chars Under Reactive Conditions,* DOE Final Tech. Report, DE-FG22-86PC90529F, May, 1990.
3. Crank, J., *The Mathematics of Diffusion,* 2nd ed., Oxford Univ. Press, 1975.
4. Debelak,K., *Influence of Changing Particle Structure on the Rate of Gas-Solid Gasification Reactions,* DOE Final Tech. Report, DE-AC21-81MC16053-F, August,1983.
5. Palekhar, M.G., and Rajadhyaksha, R.A., *J. Cat. Rev.-Sci. Eng.* **28**, 382 (1986).
6. Solomon, P.R. and J.M. Beér in *Coal Gasification: Direct Applications and Syntheses of Chemicals and Fuels,* DOE Coal Gasification Research Needs Working Group, June 1987.
7. Morgan, M.E., Jenkins, R.G., and Walker, P.L., Jr. *Fuel* **60,** 189 (1981).

Table I. Summary of parameters for $D_e/R^2 = (D_e/R^2)_o \exp(-E_D/RT)$.

Char	Species	$(D_e/R^2)_o$ (s^{-1})	E_D (kcal/mol)
Buller "B"	CO	0.022	0.32
(steam activated)	CO_2	0.029	1.2
	CH_4	0.047	1.4
PSOC-833	CO	0.012	0.57
{17.1% burn-off in 0.1MPa	CO_2	0.16	1.8
O_2 at 200°C (pre-oxidized)}	CH_4	0.028	0.42
PSOC-467	CO	0.09	0.82
{13.2% burn-off in 0.1MPa	CO_2	0.042	0.86
O_2 at 200°C (pre-oxidized)}			
Wyodak	CO	0.012	0.32
{0% burn-off;	CO_2	0.033	0.87
as pyrolyzed ("clean")}	CH_4	0.041	0.75
Wyodak	CO	0.041	1.1
{10.1% burn-off in 0.1MPa	CO_2	0.056	1.4
O_2 at 200°C (pre-oxidized)}	CH_4	0.41	1.3
Wyodak	CO	0.084	1.7
{15% burn-off in 0.1MPa	CO_2	0.045	1.3
O_2 at 200°C (pre-oxidized)}	CH_4	0.031	0.37
Wyodak	CO	0.024	0.42
{30% burn-off in 0.1MPa	CO_2	0.15	1.8
O_2 at 200°C (pre-oxidized)}	CH_4	0.095	1.1
Wyodak	CO	0.028	0.11
{0% burn-off;	CO_2	0.072	1.1
demineralized}	CH_4	0.088	0.92

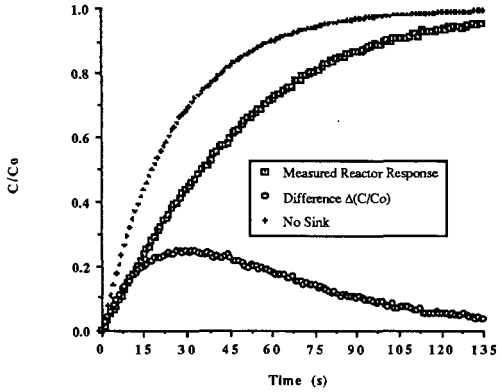

Figure 1. Data for CO diffusing into PSOC-833 coal char at T=285°C and P=30 psig, and theoretical response of a reactor with no internal porous mass sink under the same conditions.

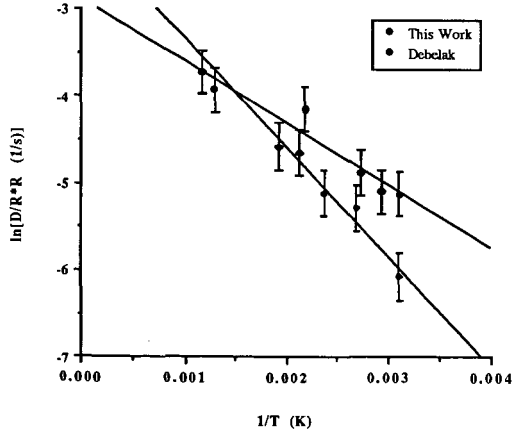

Figure 2. Comparison of activated diffusivities for CO_2 in Wyodak coal char in this work (10.1% burn-off in air) to those obtained by Debelak [4] (17.6% burn-off in CO_2).

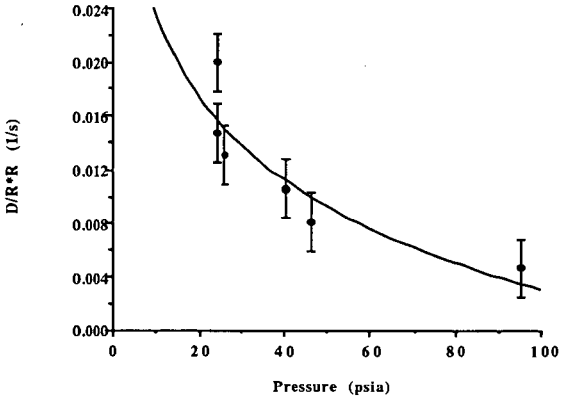

Figure 3. Effect of CO_2 pressure on effective diffusion time in PSOC-833 at 285°C.

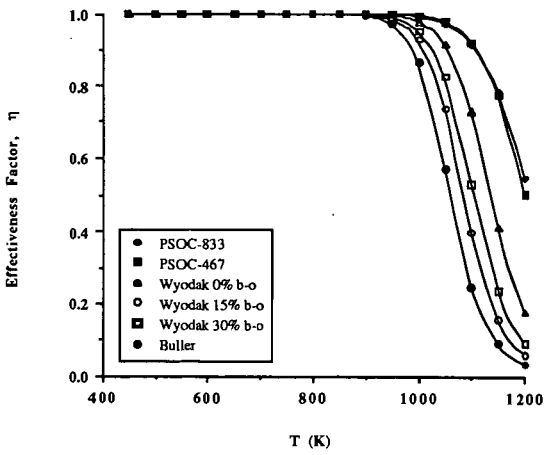

Figure 4. Calculated effectiveness factors for all the coal chars investigated.

CHEMISORPTION OF NITRIC OXIDE ON CHAR: KINETICS AND MECHANISM

Hsisheng Teng and Eric M. Suuberg

Division of Engineering
Brown University
Providence, Rhode Island 02912

Keywords : Nitric Oxide, Carbon, Chemisorption, Active Sites

INTRODUCTION

The reactions of nitric oxide with carbons have been considered as offering interesting possibilities for reduction of NO emissions from combustion systems. Some of the relevant literature on these reactions has been reviewed in a paper on the global kinetics of the gasification reaction[1]. The first step of the process, involving the chemisorption of NO on the carbon surface, has been separately considered[2]. The literature on chemisorption and/or physisorption of NO on carbons is limited[3-15]. Most of these studies acknowledge that if temperatures are kept low (i.e. well below ambient) mainly physisorption occurs,[5,8,10]. It is generally agreed that chemisorption occurs to a significant extent at temperatures above ambient. The chemisorption is generally accompanied by formation of surface oxides and release of N_2. Beyond this, the nature of the chemisorption process remains somewhat of a mystery.

One study has reported that the chemisorption of nitric oxide affects the spin-resonance absorption of charcoal in a manner similar to oxygen; there is an increase of ESR absorption linewidth with increasing extent of absorption on a cleaned carbon surface[12]. The difference is that oxygen adsorbed at room temperature can be desorbed by evacuation, whereas nitric oxide cannot. The initial absorption appears, on the basis of magnetic susceptibility, infrared, and thermal studies, to involve the addition of nitric oxide in an "N-down" configuration[5,6]. Another study cast doubt on the notion that the sites reactive towards nitric oxide addition could be spin centers[4]. It also appeared that more highly heat-treated carbons gave nitric oxide surface complexes of lower thermal stability[4]. This suggests that addition to aromatic ring structures is involved, and that the number of resonance structures affects the stability of the NO adduct. In short, it appears that the literature implies that radical addition processes occur on the surface of carbons, involving the paramagnetic nitric oxide (which is essentially free radical in nature). These addition processes appear to affect the ESR spectra, but do not destroy the measurable free radicals in carbons (which are probably of the π type). Thus the addition process does not appear to involve the "titration" of the measurable radicals in carbon by the nitric oxide. Hence the identity of the "active sites" in carbon remains unclear. The present measurements shed some new light on these issues.

EXPERIMENTAL

A standard thermogravimetric analyzer (TGA) was used for studying the kinetics of NO chemisorption on chars. Experiments were performed in a static gas environment, in He/NO mixtures at 101 kPa total pressure. The volume of the vessel was large enough to ensure that under any reaction conditions, the consumption of NO was not significant. Pulverized char samples

(50~100 mg) were held in a quartz bucket suspended in the heated zone of a quartz tube. A thermocouple placed within a few millimeters of the bucket served to indicate its temperature. The vessel could be purged following experiments, and the contents analyzed by gas chromatography.

The chars used in present study were derived from phenol-formaldehyde resins. These resins were synthesized in house in order that they contain few catalytic impurities (< 200 ppm)[16]. The resin char was prepared by pyrolysis of the phenol-formaldehyde resin in a helium environment at 1323 K for 2 hours, then ground and sieved to give the desired particle size. The surface of the char was cleaned of oxides prior to NO sorption experiments by heating the sample to 1223 K in extra high purity helium for at least 2 hours. NO sorption experiments were performed after surface cleaning by lowering the temperature of the sample from 1223 K to the desired sorption temperature, and then quickly introducing the desired NO/He mixture.

In order to clarify the mechanism of NO sorption on char, information on surface species formation during the course of sorption is required. Since N_2 and CO, both with a molecular weight of 28, are released during the thermal desorption of products from NO oxidized carbon, mass spectrometry could not be used for gas analysis. This required the use of gas chromatography (GC) as the main analytical technique. Thus temperature programmed desorption (TPD) experiments, with a linear heating rate of 22.5 K/min, were carried out in a TGA/GC system. TPD of NO treated chars were performed from 473 to 1223K. The desorbed gas products, purged from the TGA by helium, were collected in a cryogenic trap of Porapak-QS polymer kept at liquid-nitrogen temperature (77 K). This was necessary to boost product concentrations to conveniently measurable levels, as the concentrations within the TGA ambient gas were very low. The products could be desorbed from the trap by raising its temperature to ambient. Quantitative measurements of the products were performed on a Hewlett Packard GC equipped with a 2.1-m column of molecular sieve 5A. Significant amounts of NO were found to non-dissociatively adsorb on carbon surface at temperatures lower than 473K. The analysis of NO by this technique is not quantitatively reliable, but from the data on sample mass and GC analysis of other products, the quantity of NO desorbed during TPD could be evaluated from a mass balance. The surface species formed on chars were studied as a function of NO pressure, time, and temperature.

Specific surface areas of the samples were determined by the N_2 BET method at 77 K. A standard flow-type adsorption device (Quantasorb) was employed for the measurements. Prior to any such analysis, samples were outgassed in flowing N_2 at 573 K for 3 hours.

RESULTS AND DISCUSSION

The mass uptake curves obtained during chemisorption of NO on a cleaned char surface are shown in Figure 1, and as we have reported earlier, follow so-called Elovich sorption kinetics[2]:

$$r_{ad} = dq/dt = b \cdot \exp[-a \cdot q] \qquad (1)$$

where r_{ad} is the rate of sorption, a and b are fitting parameters, and q is the amount of mass uptake per unit of BET surface area. The values of a and b under different chemisorption conditions are given in Table 1. The value of a is a function of chemisorption temperature in NO sorption on char (as it is in O_2, e.g. ref 17,18). The value of a is generally a decreasing function of chemisorption temperature in the case of O_2 chemisorption. It is an increasing function of temperature in NO chemisorption. An increasing value of a with increasing chemisorption temperature can lead to a negative apparent activation energy for chemisorption , based on the following equation:

$$d\ln(r_{ad})/d(1/T) = -E_{ad}/R = d(\ln b)/d(1/T) - [da/d(1/T)]\cdot q \qquad (2)$$

where E_{ad} is the apparent activation energy for chemisorption. The first term is positive (see below) and the second term is negative, implying that E_{ad} must be negative. The increase of the value of a with increasing chemisorption temperature in the case of NO chemisorption has been attributed to the occurrence of exothermic reversible NO sorption which would result in less mass uptake at higher temperature[2]. The overall NO sorption reaction is actually a combination of reversible and irreversible process, *vide infra*, and cannot be simply represented by (1) or (2).

The physical significance of the parameter b is that it represents the initial rate of mass uptake on the clean char surface. At constant temperature, it is seen from Table 1 that the value of the parameter b increases with increasing NO pressure, as might be expected from a surface collision controlled process. This result is similar to that of O_2 chemisorption reported by other workers[18]. In the case of NO chemisorption, however, the b value decreases with increasing chemisorption temperature. This would also imply a negative activation energy for the initial chemisorption, again because of the reversible nature of NO uptake [2]. In short, Elovich-type analyses may provide satisfactory curve fitting for the NO-carbon system, but they are of no physical significance.

The existence of a certain amount of reversible sorption of NO has been earlier established[2,3]. We showed that such chemisorption data imply a heat of reversible chemisorption of -42 kJ/mol (i.e. exothermic)[2]. A heat of reversible NO adsorption on graphite of around -70 kJ/mole has been reported by others[6]. These values indicate chemisorption, since they are much higher than those for ordinary physisorption, which are usually less than 20 kJ/mol exothermic. The process can be represented in thermodynamic terms by[2]:

$$C + NO \leftrightarrow C(NO) \qquad (R\ 1)$$

This process of reversible sorption of NO is however accompanied by irreversible surface reactions involving NO. Moreover the thermodynamic representation of the reaction (R1) does not correctly portray the kinetics of this process, as discussed below.

Surface Complexes Involved in NO Chemisorption on Char

Once C(NO) is formed, it can react via thus far unestablished mechanisms to give other irreversibly bound surface species. This process can be generally represented by:

$$x_1 C(NO) + x_2 NO + \text{carbon surface} \rightarrow x_3 C(O) + x_4 C(O2) + x_5 C(N2) + x_6 N_2 + x_7 CO_2$$

The choice of the symbols on the right hand side is based on the experiments used to identify surface products.The symbol C(N2) represents the surface species that result in release of N_2 during post-chemisorption TPD. Likewise, CO is said to come from C(O), CO_2 from C(O2), and NO from C(NO). No particular structures or desorption mechanisms are implied by this nomenclature; it is selected for convenience alone. Both N_2 and CO_2 can evolve during chemisorption. The CO_2 is measured by GC, at the end of chemisorption. The N_2 is determined by mass and element balance, based upon the results of the post-chemisorption TPD analysis. The results of these analyses, following different times of sorption under 10.1 kPa of NO at 323 and 373 K, are shown in Figs. 2 and 3, in units of g/m^2. No other products are seen.

The amount of N_2 forming complexes, C(N2), remained roughly constant on the char surface

throughout chemisorption at $0.98 \cdot 10^{-4}(\pm 0.12 \cdot 10^{-4})$ and $0.76 \cdot 10^{-4}(\pm 0.10 \cdot 10^{-4})$ mmole/m^2 for 323 and 373 K, respectively. Although the sites for C(N2) have been saturated at these chemisorption conditions, the number of C(N2) complexes on the char surface under these conditions is still less than that during steady state gasification (~ $3.6 \cdot 10^{-4}$ mmole/m^2)[1]. Since in the low temperature chemisorption regime, C(N2) decreases with increasing temperature, the higher value at the higher gasification temperatures cannot be predicted by simple extrapolation of the low temperature chemisorption results. It is likely that C(N2) complexes are created by different mechanisms during gasification at higher temperatures.

We believe that C(N2) actually involves dissociated N atoms on the surface, because of the high desorption temperatures needed to release most of this product (>900K). These are relatively minor surface species, and because we observe them to form very quickly (virtually all before the first surface species measurements), they may be formed at exceptionally active surface sites on the freshly cleaned char surface. We cannot necessarily rule out the possibility that this surface species quickly builds up to a static concentration as a result of a fast dynamic equilibrium involving its formation and destruction, but this seems unlikely since the kinetics of release of N_2 during chemisorption (see Figs. 2 and 3) appear to be too slow to support such a dynamic equilibrium.

In contrast to C(N2), both C(O) and C(O2) both increase in concentration throughout chemisorption (see Figs. 2 and 3). The C(O2)/C(O) ratio on char surface is not constant during chemisorption and at 323K increases from 0.27 (molar basis) after 0.2 hour of chemisorption to 0.52 after 24 hours. For 373 K chemisorption in 10.1 kPa NO, the C(O2)/C(O) ratio increases slightly with reaction time from 0.22 after 0.2 hour to about 0.27 after 1.6 hours and remains constant afterwards. The C(O2)/C(O) ratio of 373 K sorption is less than that of 323 K sorption. The increasing C(O2)/C(O) ratio of surface species with decreasing reaction temperature is in agreement with the fact that the CO_2/CO ratio decreases with increasing steady state gasification temperatures[1]. The TPD results have revealed that the CO_2 desorption product evolves at lower temperatures than the CO desorption product. In fact, the formation of gaseous CO_2 product is significant during chemisorption at 373 K, but was too low to be accurately measured at 323 K (see Figs. 2 and 3). Considering the sum of C(O2) plus desorbed CO_2 in the case of the 373 K sorption, this value is actually seen to be quite similar to the value for C(O2) alone at 323 K, at all times. The weak temperature dependence in the kinetics of formation of the total C(O2) complexes implies that there is a process of moderately low activation energy responsible for the conversion of other surface intermediates to C(O2). The apparently strong temperature dependence of the actual C(O2) population actually reflects the temperature dependence of desorption of CO_2.

The population of C(O) on char is a weak function of sorption temperature, and is seen to slightly decrease with increase in temperature, for any time of measurement. The total yield of all irreversible C(NO) decomposition products, i.e. C(N2), C(O) and C(O2) surface complexes plus released gaseous CO_2, is relatively constant after 24 hours, for any given temperature within this range (15.4 and 14.4 mmol/m^2 for 323 and 373 K, respectively). One might expect that when CO_2 is desorbed in the 373 K case it would leave an "active site" behind that could gain further oxygen by the same mechanism as before, but this does not appear to happen. This implies that the surface appears to "heal" itself upon CO_2 desorption, and that active sites are <u>not</u> regenerated by desorption at these temperatures (This conclusion does not hold when higher temperatures are involved; TPD of this char following NO exposures up to gasification conditions shows the oxide population to be an increasing function of temperature[19]).

Since the total population of surface species changes little with time beyond about 24 hours, the behavior in NO chemisorption is quite different from that in O_2 chemisorption. In O_2, the total number of complexes quite commonly continues to increase indefinitely, until the rate of desorption begins to overtake the rate of chemisorption. In NO, it appears that there is only a particular inventory of sites that can be filled, at any temperature. What limits the inventory is unclear. The fact that the total uptake of irreversibly held species is only a weak function of temperature suggests that certain types of structures initially exist within the carbon, and that they alone are capable of participating in the formation of dissociation products.

The mass of chemisorbed oxygen atoms on the char surface can be converted to a surface area occupied by these oxygen atoms, by applying the assumption[20] that each oxygen atom occupies an area of $8.3 \cdot 10^{-20}$ m^2. The surface area occupied by oxygen atoms of any released CO_2 before its desorption from the char surface is taken into account. This surface area is obviously a weak function of chemisorption temperature and constitutes 0.094±0.003 of the total surface area (TSA = 320 m^2/g) of the sample, under the conditions at which the surface oxide inventory was measured (18% burnoff char). In the case of oxygen chemisorption on this same char, the surface area occupied by oxygen atoms is an increasing function of chemisorption temperature, accounting for 0.032 of TSA at 373 K and 0.046 at 473 K. Different numbers of "active sites" are thus apparently involved in NO and O_2 chemisorption, although this comparison is perhaps unfair in that the carbons on which oxygen ultimately resides may not be the same as the carbons involved in the initial chemisorption. It should also be mentioned that in the case of NO, there is a strong suggestion that the micropore surface area is not fully accessible[19], so the value of 0.094 may actually underestimate the fraction of accessible surface that is covered. A similar accessibility problem was not observed with O_2.

The Kinetics of Surface Complex Formation

The formation during chemisorption of each of the different types of surface complexes can be described by the Elovich equation (1) and the fitting parameters a and b for the different complexes are shown in Table 2. Again, comments similar to those related to those for total mass uptake may be made with respect to these (note trends with temperature). In this case, however, the b parameter provides some useful insights into the process. The b value is about an order of magnitude higher for the formation of C(O) than that for C(O2) at 323 K. Since b is the initial rate of complex formation, the relative magnitudes of these values apparently imply that the C(O) complexes are created earlier. This in turn suggests that some of them could serve as reactive intermediates on the char surface, and can react with NO from the gas phase or C(NO) on carbon surface, to generate the C(O2) complexes. The hypothesis that C(O2) is derived from C(O) has been advanced earlier[11].

At 323 K,the formation of reversibly adsorbed NO (i.e. C(NO)) is slightly more rapid than other surface species (see Table 2). Thus it seems to support the very plausible notion that the C(NO) surface complex may serve as an initial intermediate. Such an initial step for NO-carbon chemisorption was also proposed by previous workers[4,10]. It is unclear how the kinetics of formation of other surface species should depend on C(NO) concentration ([C(NO)]), or on the partial pressure of NO in gas phase (one or the other must be involved, based upon stoichiometric considerations). Reactions were performed at 323 K under different NO pressures to explore this

dependence. By back extrapolation of these data to zero time, the rates of complex formation on clean char surface under different NO pressures were determined.

The initial rates of C(NO) formation (r_0) on clean char surface under different NO pressures are shown in Fig. 4. It was found that the reaction of C(NO) formation on clean surface is close to second order with respect to NO pressure. Thus the reaction (R1) does not accurately portray the kinetics of this step. We hypothesize that the addition of NO occurs in a process that can be represented in two steps:

$$\text{Carbon Surface} + NO \;\text{<---> } C(NO)^* + C^* \qquad \text{(R1a)}$$
$$C(NO)^* + C^* + NO \;\text{<----> } 2\,C(NO) \qquad \text{(R1b)}$$

where C(NO)* is an unstable NO addition product, C(NO) is the stable product, and C* represents the odd electron contributed to the carbon structure by the first NO addition step. It is hypothesized that the odd electron must be paired with a second electron, in order to make two surface complexes stable. This is the origin of the second order. Note that overall, the concentration of C(NO) would still be proportional to NO partial pressure, as in (R1).

There was little C(NO) on the clean char surface initially, and it was impossible to establish the role of C(NO) in the reactions for C(O) and C(O2) formation on the clean surface by the same kind of back extrapolation to zero time. Thus the rates of C(O) and C(O2) formation were evaluated, at particular extents of total oxide surface coverage to clarify the role of C(NO) in the reaction. It was found that the rate of C(O) formation was approximately first order with respect to C(NO) and simultaneously second order with respect to gas phase NO. Thus, the process appears to be limited by the ability to form a second stable complex in the vicinity of a first stable C(NO) complex.

As for the formation of C(O2), the rate might be expected to be related to the population of C(O) on the char surface. Therefore rates of C(O2) formation were examined at constant [C(O)]. It was found that the rate was first order with respect to both C(NO) and C(O), and second order with respect to NO in the gas phase. Again, the suggestion is that the placing of a stable C(NO) complex near to existing surface complexes is a key limiting step.

CONCLUSIONS

The chemisorption of NO on char surface is not always immediately followed by the release of N_2 from the dissociation of the NO molecule. Reversibly (i.e. C(NO)) as well as irreversibly bound complexes (i.e. C(O), C(O) and C(N2)), can all exist on the char surface. The reversible sorption of C(NO) on a resin char surface is an exothermic reaction having an enthalpy of -42 kJ/mole. The rate of C(NO) formation on clean char surface is roughly second order with respect to NO pressure, but [C(NO)] is proportional to NO pressure at equilibrium. The mechanism for C(O) and C(O2) formation appears to involve both gaseous NO and C(NO) complexes. The formation of stable C(NO) surface complexes is hypothesized to involve an electron-pairing mechanism, and is important in the formation of irreversibly bound surface complexes as well.

ACKNOWLEDGEMENT

The financial support of the U. S. D.O.E. (grant DE-FG22-87PC79929) and the Exxon Education Foundation are gratefully acknowledged.

REFERENCES

1. Suuberg, E.M., Teng, H. and Calo, J.M., 23rd Symposium (Int.) on Combustion, The Combustion Institute, in press (1990-91).
2. Teng, H., Suuberg, E.M., and Calo, J.M., ACS Div. Fuel Chem Prepr., **35(3)**, 592 (1990).
3. DeGroot, W.F., Osterheld, T.H., and Richards, G.N., Carbon, **29**, 185 (1991).
4. Harker, H., Gallagher, J.T., and Parkin, A., Carbon, **4**, 401 (1966).
5. Zarifyanz, Y.A., Kiselev, V.F., Lezhnev, N., and Nikitina, O., Carbon, **5**, 127 (1967).
6. Zarifyanz, Y.A., Russian J. of Physical Chemistry, **38**, 1439 (1964).
7. Smith, R.N., Swinehart, J., and Lesnini, D., J. Phys. Chem., **63**, 544 (1959).
8. Smith, R.N., Lesnini, D., and Mooi, J., J. Phys. Chem., **60**, 1063 (1956).
9. Shah, M.S., J. Chem. Soc., 2661 (1929).
10. Brown, C.E. and Hall, P.G. , Trans. Faraday Soc. **67**, 3558 (1971).
11. Brown, C.E. and Hall, P.G. , Surface Science, **30**, 379 (1972).
12. Pastor, R., Weil, J., Brown, T., Turkevich, J., Adv. in Catalysis, **9**, 107 (1957).
13. Richter, E., Kleinschmidt, R., Pilarczyk, E., Knoblauch, K., Jüntgen, H., Thermochimica Acta, **85**, 311 (1985).
14. Richter, E., Chem.-Ing.-Tech., **55**, 986 (1983).
15. Cascarini de Torre, L.E. and Arvia, A.J., An. Quim. **64**, 349 (1968).
16. Suuberg, E.M., Wójtowicz, M., and Calo, J.M., 22nd Symposium (Int.) on Combustion, The Combustion Institute, 79 (1988).
17. Khan. M.R., Everitt, C.E., and Lui, A.P., Comb. and Flame, **80**, 83 (1990).
18. Bradbury, A.G.W. and Shafizadeh, F., Carbon, **18**, 109 (1980).
19. Manuscript in preparation.
20. Laine, N.R., Vastola, F.J. and Walker, P.L., Jr., J. Phys. Chem., **67**, 2030 (1963).

Table 1. The Elovich parameters for NO chemisorption on char- total mass uptake

Pressure (kPa)	10.1				4.04	2.02
Temperature (K)	473	423	373	323	323	323
a $[m^2/g]\cdot10^{-6}$	0.265	0.249	0.225	0.0811	0.117	0.149
b $[g/m^2hr]\cdot10^{6}$	53.5	86.1	221	337	69.8	16.0

Table 2. The Elovich parameters for formation of surface complexes.

	C(O2)	C(O)	C(NO)
T = 323 K			
$a\cdot10^{-6}$	0.213	0.248	0.147
$b\cdot10^{6}$	19.4	155	211
T = 373 K			
$a\cdot10^{-6}$	0.474	0.240	0.658†
$b\cdot10^{6}$	16.8	71.5	96.8

a is in m^2/g, and b is in $g/(hr\cdot m^2)$ † 1.6 hours of chemisorption

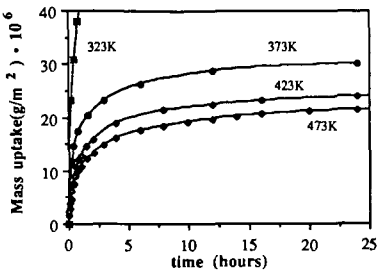

Fig. 1 Total mass uptake as a function of time in chemisorption under 10.1kPa NO pressure.

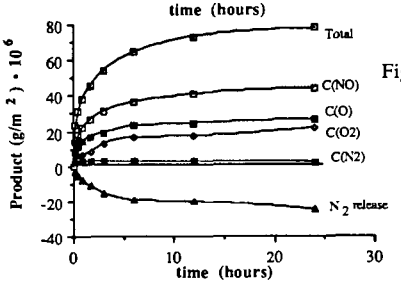

Fig. 2 Product formation during 323K chemisorption under 10.1kPa of NO (mass of carbon not included in C(NO) and C(N2) values).

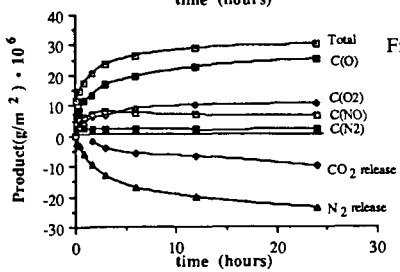

Fig. 3 Product formation during 373K chemisorption under 10.1kPa of NO (mass of carbon not included in C(NO) and C(N2) values).

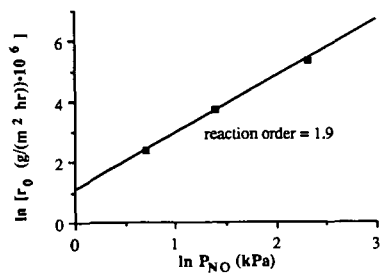

Fig. 4 Initial rate of C(NO) formation on clean char surface under different NO pressures.

MODELING OF OXYGEN CHEMISORPTION ON MICROPOROUS CARBONS

J. K. Floess
Department of Chemical Engineering
University of Illinois at Chicago
Chicago, IL

Keywords: microporous carbons; oxygen chemisorption; chemisorption kinetics

Introduction

The reaction of oxygen with carbon is believed to involve the dissociative adsorption of oxygen on the carbon to form carbon-oxygen surface complexes and the subsequent desorption of these complexes to carbon monoxide, or in a more complex sequence of steps, to carbon dioxide. The oxygen chemisorption step is effectively irreversible in that desorption to oxygen apparently does not occur; instead, desorption involves the breaking of one or more carbon-carbon bonds in the solid and the formation of carbon oxides. Because the adsorption and desorption steps involve distinct chemical pathways, however, it is necessary to investigate each of these step independently in order to determine the overall energetics of the reaction. An objective of this study was to determine activation energies for the oxygen chemisorption step by analyzing chemisorption data on a microporous char in terms of a distributed activation energy model.

This paper discusses the modeling of oxygen chemisorption kinetics with the assumption that there is a distribution of activation energies for adsorption. Two different types of heterogeneous surfaces were considered: in one case, it was assumed that the surface has an a priori distribution of activation energies for adsorption whereas in the second case, it was assumed that the activation energy increases as a consequence of oxygen chemisorption (i.e., due to induced heterogeneity). For each model, the activation energy was assumed to vary linearly with coverage. Experimental data reported by Kelemen and Freund[1] and by Floess et al.[2] show that the activation energy for chemisorption, to a first approximation at least, increases linearly with oxygen coverage. Consequently, the proposed distribution does adequately represent available experimental data. Furthermore, the use of a linear distribution function allows the model equations to be solved analytically rather than numerically. The availability of analytical equations simplifies the problem of obtaining model parameters from experimental data, and finally, an analytical solution provides insight into the behavior of the solution that is not easily discernible from numerical results.

Experimental

In this study, oxygen chemisorption data on a microporous carbon were obtained in a series of isothermal adsorption runs at temperatures between 400 and 548 K and at oxygen partial pressures up to 1atm. Experimental data were obtained using a thermogravimetric analyzer. Gas compositions in the reactor were also monitored by leaking a small amount of gas to a quadrupole mass spectrometer. A detailed description of the experimental approach is given in reference (2).

Chemisorption data were obtained with Spherocarb that had been partially reacted to 5% conversion and then outgassed. Pretreatment of the char in this manner was found to substantially increase the amount of oxygen that could be chemisorbed at low temperatures. The experimental data, which are presented later, are reported on a normalized basis with respect to the maximum amount adsorbed, which was taken to be the amount adsorbed at conditions where the rate of gasification is negligible. This oxygen uptake, however, is significantly less than the amount of oxygen typically present on a char after partial gasification. In other words, with carbon conversion, the oxygen content increases significantly above the amount present when no conversion has yet occurred. Although the choice of a normalization factor for reporting experimental data is to a degree arbitrary, its value can affect the interpretation of the model results, as will be shown later.

Chemisorption Models

The first model assumes that there exists a continuous distribution of activation energies for adsorption. Here $\eta(\varepsilon)$ is the density of the distribution function, and $\eta(\varepsilon)\Delta\varepsilon$ is the fraction of total sites with an activation energy for adsorption between ε and $\varepsilon+\Delta\varepsilon$. The rate of adsorption on sites of energy ε is:

$$\frac{d[C(O)_\varepsilon]}{dt} = k_\varepsilon C_{O_2} (1 - \theta_\varepsilon) \qquad (1)$$

where $C(O)_\varepsilon$ is the concentration of adsorbed oxygen atoms on sites of energy ε; k_ε is the adsorption rate constant; C_{O_2} is the oxygen concentration; and θ_ε the fraction of sites of energy ε that are occupied. The reverse reaction is neglected in this equation since oxygen chemisorption is assumed to be irreversible, and the analysis is limited to the case of negligible gasification. Integration of (1) yields:

$$\frac{C(O)_\varepsilon}{C_{T_\varepsilon}} = \theta_\varepsilon = [1 - \exp(-\bar{k}_\varepsilon t)] \qquad (2)$$

where $\bar{k}_\varepsilon = k_\varepsilon C_{O_2} / C_{T_\varepsilon}$.

The total amount adsorbed is obtained by integrating equation (2) over the activation energy distribution:

$$\{C(O)\}(t) = C_t \int_{\varepsilon_*}^{\varepsilon^*} [1 - \exp(-\bar{k}_\varepsilon t)]\, \eta(\varepsilon)\, d\varepsilon \qquad (3)$$

For a linear distribution function (i.e., the density of the distribution is equal to a constant), equation (3) may be integrated analytically to give:

$$\theta(t) = \frac{\{C(O)\}t}{C_t} = 1 - \eta_o RT\, [E_1(\bar{k}^* t) - E_1(\bar{k}_* t)] \qquad (4)$$

where E_1 is the exponential integral; $\eta_o = 1/(\varepsilon^* - \varepsilon_*)$; and $\bar{k}^*$ and $\bar{k}_*$ are the rate constants at ε^* and ε_*, respectively.

This equation may be differentiated to obtain the rate of oxygen chemisorption:

$$\frac{d\theta}{dt} = \eta_o \frac{RT}{t} [e^{-\bar{k}^* t} - e^{-\bar{k}_* t}] \qquad (5)$$

The rate equation for the second model, where it is assumed that surface heterogeneity is induced by oxygen chemisorption, is:

$$\frac{d[C(O)]}{dt} = k(\theta)\, C_{O_2}\, (1 - \theta) \qquad (6)$$

Here $k(\theta)$ indicates the dependence of the adsorption rate constant on oxygen coverage. This model has been used by Tokoro et al.[3] to analyze desorption data and to obtain site energy distributions from experimental data in a comparatively straightforward manner.

For the case where ε varies linearly with θ:

$$\varepsilon = a\theta + b \qquad (7)$$

equation (6) can be integrated to yield:

$$\int_0^\theta \frac{e^{a\theta/RT}}{(1 - \theta)}\, d\theta = k't \qquad (8)$$

Here $k' = A_o \exp(-b/RT)\, C_{O_2}/C_t$

This integral may be evaluated to obtain its asymptotic behavior as $\{a/RT\} \rightarrow \infty$:

$$k't = \frac{RT}{a} \frac{e^{a\theta/RT}}{(1 - \theta)} \qquad (9)$$

Equations (4) and (8) are intrinsic rate equations for oxygen chemisorption for each model. However, in applying these equations to experimental data it is necessary to correct for the effects of bulk phase mass transfer, intra-particle diffusion, and instrument response time on the observed kinetics. In this study the two principal effects were the instrument response time and and the bulk phase mass transfer resistance. (Although, as a rule of thumb, intra-particle diffusion will usually manifest itself before bulk phase diffusion, in this study this was not the case since the length scales for mass transport and intra-particle diffusion were widely different. Experimental measurements[2] confirmed that there was no effect of particle size on the chemisorption rates obtained in these experiments.)

The TGA used in the experiments had a characteristic response time of 3.4 sec. The response of the instrument to a step change in weight could be adequately fitted by a first order model (both first and second order response models were investigated).

The mass transfer coefficient was estimated from the correlations of Wigmans et al.[4] and of Treybal[5]. Both correlations yield a Sherwood number of approximately 4. over the temperature range of 300-800K and for a flowrate of 60 scc/min. However, because of the large temperature gradient in the furnace tube neither correlation is entirely valid for the actual flow conditions in the TGA. The Raleigh number for the gas flow in the furnace tube is estimated to be $3.x10^5$, and for this value, the flow in the tube is dominated by free convection[6]. In any case, the characteristic mass transfer time (at an oxygen partial pressure of 0.5 atm) is 1.0 s, so that instrument lag is the dominant resistance for the experiments reported here.

The bulk phase mass transport resistance can be incorporated in a straight forward manner into the model of Tokoro to give:

$$\frac{d\theta}{dt} = \frac{C_{o_2}^{\circ}}{\frac{1}{k_r (1 - \theta)} + \frac{1}{k_m}} \qquad (10)$$

where k_m is a mass transfer coefficient, $k_r = k(\theta)/C_t$, and $C_{o_2}^{\circ}$ is the bulk oxygen concentration. This equation can be integrated to give:

$$t = \frac{1}{k'} \int_0^{\theta} \frac{e^{a\theta/RT}}{(1 - \theta)} \, d\theta + \frac{\theta}{k_m C_{o_2}^{\circ}} \qquad (11)$$

For the distribution model no simple rate equation that includes the mass transfer resistance can be obtained.

Since the instrument response to a step disturbance is known, Duhamel's integral was evaluated to determine the actual uptake of oxygen recorded in the experiments:

$$\theta = \int_0^t \theta(s) \frac{1}{\tau} e^{-(t - s)/\tau} \, ds \qquad (12)$$

where $\theta(s)$ is the amount of oxygen adsorbed as a function of time given by equation 4, 8, or 11 and τ is the instrument time constant. The integral was evaluated analytically by locally approximating $\theta(s)$ by a straight line over a time interval Δt_i. The results of the integration are presented in Figure 1. As shown, the adsorption curves obtained when the mass transfer resistance is also included in the calculations are not appreciably different from the case where this resistance is neglected. Consequently, the mass transfer resistance is neglected in comparing the results of each model, and equations (4) or (8) are used directly in equation (12).

Discussion

Calculations were done for different ranges of activation energies, which corresponds to different slopes for the activation energy distribution shown in Figure 2. It is likely, as shown by the dashed lines in the figure, that deviations from linearity occur at both extremes of the distribution. The deviation from linearity at the low activation energy end will not appreciably affect the results since chemisorption rates here are faster than can be measured experimentally under non-vacuum conditions. At the high end, it is assumed that the fraction of sites that deviate from the linear model and also contribute appreciably to the adsorption rate is small. Calculations were also done for two different values of the normalization factor.

Predicted isothermal adsorption curves at 400, 448, 498, and 548 K for two different activation energy ranges are shown in Figures 3 and 4. Both models give adsorption curves of a similar shape, and in fact, there is no basis for distinguishing between models. As a result, the choice of a model can be largely dictated by mathematical convenience. The model of Tokoro is advantageous when corrections for bulk phase mass transport or intra-particle diffusion need to be taken into account, and this model can be used in a straightforward manner to obtain a site distribution from experimental rate data by solving a set of n linear equations in m unknowns[3]. The unknowns are the pre-exponential factor and the constants in the function assumed for $\epsilon(\theta)$. The principal disadvantage of this model is that the correct θ values for the experimental data must be known.

Changing the range of activation energies alters the rise of the individual adsorption curves and the spacing between individual curves. However, these differences in the shape of the curves are not very sensitive to a change in the activation energy range. (For the two sets of data shown, the pre-exponential factors differ by 10^6.) In general, lowering the activation energy range tends to increase the rise of the curve between the initial, approximately linear, part and the final amount adsorbed and tends to push the curves closer together and up toward $\theta=1$. This bunching effect is accentuated for data near $\theta=1$. If, however, a larger normalization factor is used in calculating θ, the isothermal adsorption curves remain approximately equally spaced and do not come together since now the curves never reach $\theta=1$. As a result, the determination of the correct activation energy range is more difficult since one can now only use the rise of the curves to discriminate between activation energy ranges.

The effect of oxygen partial pressure on the adsorption curves is shown in Figure 5. The predicted curves are in good agreement with experimental data[2] previously reported.

Experimental chemisorption data for Spherocarb are presented in Figure 6, where the data are compared to model predictions for an activation energy range of 12 to 32 kcal/mole. This range gave the best agreement with the data for the assumption of a linear variation in activation energy with oxygen coverage. Agreement between the data and the model is satisfactory, although the model predicts a more rapid initial increase in oxygen coverage than is exhibited by the data. This discrepancy may be because the linear distribution assumed in the calculations is not sufficiently accurate for representing the actual activation energy distribution with the necessary precision.

Conclusions

This paper examined kinetic models for oxygen chemisorption on two types of heterogeneous carbon surfaces. In each case, a linear variation in activation energy with oxygen coverage was assumed. The models include correction terms for the effects of bulk phase mass transport and instrument response on the observed kinetics.

It was found that the adsorption curves obtained from each model are essentially similar and that the use of one or the other can be largely dictated by computational convenience. For example, the Tokoro model can be regressed in a straightforward manner to obtain model parameters from the data and can be readily modified to include the effects of intra-particle diffusion or bulk phase mass transfer on the kinetics.

Based on an analysis of experimental chemisorption data, it is concluded that the activation energy for oxygen chemisorption on a microporous char is in the range of 12-32 kcal/mole. However, since model predictions are rather insensitive to the range of activation energies, experimental data at precise temperature intervals are needed to accurately determine the activation energy range for chemisorption kinetics.

The models can correctly account for the oxygen partial pressure dependence of the chemisorption data.

References

1. Kelemen S. R.; Freund, H. *Carbon*, 1985, 23, 723-729.
2. Floess, J. K.; Lee, K-J.; Oleksy, S. A. *Energy and Fuels*, 1991, 5, 133.
3. Tokoro, Y.; Uchijima, T.; Yoneda, Y. *J. of Catal.*, 1979, 56, 110.

3a. Tokoro, Y.; Misono, M.; Uchijima, T.; Yoneda, Y. *Bull. Chem Soc. Japan*, 1978, 51, 85.

4. Wigmans, T.; v. Cranenburgh, H.; Elfring, R.; Moulijn, J. A. *Carbon*, 1983, 21, 23.
5. Treybal, R. E. *Mass Transfer Operations*; McGraw-Hill: New York, 1980.
6. Eckert E. R.; Drake, R. M. *Analysis of Heat and Mass Transfer*; McGraw-Hill, New York, 1972.

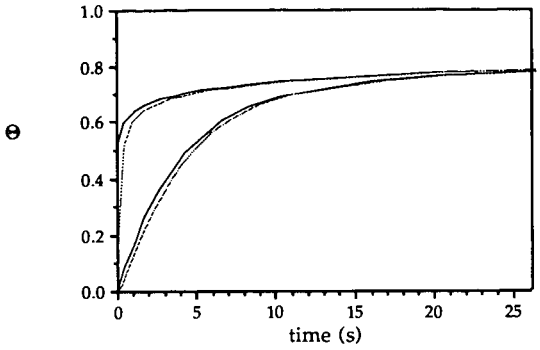

Figure 1. Effect of instrument response on chemisorption kinetics. Curves towards the left side of the graph are instrinsic kinetics; curves towards the right include instrument response; model of Tokoro: (- - -) includes mass transfer resistance; (—) no mass transfer included.

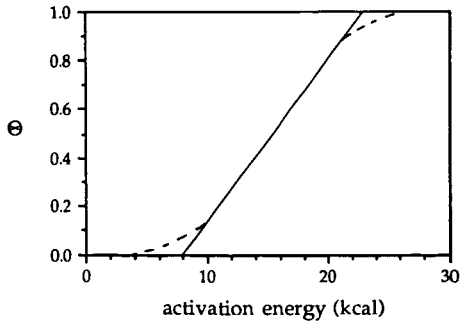

Figure 2. Activation energy distribution.

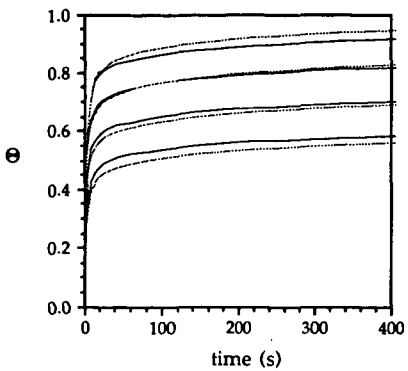

Figure 3. Predicted chemisorption curves at 400, 448, 498, 548 K, 0.5 atm oxygen partial pressure; activation energy range: 12.3 to 34.8 kcal; (---) distributed site model; (—) model of Tokoro.

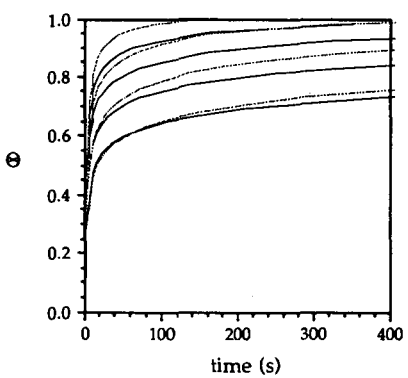

Figure 4. Predicted chemisorption curves at 400, 448, 498, 548 K, 0.5 atm oxygen partial pressure; activation energy range: 5.8 to 16.7 kcal; (---) distributed site model; (—) model of Tokoro.

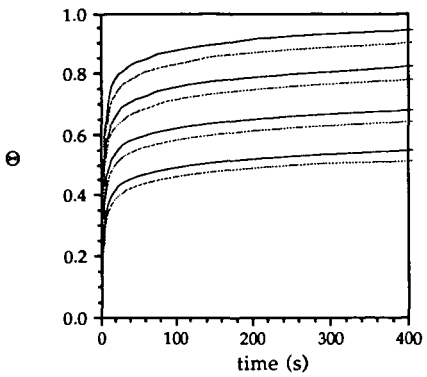

Figure 5. Model results for oxygen partial pressures of 0.5 atm (—) and 0.21 atm (---); site energy distribution model; activation energy range: 11.8 to 32.4 kcal.

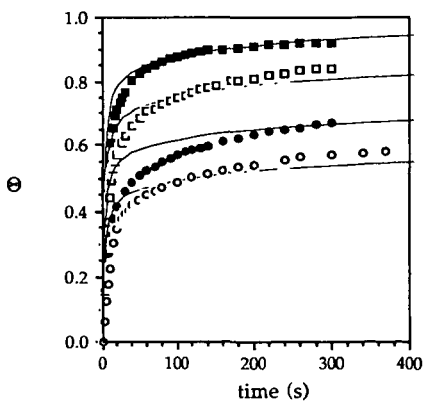

Figure 6. Comparision of chemisorption data at 400, 448, 498, and 548 K and 0.5 atm oxygen partial pressure to model results. Site energy distribution model; activation energy range: 11.8 to 32.4 kcal.

MORPHOLOGICAL CHANGES DURING OXIDATION OF A SINGLE CHAR PARTICLE

Matteo d'Amore[^], Leonardo Tognotti[*], and Adel F. Sarofim[o]

[^]University of Salerno, Chemical and Food Engineering Dept., Italy

[*]University of Pisa, Chemical Engineering Department, Italy

[o]Massachusetts Institute of Technology, Chemical Engineering Dept. Cambridge, MA 02139 (U.S.A.)

Keywords: char oxidation; morphology; electrodynamic balance.

ABSTRACT

The evolution of pore size distribution during the oxidation of single Spherocarb char particles has been measured under chemical controlled conditions. Electrodynamically levitated particles were heated to reaction temperature using a laser and the weight and size changes monitored. The laser heating was interruypted at selected conversions and the CO_2 adsorption determined at ambient conditions. As reaction proceeds, particles are found to shrink, the macropore volume decreases in proportion to the total particle volume, maintaining a constant macroporosity. The micropore volume, however, decreases with increasing conversion whereas the normalized pore size distribution remains unchanged, suggesting that the densification of the microporous volume which leads to particle shrinkage results from pore elimination. At the same time the mesopore volume increases with increasing conversion indicating that the mesopores play a dominant role in the char reaction.

1. INTRODUCTION

The reaction rate of carbon burning under chemical kinetic or internal diffusion controlled regime is strongly affected by the pore structure, which governs the extent of penetration of the reacting gases and, through the porosity evolution with conversion, the total amount of surface available for reaction (Gavalas, 1980; Mohanty et al., 1982; Reyes and Jensen, 1986).

The problem of evaluating the variation of combustion rates with conversion is usually reduced to the purely topological problem of establishing the relationship between accessible surface area and porosity as this latter changes. In the above referenced theoretical studies the assumption is made either that the reactivity is constant over the entire surface or restricted to the non microporous area (Gavalas, 1980). Accessibility to the microporous area may be restricted due to hindered diffusion in pores having dimensions approaching that of the reacting molecules and reactivities may vary due to either graphitization of surfaces or non-uniform distribution of catalysts. For this reason it is

desirable to experimentally determine the evolution of pore structure with increasing carbon conversion.

Whatever the experimental technique used, the possible occurrence of phenomena like shrinkage (Hurt et al., 1988) or fragmentation by percolation (Bar-ziv et al., 1989; Kerstein and Niksa, 1985), complicates the analysis of data to obtain basic information on porosity and surface area. Moreover, the experimental apparatuses currently used for reactivity measurements and the porosimetry techniques presently available, even when used on small amounts of samples, yield average information, since they integrate the results over the entire number of particles used. All these uncertainties result in tremendous data scattering (up to four orders of magnitude at a given temperature) when general correlations for intrinsic reactivity of coal chars are proposed (Smith, 1982).

In this study, the changes with conversion in morphology of a carbon char in the temperature range 500-1200 K are followed by using an electrodynamic balance (EDB) (Spjut et al., 1985; Dudek, 1988; Bar-ziv et al., 1989). This device allows one to measure in situ, over temperature range wider than in other apparatuses, mass, diameter, density, surface area, rate of reaction and temperature for a single, suspended submillimeter particle. By following with the EDB the changes in the char as it reacts, it is possible to study the influence of the porous texture on the reaction behavior and shed some light on the contribution by micropores to the reaction in the chemical kinetic controlled regime.

The pore sizes will be broken down into three classes: micropores (diameters between 0.8 and 3 nm), mesopores (3 <d < 20 nm), and macropores (20 nm < d). The micropores will be determined by CO_2 gas adsorption and a significant part of the results and discussions in this paper will be devoted to the interpretation of adsorption data to obtain the finer pore structure. The macropores are traditionally obtained by mercury intrusion porosimetry, although precautions must be taken to separate the contribution of interparticle voids from those of the larger macropores (Bellezza, 1985). In this study the result of Hurt et al. (1988) that the macropore volume is constant during reaction in the kinetic controlled regime will be utilized. This result was based on the observation that all macrofeatures of a particle were conserved during reaction in a chemical controlled regime and that the changes in diameters of macropores, down to the limit of resolution of 100 nm on the electromicrographs, were proportional to the change in the particle diameter. The mesopores are traditionally measured by capillary condensation with the results being somewhat dependent on the method of interpretation of the adsorption-desorption isotherms. In this study the mesopores will be determined from a volume balance utilizing the special capability of the EDB for measuring the density of a single particle.

2. EXPERIMENTAL

2.1 Apparatuses

Electrodynamic Thermogravimetric Apparatus

The electrodynamic chamber consists of three electrodes in an hyperboloidal configuration, the theory of which is described by

Wuerker et al. (1959), Davis and Ray (1980), Philip (1981) and Spjut (1985). A schematic view of the electrodynamic balance is shown in Fig. 1. The chamber creates a dynamic electric field capable of suspending a single, charged particle with a characteristic size less than 250 μm in the present configuration. The AC or ring electrode provides lateral stability to the particle through an imposed AC field oscillating sinusoidally ±2000 volts at 100 Hz. The DC top and bottom electrodes provide vertical stability by balancing the gravitational force, thus stably suspending the charged particle in the chamber. A position control system can be used which automatically adjusts the electric field to keep the particle at the chamber center. An optical microscope is used for viewing the particle and for manual control of the particle position. The microscope allows the measurement of the particle diameter to ±5 μm. A 20 W CO_2 laser is used to heat the suspended particle and a two color infrared (2 and 4 μm) pyrometry is used for temperature measurements. A gas flow system allows one to react a particle in various gaseous enviroments. Additional details on the experimental apparatus and procedure can be found in Spjut et al. (1985), Bar-ziv et al.(1989), Dudek et al. (1988).

Porosimetry

The pore size distribution of the char was measured by means of a Carlo Erba Sorptomatic 1800 static-volumetric apparatus, using N_2 at 77 K or CO_2 at 195 and 298 K as adsorption gases, and a high pressure mercury porosimeter model Carlo Erba 2000. The EDB was used as a gravimetric apparatus for CO_2 adsorption measurements on single "Spherocarb" particles at 298 K.

2.2 Char properties

The model char used in this work was "Spherocarb", a spherical microporous carbon from Analabs Inc.. The 60/80 mesh commercial fraction has been used in several previous studies (Waters et al., 1988, Dudek et al., 1988, D'Amore et al., 1988, Hurt et al., 1988) because of its high degree of uniformity and sphericity. Furthermore, the low ash content of the particles minimizes the effects of catalytic impurities, while the limited amount of volatile matter precludes the complicating effects of devolatilization on the burning behaviour. The gross physical properties and the chemical analysis of the material are reported in the following section.

Size	180-240	μm
Particle density	0.63	$g cm^{-3}$
True density	2.10	$g cm^{-3}$
BET surface area	963	$m^2 g^{-1}$
DR surface area	965	$m^2 g^{-1}$
Total surface area	1025.6	$m^2 g^{-1}$
Carbon content (weight basis, %)		96.9
Oxygen		2.4
Hydrogen		0.7

The BET area was obtained by analysing the N_2 adsorption isotherm at 77 K. Analysis of the CO_2 adsorption data at 195 and at 298 K by the Dubinin-Raduskevitch equation gave the DR area. The total surface area includes those of the micro-, meso-, and macro-pores. The good

agreement between the BET and the DR surface areas obtained in this case is somehow unexpected. Capillary condensation of the adsorption gases in the microporosity should be misinterpreted by Bet theory, which in this case would overestimate the sample surface area. On the other hand, indications have been given in the past that N_2 at 77 K hardly reaches the whole microporosity of chars. These counterbalancing effects could lead to the agreement above outlined.

Figure 2 shows the cumulative pore size distribution of the "Spherocarb" on a volume basis. The distribution has been obtained by joining distribution curves from gas adsorption together with results of high pressure mercury porosimetry (Dubinin, 1966; Spitzer et al., 1976). The method of Medek (1977) has been used to determine the size distribution of the micropores. Size distribution of mesopores has been obtained from adsorption data according to the method of Dollimore and Heal (1970). Mercury porosimetry has been used to determine the size distribution of macropores.

2.3 Experimental procedure with EDB

After capture in the EDB each particle was weighed by the technique described in detail elsewhere (D'Amore et al., 1988), and its diameter, density, porosity (D'Amore et al. 1988), surface area (Dudek et al. 1988) measured. The concentration of the gases flowing through the EDB was selected to include 5, 21 or 100% O_2 in N_2 or chromatographic-grade CO_2. The particle was heated by the $^2CO_2$ laser to the desired temperature which was measured by the two color optical pyrometry and continuously recorded. A semicontinuous reaction technique was utilized arresting the reaction by turning the laser off, and measuring at various conversions the physical parameters of the particle.

3. RESULTS

3.1 Microporosity

Theory

The adsorption data have been interpreted using the BET equation in the linear form:

$$\frac{p/p_s}{s(1-p/p_s)} = \frac{1}{s_m c} + \frac{c-1}{s_m c}\,(p/p_s) \qquad (1)$$

where s and s_m are the number of moles of gas adsorbed at relative pressure p/p_s and in a complete monolayer, per unit of sample mass, respectively.

For chars with a high fraction of microporosity, the low- and medium-pressure parts of isotherms are analysed using the Dubinin and Astakhov equation (Dubinin and Astakhov, 1971):

$$\theta = \frac{w}{w_{ts}} = \exp\,[-(A/E)]^h \qquad (2)$$

where w/w_{ts} is the ratio of the micropore volume w filled at pressure p/p_s to the total micropore volume w_{ts}, i.e. the degree of filling of micropores θ; E is the characteristic free energy of adsorption; A is the differential molar work of adsorption and is given by:

$$A = RT \ln(p_s/p) \qquad (3)$$

When w and w_{ts} are expressed in terms of moles of adsorbate s and s_{ts}, respectively, eq. (2) and (3) give:

$$\ln s - \ln s_{ts} = - (RT/E)^h [\ln (p_s/p)]^h \qquad (4)$$

For h=2 eq. (4) reduces to Dubinin-Raduskevitch equation (DR).

According to Medek's analysis (1977) the equation for the differential micropore size distribution is given by:

$$\frac{d\theta}{dr_e} = \frac{dw}{w_{ts} dr_e} = 3h\,(k/E)^h\, r_e^{-(3h+1)} \exp[-(k/E)^h\, r_e^{-3h}] \qquad (5)$$

where θ is the degree of filling of micropores, r_e the pore radius, k, evaluated according to Dubinin's affinity postulate, is equal to $7.51\ 10^{-25}$ cal m^{-3} $mole^{-1}$.

Evolution of "Spherocarb" morphology with reaction

By taking advantage of the special features of the electrodynamic balance, changes in physical characteristics of single "Sperocarb" particles with reaction have been followed.

The volume of micropores w_{ts} of single "Spherocarb" particles have been evaluated from the CO_2 adsorption isotherms at 298 K obtained in an EDB by the use of the DR equation. A complete description of the technique is given by Dudek et al. (1988). These volumes can be related to the surface areas of the micropores (Lamond and Marsh, 1964; Gan et al., 1972; Rand, 1974; Marsh et al., 1975). The char pores volumes are here reported (Figure 3) per unit mass of the particle being measured. In Figure 3, w_{ts} is reported versus fractional conversion f defined as the weight loss divided by the initial mass of carbon, for eight separate single particle "Spherocarb" oxidations. Five of the runs have been performed in oxygen, two in CO_2 and one in air. The reaction temperatures are in the range 750-830 K for reactions in oxygen and 1200-1250 K for reactions in CO_2. The initial specific volume of the micropores vary from 0.203 to 0.276 $cm^3\ g^{-1}$ with the average being 0.237 $cm^3\ g^{-1}$. These specific volumes can be compared to a value of 0.237 $cm^3\ g^{-1}$ obtained on a 0.294 g sample of "Spherocarb" (about 100,000 particles!) by Hurt et al (1988) in a conventional gravimetric apparatus. The specific volumes of the micropores for the 0.294 g sample at conversions of f=0 and f=0.65 for an oxidation run with air are also in Figure 3.

Adsorption can give, in addition to the total microporosities volumes, the pore size distribution by the use of eq. (5). Normalized distributions for fractional conversions f of 0.14, 0.23

and 0.52 for a single particle reacting in air at 770 K are compared in Figure 4 with the distributions for the unreacted char. Although the total microporous volume decreases, the fractional distribution of the residual pores is remarkably constant. This is consistent with the micropore elimination model of Hurt et al., (1988), which was presented with an alternative pore shrinkage model to explain the observation of shrinkage of particles when chemical kinetics are controlling.

3.2 Meso- and macro-porosities

The meso- and macro-porosities are obtained by volume balances on the single particle using measurements of the weight and volume of the particle to obtain total porosity.

Figure 5 shows the single particle porosity ϵ as a function of conversion for the same separate "Spherocarb" oxidations. The porosity values have been obtained from the particle densities by the relation:

$$\epsilon = (1 - \rho / \rho_t) \qquad (6)$$

where ρ is the density of a "Spherocarb" particle at a given conversion and ρ_t is the "Spherocarb" true density. Density measurements were performed discretely using the aerodynamic drag force technique (D'Amore et al., 1988). Initial porosities ranged from 0.56 to 0.68. Although conventional theory would predict particle porosity to increase linearly with conversion under kinetically controlled conditions (zone I) up to ϵ=1, the figure shows that the linearity holds up to a conversion of only 40-50%. A sort of plateau is then approached, consistent with the shrinkage-densification model proposed by Hurt et al. (1988) for chars undergoing regime I or kinetically controlled oxidation.

A particle shrinkage factor Σ has been defined as the ratio of the particle volume V to the initial volume V_0. The Σ values for the eight runs above have been reported in Fig. 6 as a function of conversion. The straight solid line in the figure represents a conventional shrinking, constant density, particle model, while the line at Σ=1 is representative of a purely internal reaction without shrinkage. The data indicates that the extent of "Spherocarb" shrinkage is not a function of temperature, or reacting gas, but only a function of conversion.

The data on total porosity and microporosity obtained in the EDB for a single particle allow one to evaluate the meso- and macropore volume of the particle at a given conversion. This can be done by a volume balance, given by the relation:

$$W = (1/\rho - 1/\rho_t - w_{ts}) (1-f) \qquad (7)$$

where W is the volume of the meso- plus macro-pores per unit initial mass. The results of such an analysis are reported in Fig. 7. In the figure, W has been normalized for each run with the initial value W_0, to account for the different characteristics of the single particles tested. In spite of the large differences in the initial porosity of the single particles (D'Amore et al., 1988), and in the

experimental conditions, clustering of the data points about one curve indicate that the particles all exhibit the same behavior: meso- plus macro-porosity increases with reaction, reaches a maximum at about f=0.3 and eventually decreases to zero at f=1, when the solid is consumed.

The meso- plus macro-pore volume fractions can be separated by utilization of the results of Hurt et al. (1988). Based on electronmicrographs studies of particles reacted to different fractional conversions, visible macropores (diameters greather than 100 nm) were found to have a constant volume fraction as particles shrank during conversion. Utilizing this information we are now in a position to show how the micro-, meso-, and macro-pore volumes change with conversion (Fig. 8), with the microporous volume fraction decreasing, the mesoporous volume fraction increasing, and the macroporous fraction remaining constant. These variations have implications on how the internal surfaces participate in the chemical reaction, which will be a subject of a subsequent paper.

4. CONCLUDING COMMENTS

Pore size distributions have been obtained for single particle using gas adsorption for micropores, the observed constancy of the macropores and a volume balance for the mesopores. The ability of the electrodynamic balance to measure densities of single macroporous particles, without need to differentiate as in conventional liquid displacement methods between macropores and interparticle interstices, provides a ready way for obtaining the mesoporous regime. The results can be depicted graphically as pie charts as shown for three conversions in Fig. 9.

The study provides support for the hypothesis of Hurt et al. (1988) that densification of the microporous regions is due to pore elimination. The interesting finding is the increase in the mesoporous region with increasing conversion, suggesting a crucial role for the mesopores in the reaction.

REFERENCES

- Bar-ziv E., Jones D. B., Spjut R. E., Dudek D. R., Sarofim, A. F. and Longwell, J.P. (1989). Comb & Flame, 75, 81, 1989
- Bellezza, C. (1985). Naples, Dept. of Chem. Eng. Dissertation.
- D'Amore M., Dudek, D.R., Sarofim, A.F., and Longwell J.P. (1988). Powder Tech., 56, 129.
- Davis E.J. and Ray, A.K.(1980). J. Colloid Interface Sci. 75, 566.
- Dollimore, D. and Heal, G.L. (1970). J. Colloid Interfaces Sci. 33, 508
- Dubinin, M.M. (1966) in Chemistry and Physics of Carbon (ed. by P. L. Walker) Vol. 2, p. 86, Marcel Drekker, New York
- Dubinin, M.M. and Astakhov, V.A. (1971). Adv. Chem. Ser. 102, 69
- Dudek, D.R. (1988). Mass. Inst, of Tech. PhD Thesis
- Dudek, E.R., Longwell, J.P. and Sarofim, A.F. (1988) Energy & Fuels, 3, 24.
- Gan, H., Nandi, S.P. and Walker, P.L., Jr. (1972). Fuel. 51, 272
- Gavalas, G.R. (1980). AIChE. 26, 577
- Hurt, R.H., Dudek, E.R., Sarofim, A.F. and Longwell, J.P. (1988). Carbon, 26, 433,
- Kerstein, A.R., and Niksa, S. (1985). Twentieth Symp. (Int.) on

Comb. The Combustion Institute, Pittsburgh, Pa. p. 941
- Lamond, T. and Marsh H. (1964). Carbon. 1, 281
- Marsh, H., Iley, M., Berger, J. and Siemieniewska (1975). Carbon, 13, 103
- Medek, J. (1977). Fuel. 56, 131
- Mohanty, K.K., Ottino, J.M. and Davis, H.T. (1982). Chem. Engng. Sci. 37, 905
- Philip, M.A. (1981). Mass.Inst. of Technology, M.S. Thesis
- Rand, B.J. (1974). J. Colloid Interface Sci. 48, 183
- Reyes, S. and Jensen, K.F. (1986). Chem. Engng. Sci. 41, 333
- Smith, I.W. (1982). Nineteenth Symp. (Int.) on Comb. The Combustion Institute, Pittsburgh, Pa. p. 1045
- Spitzer, Z., Biba, V. and Kadlec, O. (1976). 14, 151
- Spjut, R.E. (1985). Mass. Inst. of Tech. Ph.D. Thesis
- Spjut, R.E., Sarofim, A.F., and Longwell, J.P. (1985). Langmuir, 1, 355.
- Waters, B.J., Squires, R.G., and Laurendeau, N.M. (1988b). Comb. Sci and Tech. 62, 187
- Wuerker, R.F., Shelton, H., and Langmuir, R.V. (1959) J. Appl. Phys., 30, No 3, 342.

LIST OF SYMBOLS

A	differential molar work of adsorption, cal mol^{-1}
E	characteristics free energy of adsorption, cal mol^{-1}
R	gas constant, 1.987 cal mol^{-1}
T	particle temperature, K
V	particle volume, cm^3
V_0	initial particle volume, cm^3
W	single particle meso- plus macropore volume per unit initial mass, $cm^3\ g^{-1}$
W_0	single particle initial meso- plus macropore volume per unit mass, $cm^3\ g^{-1}$
c	parameter in BET equation
f	fractional conversion
h	parameter in Dubinin equation
k	interaction constant in eq.(4). For CO_2 $k=7.51\ 10^2$ cal nm^{-3} $mole^{-1}$.
p	adsorption gas pressure, atm
p_s	adsorption gas saturation pressure, atm
r_e	pore radius, nm
s	amount of gas adsorbed at relative pressure p/p_s, $mol\ g^{-1}$
s_m	amount of gas adsorbed in a complete monolayer, $mol\ g^{-1}$
s_{ts}	amount of gas adsorbed in the total micropore volume, $mol\ g^{-1}$
w	micropore volume per unit particle mass filled at pressure p/p_s, $cm^3\ g^{-1}$
w_{ts}	total micropore volume per unit particle mass, $cm^3\ g^{-1}$
ϵ	single particle porosity
θ	degree of filling of micropores
ρ	apparent particle density, $g\ cm^{-3}$
ρ_t	true particle density, g cm^{-3}
Σ	particle shrinkage factor

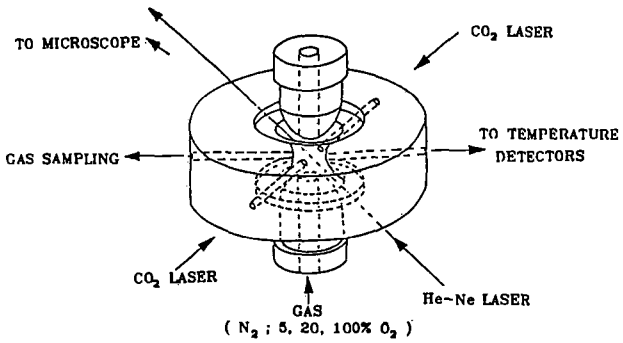

Fig. 1 - The Electrodynamic Thermogravimetric Analyser

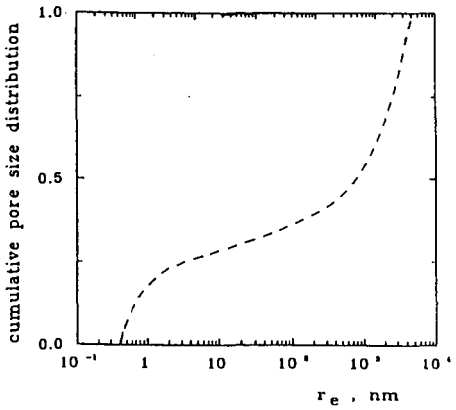

Fig. 2

Cumulative pore size distribution on volume basis

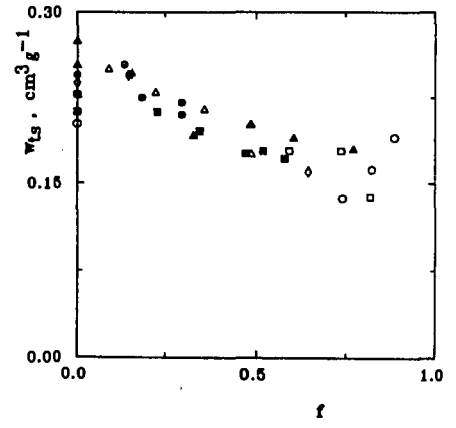

Fig. 3

Eight separate aingle particle "Spherocarb" oxidations in EDTGA.
Micropores volume per unit particle mass as a function of conversion.

◇ ▲ △ ○ □ 100% O_2
● ◒ 21% O_2
■ 100% CO_2

▨ 100,000 "Spherocarb" particles oxidation with 21% O_2 in CTGA.

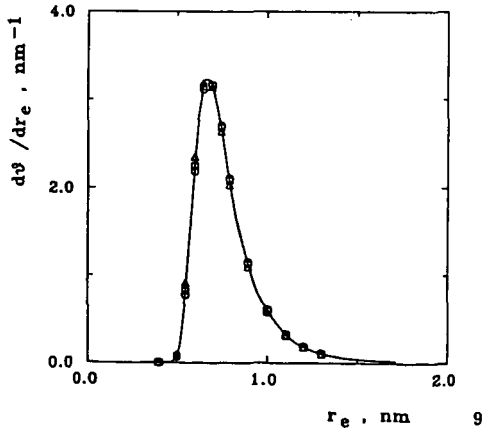

Fig. 4

Single particle "Spherocarb" oxidation with 21% O_2 in EDTGA.
Micropores size distribution at various conversions.

△ f = 0.14
□ 0.23
○ 0.52
solid line unreacted char

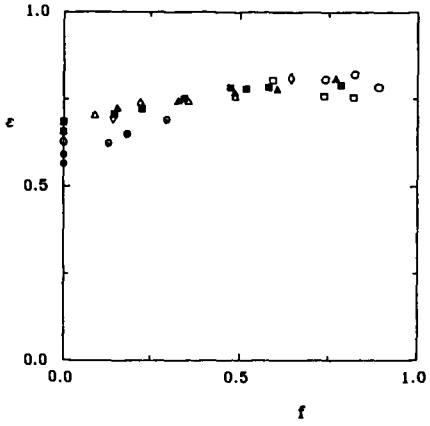

Fig. 5

Eight separate single particle "Spherocarb" oxidations in EDTGA.
Particle porosity as a function of conversion.
◇ ▲ △ ○ □ 100% O_2
● ◒ 21% O_2
■ 100% CO_2

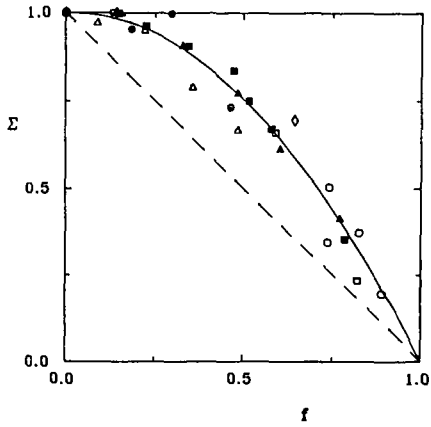

Fig. 6

Eight separate single particle "Spherocarb" oxidations in EDTGA.
Particle shrinkage factor as a function of conversion.
◇ ▲ △ ○ □ 100% O_2
● ◒ 21% O_2
■ 100% CO_2
dashed line shrinking core model
solid line best fit line

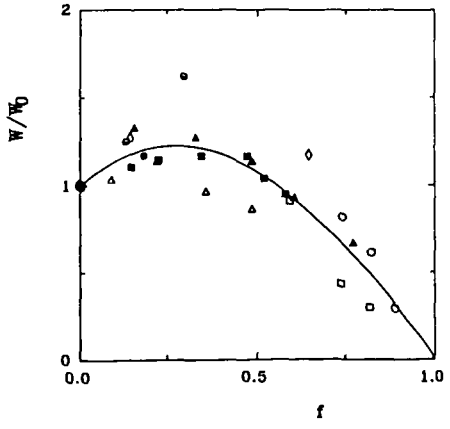

Fig. 7

Eight separate single particle "Spherocarb" oxidations in EDB.
Particle meso- plus macropore volume per unit initial mass, normalized in respect to the value at f=0, as a function of conversion.
◇ ▲ △ ○ □ 100% O_2
● ◒ 21% O_2
■ 100% CO_2
solid line best fit line

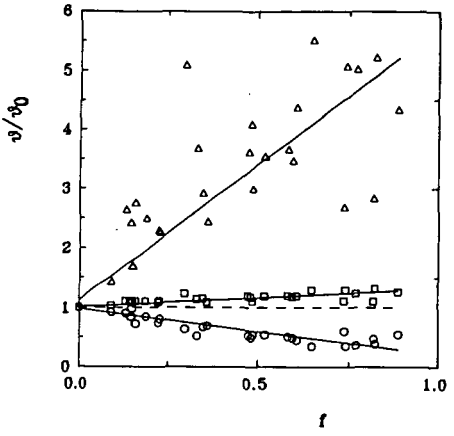

Fig. 8 - Eight separate single particle "Spherocarb" oxidations in EDB.
Pores volume fractions, normalized with respect to the value at f=0, as a function of conversion.

□ total pores volume fraction
--- macropores
△ mesopores
○ micropores

Fig. 9 - Single particle "Spherocarb" oxidation in EDB.
Volume fraction of porea and carbon at various conversions.

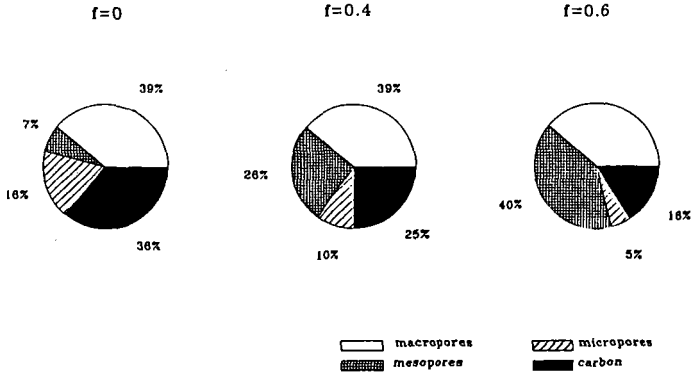

ON THE COMBUSTION KINETICS OF HETEROGENEOUS CHAR PARTICLE POPULATIONS*

R. H. Hurt and R. E. Mitchell**
Combustion Research Facility
Sandia National Laboratories, Livermore, CA 94551-0969

Keywords: coal, combustion, kinetics

An optical technique has previously been used to measure, *in situ*, the temperatures, sizes, and velocities of individual pulverized-coal char particles.[1-3] A model of mass and energy transport processes to and from the burning char particles was used to derive burning rates and kinetic parameters from the single-particle measurements. In the past, the measured joint distribution of particle temperature and size was divided into narrow size fractions, and global kinetic parameters were determined from the average temperatures and sizes in these fractions.[2,3] An effort is currently underway to extract additional information from the existing extensive data base by computing and analyzing burning rates and rate coefficients for *individual* particles derived directly from the single-particle temperature measurements. In the present article, single-particle rate coefficients are computed from optical measurements on char from Pocahontas #3 coal†, and techniques for the determination of kinetic parameters from the single-particle coefficients are investigated.

RESULTS

A laboratory-scale laminar-flow reactor was used to investigate the combustion of Pocahontas #3 low-volatile bituminous coal particles (nominal diameter range 106 -124 μm) in gas environments containing 6 or 12 mole-% oxygen over the range of gas temperatures 1500 -1700 K. An optical particle sizing/pyrometer was used to measure single-particle temperatures, sizes, and velocities during the char combustion phase (subsequent to devolatilization). Char particle sizes differ from the nominal coal particle size due to both swelling during devolatilization and surface carbon consumption. A model of mass and energy transport processes was used to extract burning rates and kinetic parameters from the single-particle optical measurements. The model treats unsteady radiative and convective heat transfer between the particle and its surroundings as well as oxygen transport to the particle surface, accounting for the effect of Stefan flow. The principle and operation of the optical particle sizing/pyrometer and the transport model are discussed in detail elsewhere.[1-3] Char oxidation kinetics are represented here by a rate law of the form:

$$q = k_s P_s^n = A\, e^{(-E/RT_p)}\, P_s^n \qquad (1)$$

where q is the burning rate per unit external particle surface area, and k_s is a global coefficient embodying the combined effects of internal surface area, pore diffusion, and intrinsic surface reactivity. The combustion behavior of a given coal char is described by the set of three global kinetic parameters, n (reaction order), E (activation energy), and A (preexponential factor).

Single-particle rate coefficients

At each measurement location in the flow reactor (i.e. at successive particle residence times), the optical technique recorded a distribution of particle sizes and temperatures. Standard deviations typically observed were 20 μm in particle diameter and 40 to 120 K.

* Work supported by the U.S. Department of Energy's Pittsburgh Energy Technology Center's Direct Utilization AR&TD Program.

** Present address: Department of Mechanical Engineering, Stanford University, Stanford, CA 94305-3032

† The Pocahontas #3 coal was obtained from the Pennsylvania State Coal Bank (designation PSOC-1508), through the Pittsburgh Energy Technology Center, and is one in a suite of ten coals under study within the Sandia Coal Combustion Science Program.

in particle temperature. In Figure 1, single-particle rate coefficients derived from the optical data on Pocahontas #3 coal, are plotted as a function of temperature, in Arrhenius form†. A characteristic feature of this and other Arrhenius plots of single-particle rate constants is the presence of distinct linear groupings of points associated with a given gas composition and a given measurement location in the reactor. These linear groupings generally exhibit slopes that are steeper than the kinetic rate expression fit to the entire data set. As a result of this feature, data taken in only a single gas environment (e.g. 12-mole% O_2) produce activation energies generally higher than those determined from a simultaneous regression of data in several gas conditions.[4]

In Figure 2, single-particle rate constants are plotted for the same data set, but for the optimum (least squares) reaction order, $n = 0.0$. By varying the reaction order, the data from Fig. 1 have been partially collapsed to a single curve. Experience with similar data for a number of coals indicates that it is often possible to find a reaction order that at least partially collapses the data from different measurement locations. For some data sets, however, no value of n collapses the data onto one curve, resulting in a kinetic expression (a set of values for n, E, and A) that does not adequately describe the entire data set. In either case, the basic trend toward collections of distinct lines with higher slopes is apparently an intrinsic property of Arrhenius plots of single particle combustion rate constants. The origin of this feature will be explained in the next section.

DISCUSSION

Characteristic curves on Arrhenius diagrams

Let us consider a simplified analysis that ignores the effect of Stefan flow (a minor correction) and assumes the particles to be in thermal equilibrium with their environment. Under these conditions, given a reaction order n, the equations governing mass and energy transport can be algebraically manipulated to arrive at the following explicit expression for the single-particle rate constant, k_s.

$$k_s = \frac{\left[\frac{Nu\lambda}{H_{rxn}\, d_p}(T_p - T_g) + \frac{\varepsilon_p \sigma}{H_{rxn}}(T_p^4 - T_w^4)\right]}{\left[P_g - \frac{d_p R(T_p + T_g)}{48 D_{ox}}\left(\frac{Nu\lambda}{H_{rxn}\, d_p}(T_p - T_g) + \frac{\varepsilon_p \sigma}{H_{rxn}}(T_p^4 - T_w^4)\right)\right]^n} \qquad (2)$$

From Eq. 2 k_S is a function of the following variables: T_p, d_p, T_g, P_g, T_w, n, D_{ox}, λ, ε_p, H_{rxn}. For a given operating condition at a given measurement height, T_p and P_g are fixed, as are T_w and the properties of the gas D_{ox} and λ, and the heat of reaction, H_{rxn}. For coal particles with an emissivity ε_p, k_s is a function only of T_p, d_p, and n. If one fixes the reaction order, n, and considers only particles of a given size, d_p, Eq. 2 reduces to a relationship between T_p (which is measured in the laboratory) and k_s, (the derived quantity of interest, the single-particle rate coefficient). In a plot of k_s as a function of $1/T_p$, Eq. 2 defines a characteristic curve representing the mass and energy balances for the reacting char particle.

An example of such a characteristic curve is the leftmost trace in Fig. 3, calculated for the specific case: $d_p = 150$ μm, $\varepsilon_p = 0.8$, $T_g = 1645$ K, and $P_g = 0.12$ atm (corresponding to the 12.7 cm measurement height in the laminar flow reactor in the 12 mole-% O_2 gas environment). It is important to note that the characteristic curves are functions of the reaction order, n, but not of the other kinetic parameters, A and E. Also in Fig. 3 are data points corresponding to the 140-160 μm size fraction (a subset of the data in Fig. 1),

† Single-particle rate coefficients can be calculated from the optical data directly if the reaction order, n, is specified. A value for the reaction order of 1/2 was chosen arbitrarily for this example. Also, the results presented in Figures 1 - 4 were generated by a simplified analysis technique which assumes that CO is the only combustion product and that the particles are in thermal equilibrium with their environment.

superimposed on the theoretically derived characteristic curves for d_p = 150 μm. This particular linear grouping from Fig. 1 is seen to lie, as it must, along a characteristic curve representing the mass and energy balance equations for reacting char particles. The characteristic curves have the following features: at low particle reactivity (low k_s) the burning rate is insufficient to generate enough heat to affect the particle temperature - the temperature in this "nonburning" regime is nearly independent of k_s (see the nearly vertical curve segments at the bottom of Fig. 3), and accurate values of k_s cannot be extracted from the measured particle temperatures. For moderate particle reactivity (moderate k_s), the surface reaction generates sufficient heat to raise the particle temperature well above the nonburning temperature. In this region particle temperature is sensitive to k_s and the burning rates and kinetic parameters can be derived from the measured particle temperatures (see the sloped portion of the curves in the center of Fig. 3). At high particle reactivity (high k_s), particles burn so rapidly that oxygen is thoroughly depleted at the particle surface and an asymptotic temperature is reached associated with diffusion-limited or zone III burning. In this region the temperature again becomes insensitive to k_s, and extraction of accurate values of k_s from measured particle temperatures is no longer possible (see the vertical curve segments at the top of Fig. 3).

The characteristic curves exhibit many of the same features as plots of k_s vs. χ used by Smith[5], where χ is the ratio of the observed burning rate to the maximum, diffusion-limited rate. Data points that lie in the nearly vertical upper or lower segments of the characteristic curves correspond to high and low values of χ respectively, For the determination of the kinetic parameters, only values within a chosen χ range (typically $0.2 < \chi > 0.85$) are used, corresponding to points that lie on the central, nearly linear segment of the curves.

Families of characteristic curves for a particle size distribution

It was shown in the previous section that rate constants, k_s, for individual burning particles of a given size, d_p, lie on characteristic curves on the Arrhenius diagram representing mass and energy balance equations for the reacting particles. In practice, even though size-graded coal is fed to the reactor, the devolatilization process broadens the particle size distribution to such an extent that the size dependence of char reactivity must be considered.

In Fig. 4 characteristic curves are presented for various particle sizes at two selected experimental conditions. Also appearing on Fig. 4 are single-particle rate constants for all particle sizes from Fig. 1, superimposed on the characteristic curves. The figure illustrates how a distribution of particle sizes at a given measurement height gives rise to a family of characteristic curves on the Arrhenius diagram. The range of particle sizes considered (100 - 200 μm) produces, for each condition, a band that contains essentially all of the measured points. There is a significant size dependence in the upper and lower extremes of the curves due to the size dependence in the convective mass and heat transfer coefficients in Eq. 2. In the central region, however, from which kinetic data are extracted, particle temperatures are only weakly size dependent and the family of curves converges to a narrow band. The measured rate constants (points) are therefore seen to lie in nearly linear groupings within the narrow bands formed by the nearly linear segments of the characteristic curve families.

It can therefore be concluded that the distinct linear groupings clearly seen in Arrhenius plots of single-particle rate constants are the outlines of the nearly linear sections of characteristic curves, with the particle size distribution causing a limited scatter about a central curve corresponding to the median particle size. These linear groupings of points, like the theoretical characteristic curves they follow, are a function of the reaction order, n, *but not the actual global kinetic activation energy E or preexponential factor, A.* The global kinetic activation energy and preexponential factor determine, rather, *where* along these curves the measured points will lie.

Implications for kinetic studies

With this background on characteristic curves, let us consider how kinetic parameters can be extracted from measurements of single-particle sizes and temperatures. A large number of single particle temperatures are measured and the model (represented here by a series of characteristic curves) is used to determine a value of k_s for each particle. As a consequence of the analysis procedure, each point on the Arrhenius diagram corresponding to a single-particle measurement from the laboratory must lie on one of the characteristic curves. This is true irrespective of the accuracy in the data - random measurement errors cause the data not to scatter *about* the characteristic curves, but to distribute *along* characteristic curves.

If kinetics are to be measured for a system in which each particle obeys a single rate law, for example the Arrhenius law, the individual data points will be the intersections of the line representing the Arrhenius rate law (Eq. 1) and the appropriate characteristic curve representing the particle mass and energy balance equations (Eq. 2). Because these curves intersect at only one point, there is only one particle temperature and one value of k_s that satisfy both the rate law and the mass and energy balances. The rate expression obtained by regression of the data will be a locus of experimental points lying on different characteristic curves.

In practice, particle-to-particle variations in properties and reactivity result in a distribution of particle temperatures at each location, producing a distribution of points along a characteristic curve, appearing as a distinctly recognizable line of slope $\beta = d(\ln k_s)/d(1/T_p)$. From the definition of the activation energy:

$$E \equiv -R \frac{d\ln k_s}{d(1/T_p)} \tag{3}$$

it is clear the the data at one experimental condition exhibit a pseudo activation energy of $-R\beta$. The slope, β, is a property of the associated characteristic curve and can be obtained by direct differentiation of Eq. 2. Examination of Eq. 2 reveals that this pseudo activation energy, $-R\beta$, associated with a given reactor height, is a function of T_p, d_p, T_g, P_g, n, T_w, D_{ox}, λ, ε_p, and H_{rxn}.

The pseudo activation energy for data from a single measurement location is therefore a function of the reaction order, properties of the gas phase, and physical properties of the char particle, *but is independent of the actual global kinetic activation energy, E*. From this we can conclude that the temperature distribution observed in a given experiment at a single measurement location contains little or no information on the activation energy.† It is primarily in the comparison of data points taken at different measurement locations that the true information on the pressure dependence (n) and the temperature dependence (E) of the char combustion rate lies.

When a single Arrhenius rate law is fit to all experimental points simultaneously, optimal (least-squares) coefficients are influenced by particle-to-particle variations in properties and reactivity, manifested in the presence of the characteristic curve segments of generally higher slope. The regression routine attempts, in effect, to fit both the true kinetics and the characteristic curve segments simultaneously. The least-squares parameters obtained will be influenced both by the kinetic parameters (A,E,n), and by the properties of the characteristic curves. In practice, the presence of the linear groupings of single-particle rate coefficients affects the data regression in the following manner: Both the characteristic curves and their derivatives are functions of n, the reaction order. A comparison of Figs. 1 and 2 illustrate that the slope, and thus the pseudo activation energy at one height, tends to decrease with increasing n. Extraction of a rate law by regression of the entire set of single-

† Limited kinetic information is contained in the observed dependence of temperature on particle size at one measurement location.

particle data often results in artificially low reaction orders, because low orders produce characteristic curves of lower slope that are more closely comparable to typically observed activation energies for oxidation of impure carbons (typically 15 - 25 kcal/mole in zone 2). A parameter set (A,E,n) with low n partially collapses the data onto nearly parallel, closely spaced characteristic curves, resulting in a lower RMS error (see Fig. 2).

The extent to which particle-to-particle variation in properties and reactivity influences the kinetic parameters can be seen by repeating the analyses for Figs. 1 and 2 with data sets formed by various temperature averaging strategies. Table 1 presents the results of applying an identical analysis technique to three different data sets derived from the original measurements of single particle temperatures, sizes, and velocities for Pocahontas #3 coal:

1. individual particle sizes and temperatures
2. average sizes and temperatures in 10 μm size bins
3. overall median particle sizes and temperatures at each experimental condition and measurement location.†

An optimal value of the reaction order was determined by minimizing the sum of the squared residuals in k_s. Table 1 shows a sharply increasing value of n with an increasing degree of temperature averaging. Averaging decreases the amount of scatter along characteristic curves and thus reduces the biasing effect on the kinetic parameters. The use of average temperatures in 10 μm size bins reduces the length of the characteristic curve segments and thus reduces the biasing effect, but does not eliminate it. Use of the overall median values, corresponding to a reaction order of 0.75, is believed to yield unbiased results for this data set.

Recommended Technique for Determination of Kinetic Parameters

The distribution of particle temperatures at one measurement location reflects the effects of particle size and of particle-to-particle variations in both physical properties and reactivity. For the Pocahontas coal char the effect of variations in particle size is quite small. To understand the origin and evolution of the observed temperature distributions, a more detailed statistical treatment is needed that explicitly considers particle-to-particle variations in both physical properties and reactivity. Gavalas and Flagan[6] have used a statistical model of char combustion to describe variability in temperature traces of individual burning coal particles.

For the more limited practical goal of predicting overall burning rates for the particle population over narrow to moderate ranges of carbon conversion, kinetic parameters describing the combustion behavior of "typical" particles in the population (those of median reactivity) is often sufficient. It has been shown here, that even this limited goal cannot be attained by direct application of nonstatistical analyses to single-particle measurements. The presence of the particle temperature distributions has been shown to introduce a systematic bias in the determination of kinetic parameters, resulting for this example, in artificially low reaction orders. In the following paragraphs, a simple analysis technique is recommended that avoids this bias and yields kinetic parameters describing the combustion of "typical" particles within a heterogeneous particle population.

In general, the joint size/temperature distribution measured by the single-particle optical technique contains valuable information on the kinetic parameters A,E, and n. There is, however, often a wide variation in temperature within a particle size fraction, which has been shown to systematically bias kinetic analyses. Classifying the single-particle data into narrow size bins preserves much of the information in the T_p-d_p relationship, but produces average temperatures for each size bin that are based on few data points. The averages therefore contain a significant fraction of the scatter present in the original temper-

† These three optimum reaction orders were determined by a kinetic analysis that assumed CO to be the only combustion product, but accounted for the influence of particle thermal inertia on the heat balance (a term arises for thermal inertia when the particles traverse regions of changing gas temperature or properties).

ature distribution, according to Eq. 4:

$$\sigma_{T_{ave}} = \sigma_T/\sqrt{N} \qquad (4)$$

where σ_T is the standard deviation in the measured temperature distribution and $\sigma_{T_{ave}}$ is the standard deviation of the averages computed from N experimental points. Wide size bins, on the other hand, produce accurate estimates of the average temperatures (reducing the bias associated with the distinct lines) but sacrifice much of the information contained in the T_p-d_p dependence. For a given experiment, there is an optimum width for the size bins that results in the most accurate determination of the kinetic parameters A,E, and n.

A simple statistical technique for determination of n^{th}-order kinetic parameters was developed and used that achieves the proper balance between temperature averaging and preservation of information contained in the joint size/temperature distribution. The single-particle data was divided into only two size categories: one containing particles between the 0^{th} - 50^{th} size percentiles (with a median at the 25^{th} percentile) and a second containing particles between the 50^{th} - 100^{th} size percentiles (with a median at the 75^{th}). Median sizes and temperatures are obtained for each of the two categories by a sorting routine and are combined with the overall median size and temperature to yield the data set for regression. Rate parameters for the Pocahontas coal determined by the technique outlined above are presented in Fig. 5. The full analysis of Mitchell[3], including the effects of thermal inertia, Stefan flow, and partial CO_2 production at the particle surface was applied. The reaction order was determined to be 0.75 by least squares regression and the CO/CO_2 ratio was adjusted to fit the measured mass-loss profiles using the correlating expression $CO/CO_2 = A_c e^{(-E_c/RT)}$. Inclusion of some CO_2 production improves the fit to the conversion profile and average values of ψ, the fractional molar conversion to CO_2, are reported in Fig. 5 for the two gas environments (6, 12 mole-% oxygen).

CONCLUSIONS

Particle-to-particle variations in properties and reactivity often give rise to a broad distribution of char particle temperatures at a given location in a combustion environment. This distribution of particle temperatures is shown to produce distinct characteristic curves or bands of points on Arrhenius plots of single-particle rate constants. These linear features exhibit pseudo activation energies that are independent of the actual global kinetic activation energy. A complete description of single-particle combustion behavior will require a detailed statistical treatment that explicitly accounts for the origin and implications of the observed temperature distributions. Accounting for particle-to-particle variations in reactivity and properties may be key to understanding reactivity at high carbon conversions. For the more limited goal of predicting overall burning rates for the entire particle population over narrow to moderate ranges of carbon conversion, kinetic parameters describing the combustion behavior of "typical" particles (those of median reactivity) is often sufficient. It has been shown here, that even this limited goal cannot be attained from single particle measurements without careful statistical considerations. The observed particle-to-particle variations in properties and reactivity are shown to dramatically bias the global kinetic parameters determined by nonstatistical analysis. A simple analytical procedure is demonstrated that extracts the true kinetic information for particles of median reactivity within a heterogeneous particle population.

LITERATURE

1. Tichenor D. A., Mitchell R. E., Hencken K. R., and Niksa S. 20^{th} *Symp. (Int.) Comb. 1213 (1984)*
2. Mitchell, R. E. and Madsen, O. H. *21^{st} Symp. (Int.) Comb.* 173 (1986)
3. Mitchell, R. M. *22^{nd} Symp. (Int.) on Comb.*, 69 (1988)
4. Mitchell, R. M., and D. R. Hardesty, in *Coal Combustion Science--Quarterly Progress Report*, Hardesty, D. R. (ed.), Sandia Report SAND89-8250 (1989).
5. Smith, I. W., *19^{th} Symp. (Int.) on Comb.* 1045 (1982)
6. Gavalas, G. R. and Flagan, R. C. "Kinetics of Coal Combustion Part III: Mechanisms and Kinetics of Char Combustion," Final Report to the Dept. of Energy, Rpt.# TRW S/N 44617

NOMENCLATURE

A	preexponential factor	R	gas constant
A_c	preexponential factor in the correlation for CO/CO_2 ratio	T_g	gas temperature
		T_p	particle temperature
d_p	particle diameter	T_w	wall temperature
D_{ox}	oxygen diffusivity	v_g	gas velocity
E	global kinetic activation energy for char oxidation	v_p	particle velocity
		Greek Symbols	
E_c	activation energy in the correlation for CO/CO_2 ratio	β	slope of characteristic curve
		ϵ_p	particle emissivity
H_{eff}	heat of combustion reaction	λ	thermal conductivity of the gas phase
k_s	rate constant	Nu	Nusselt number
n	reaction order	σ	Stefan-Boltzmann constant
P_g	partial pressure of oxygen in the bulk gas	σ_T	standard deviation of measured temperature
P_s	partial pressure of oxygen	σ_{Tave}	standard deviation of average temperature
q	burning rate per unit area of external surface	χ	ratio of observed to maximum burning

Table 1. Optimum Reaction Order for Oxidation of PSOC-1508 Char Determined From Three Different Data Sets

Data Set used in Regression	*Reaction order*
All single-particle sizes and temperatures	0.00
Average sizes and temperatures in 10 μm size bins	0.16
Overall median sizes and temperatures	0.75

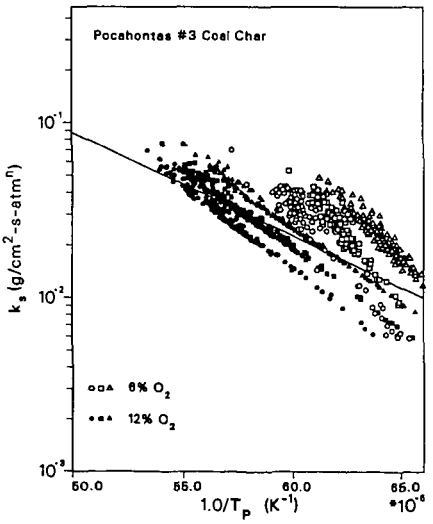

Figure 1. Rate constants for individual burning char particles from Pocahontas #3 (PSOC-1508) coal: Reaction order, n, = 1/2. Initial coal particle diameters 106 - 125 μm. Reaction product assumed to be CO. Symbols correspond to various measurement heights (particle residence times): circles: 12.7 cm; squares: 19.1 cm; triangles 25.4 cm.

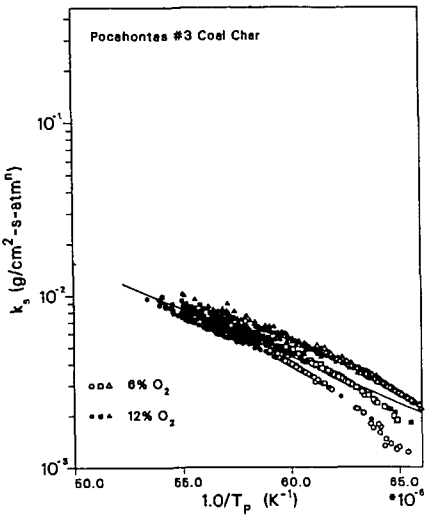

Figure 2. Rate constants for individual burning char particles from Pocahontas #3 (PSOC-1508) coal: optimum reaction order, n = 0.0. Initial coal particle diameters 106 - 125 μm. Reaction product assumed to be CO. Symbols correspond to various measurement heights (particle residence times): circles: 12.7 cm; squares: 19.1 cm; triangles 25.4 cm.

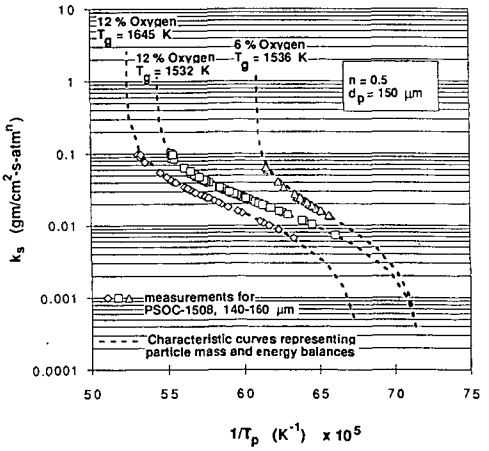

Figure 3. Characteristic curves and experimentally determined single-particle rate constants for PSOC-1508 Pocahontas #3 coal. Curves for 150 μm particles; points for particles with diameters 140 - 160 μm. Reaction order, n, ≈ 1/2.

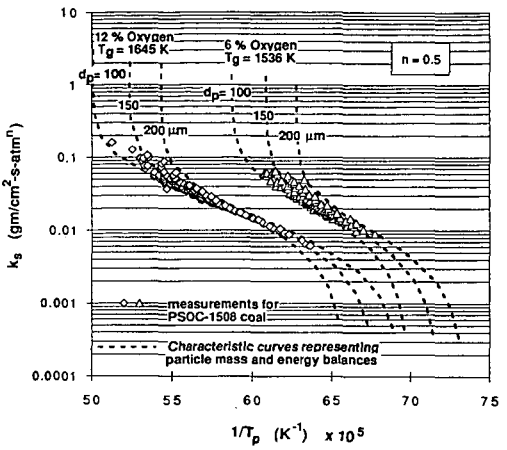

Figure 4. Families of characteristic curves for a particle size distribution and experimentally determined single-particle rate constants for PSOC-1508. Reaction order, n, = 1/2.

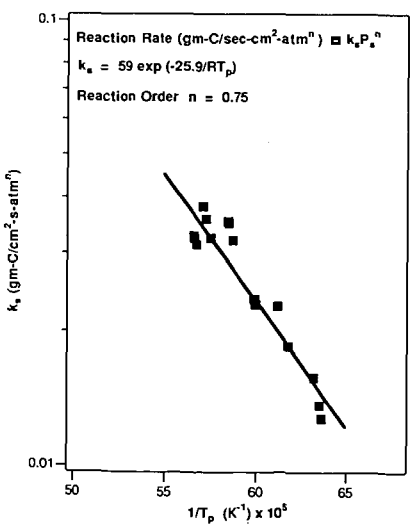

Figure 5. Global kinetic parameters for PSOC-1508 Pocahontas #3 low-volatile bituminous coal. Points represent rate coefficients calculated by the recommended simple statistical technique.

INFLUENCE OF MACERAL COMPOSITION OF RAW COAL ON POTASSIUM ACTIVITY IN STEAM GASIFICATION OF CHARS

V. Calemma, G. Del Piero and G. Passoni
Eniricerche,20097, S. Donato Milanese,
Milan, Italy

Keywords: potassium; coal gasification; steam

INTRODUCTION

The catalytic effect of potassium salts on steam gasification rate of coal chars, is one of the subjects in the field of coal gasification most widely investigated because of their potential application in commercial processes. The results of research activity,have pointed out that the catalytic activity of potassium depends upon several factors such as associated ion, mineral matter, rank of parent coal, pretratment conditions and K/C ratio[1]. As regards the latter, literature data show that gasification rates increase with potassium content until a particular value is reached after which higher values are ineffective or lead to a decrease in reactivity [2]. Moreover, it has been reported that the value of catalyst concentration at which the gasification rate saturates depends on the identity of the substrate and the procedure used to prepare the doped char[3]. The objective of the work reported here was to investigate the influence of maceral composition of the parent coal on the catalytic behavior of potassium carbonate in steam gasification of chars.

EXPERIMENTAL

Four coals were used in this study: three bituminous coals (Illinois N°6, Middelburg (S.A), Polish) and a subbituminuos Sulcis coal. Table 1 shows their maceral composition and the respective rank determined by petrographic analysis. In all cases K_2CO_3 was added to the coals by mechanical mixing before pyrolysis. A known amount of powered catalyst was added to the coal (150 - 300 μm), homogenized and then charrified at 1073 °K for 2 h under nitrogen

flow. After pyrolysis the doped chars were ground, sieved and the fraction 150-300 μm was used for this study. Potassium loading on chars was determined by AES-ICP technique on the solution obtained after an oxidizing treatment with HNO_3-H_2O_2 solution of doped samples.The kinetic experiments were carried out under a steam pressure of 3,6 MPa using a small bench-scale apparatus with a semicontinuous fixed-bed reactor consisting of 0.0127 m i.d., 0.7m long stainless steel pipe, water precision pump and steam preheater. After loading the reactor with the doped char the temperature was raised (flowing N_2) to the desired value and then the sample was reacted stopping the nitrogen flow and pumping water. The reaction temperature was 1018 °K for chars obtained from Polish coal and 973 °K for those from Illinois N°6, Sulcis, and Middleburg coals. After water removal, the product gas was sampled and analyzed by a gaschromatograph. Reactivity during gasification was determined by measuring the reaction rate (mol* h^{-1}) normalized with respect to the initial moles of carbon in the sample.

RESULTS AND DISCUSSION

The catalytic activity of K_2CO_3 towards steam gasification of the coal chars with different catalyst concentration was evaluated determining the reaction rate at 50% conversion. The relationships between reactivity and K/C ratio , shown in figure 1, point out a different trend for the chars examined. Leaving out the first part of the curves whose lower slopes are mainly due to the reaction of potassium with mineral matter[4], chars from Sulcis and Illinois N°6 coals display a linear correlation in the whole range of catalyst concentration.Differently, in the case of chars from Middleburg and Polish coals the concentration of active sites increases linearly with catalyst concentration up to a limit value after which further addition of catalyst is less effective. Studies carried out by several investigators using different substrates have yielded some conflicting results. For example Wigmans et al.[5] reported a linear increase of reactivity with catalyst loading up to 40%w. In contrast other authors [6,7] have found that gasification rates saturate at much lower K/C ratios. Generally the variation of saturation limit has been explained in terms of different preparation methods used to load the catalyst, potassium

volatilization or micropore blockage by catalyst [2,3,6,7]. In our case the preparation method was always the same and no loss of potassium was detected during gasification experiments. All this strongly suggests that besides the above mentioned factors, the value of K/C ratio at which the catalyst begins to be less effective should be also dependent on the particular features of the substrate and the interactions between catalyst and coal during the pyrolysis step. The results of petrographic analyses of the coals used in this study, listed in table 1, point out that the vitrinite content in Illinois N°6 and Sulcis coals is remarkably higher than in Polish and Middelburg coals. In this connection it is interesting to note that the decrease of catalytic activity of potassium after a given value of K/C ratio occurs only with the chars obtained from the two coals having the lowest vitrinite content. During the pyrolysis process (with or without catalyst) vitrinite undergoes to substantial changes of its chemical composition, porous structure and morphology which leads to the development of macroporosity whereas the inertinite remains almost unchanged. This situations is illustrated in figures 2, 3, 4 and 5 which show vitrinite and inertinite fragments before and after pyrolysis.It is known that upon heating the catalyst becomes extremely mobile and spreads over the accessible carbon surface through the porous system [8]. On this ground, it follows that the porosity originated during the pyrolysis step promote the contact between catalyst and the "support" and the distribution of potassium in the char matrix. An example is given in figure 6 where the oblique section of a vitrinite fragment shows how the pores can be easily penetrated by the catalyst during pyrolysis. On the contrary inertinite fragments do not develop macroporosity upon heating (fig. 7) and therefore it is reasonable to expect that higher contents of this maceral could lead to a lower ability of the coal to allow a constant dispersion of increasing quantity of catalyst. The examination of doped char samples by electron microscopy and microanalysis (SEM+EDS) confirms the hypothesis reported above.Indeed figures 8 and 9 show that the distribution of potassium on the surface of chars obtained from Polish coal is uneven and regions with higher potassium concentration are mainly those formed by pyrolysis of vitrinite. All this is particularly clear in figure 8 which shows a pyrolyzed inertinite fragment free

of potassium close to a "vitrinite" fragment with a high concentration of catalyst.

Conclusions

It has been demonstrated that regions of enhanced reaction rate are those associated with the interface between the "support" and added catalyst [9], therefore from a general point of view the existence of a linear relationship between reaction rate and K/C ratio implies a constant dispersion degree of the catalyst. In our case the porous system of the char through which the catalyst is dispersed is mainly the result of changes undergone by the vitrinite and its interaction with K_2CO_3 during the pyrolysis step. Hence the ability of a given char to allow a constant dispersion degree of increasing quantity of catalyst, besides the feature of the porous system and its evolution during gasification, will be also affected by the vitrinite content of the parent coal.

References

1. B.J. Wood and K.M. Sancier, Catal. Rev.-Sci. Eng. 26, 233 (1984)
2. D.A. Sams and F. Shadman, Fuel 62, 880, (1983)
3. C.A. Mims and J.K. Pabst, Am. Chem. Soc., Fuel Chem. Div. Prep. 25(3), 258 (1980)
4. G. Bruno, M. Buroni, L. Carvani, G. Del Piero and G. Passoni Fuel 67, 67 (1988)
5. T. Wigmans, R. Elfring and J.A. Moulijn, Carbon 21, 1 (1983)
6. D.A. Sams, T. Talverdian and F. Shadman, Fuel 64, 1208 (1985)
7. B.C. Gorrini, L.R. Radovic and A.L. Gordon, Fuel 69, 789 (1990)
8. P.R. Abel, B.J. Waters, P.C. Koenig, R.G. Squires and N.M. Laurendeau Fuel 64, 613 (1985)
9. D.J. Coates, J.W. Evans, A.L. Cabrera, G.A. Somorjai and H. Heinemann J. Catal. 80, 215 (1983)

Table 1. Maceral analyses of coals(*)

Coal	Vitrin.	Inert.	Liptin.	Reflect.%	Rank
Sulcis	93	1	6	0.49	Subbitum.
Illinois N°6	94	3	3	0.58	HVB-C
Polish	53	38	9	0.92	HVB-A
Middelburg	48	46	6	0.64	HVB-C

(*) Data are given on mineral matter free basis (% volume).
Reflectance percentages refer to vitrinite macerals
HVB: High volatile bituminous

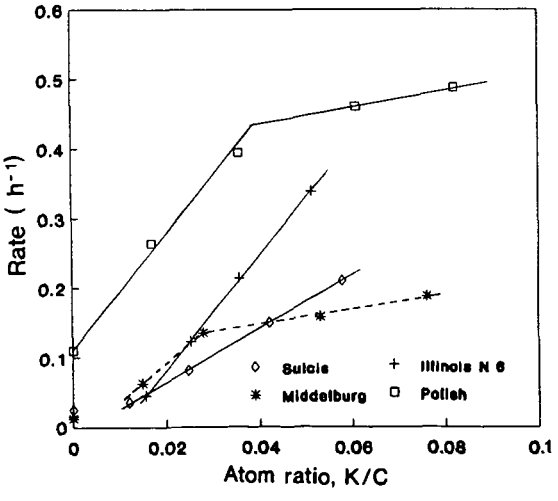

FIGURE 1. CATALYTIC EFFECT OF K_2CO_3 ON GASIFICATION RATES

FIGURE 2 FRAGMENT OF VITRINITE IN RAW COAL

FIGURE 3 FRAGMENT OF PYROLYZED VITRINITE

FIGURE 4 FRAGMENT OF FUSINITE (INERTINITE) IN RAW COAL

FIGURE 5 FRAGMENT OF PYROLYZED FUSINITE (INERTINITE)

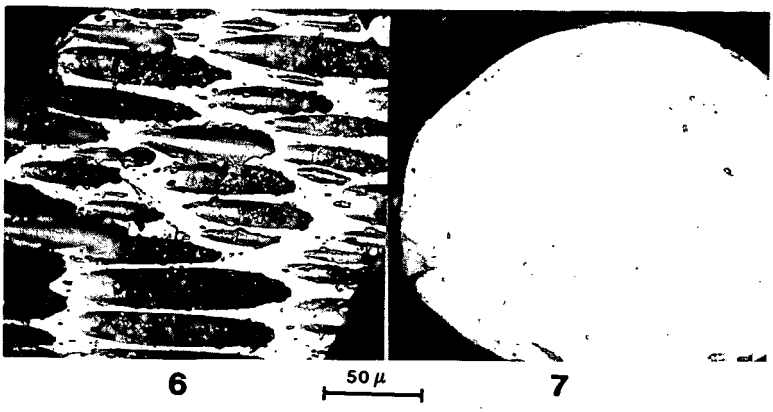

FIGURE 6 FRAGMENT OF PYROLYZED VITRINITE

FIGURE 7 FRAGMENT OF PYROLYZED MACRINITE

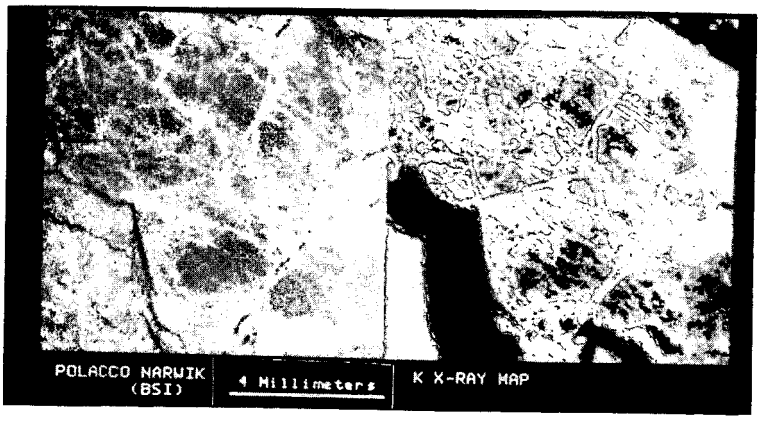

FIGURE 8. POTASSIUM DISTRIBUTION MAP OF DOPED POLISH CHAR

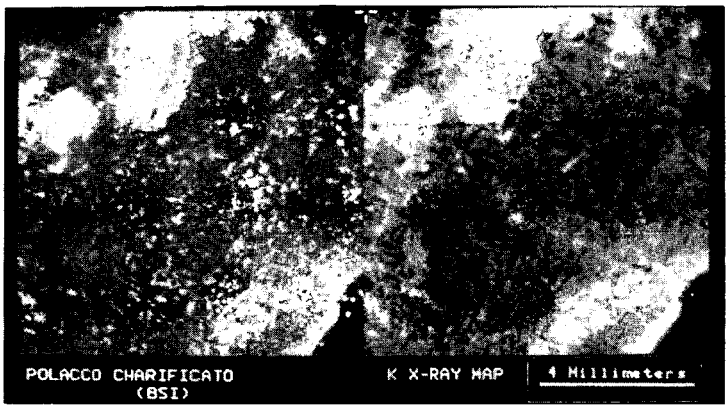

FIGURE 9. POTASSIUM DISTRIBUTION MAP OF DOPED POLISH CHAR

EFFECT OF THERMAL AND CHEMICAL PRETREATMENTS ON THE COPPER-CATALYZED GASIFICATION OF CARBON IN AIR

C.A. Leon y Leon and L.R. Radovic

Fuel Science Program, Department of Materials Science and Engineering
The Pennsylvania State University, University Park, PA 16802

Keywords: Copper Catalysts, Carbon Supports, Gasification Reactivity

INTRODUCTION

Copper is one of the most active catalysts for the gasification of carbon in oxygen [1]. Its high activity is thought to be related to the ease with which copper can undergo oxidation/reduction cycles at gasification conditions [2-6], thereby promoting the transfer of oxygen atoms to the (re)active carbon sites [2,7]. Evidently, oxygen transfer rates will be faster for smaller catalyst particles, which provide a higher degree of catalyst-carbon interface contact. (This explains the observed structure-sensitivity of the Cu- (and other metal-) catalyzed carbon gasification in air [8,9].) However, smaller particles are also more susceptible to catalyst-support interactions [10]. In this report we examine the role of carbon surface chemistry in (a) securing a high and thermally resistant Cu dispersion; and (b) affecting the kinetics of the Cu-catalyzed gasification process.

EXPERIMENTAL

For brevity this report will concentrate on the gasification of a highly pure, polymer-derived microporous carbon (Saran, Dow). Results on other (less porous or non-porous) carbons will be addressed at length elsewhere [11]. All carbons were subjected to a wide variety of thermal and/or chemical treatments aimed at modifying their surface properties (see Ref. 12). Changes in the surface chemistry and physics of the carbons were followed by techniques such as acid/base and mass titrations [12], electrophoresis [12,13], temperature-programmed desorption [14], N_2 and CO_2 adsorption [15], XPS [9], XRD [7,15] and others [11]. Selected samples were impregnated with copper acetate (Fisher) by incipient wetness or ion exchange (without filtering) to yield 5% Cu catalysts (dry carbon basis). In the latter case, the exchange on selected carbons was monitored by withdrawing small aliquots of supernatant after partial equilibration (ca. 30 min) and measuring the copper concentration remaining in solution with an ion-selective electrode (Orion). Gasification reactivities of all catalysts in 0.1 MPa air were measured on a modified TGA-7 apparatus (Perkin-Elmer) under conditions of chemical reaction control [9,14].

RESULTS AND DISCUSSION

Adding copper to Saran (and other) carbons was found to increase their maximum gasification rate in air by 2-3 orders of magnitude. (The method of Cu addition is important, since physically mixed Cu acetate was found to enhance the rate only by a factor of ca. 30.) It was also noted that both chemical and thermal treatments of the carbons alone affect their uncatalyzed reactivities, but only to well within the same order of magnitude [11]. Hence, the importance of chemical and thermal treatments lies in their effect on the distribution (dispersion) of the active catalyst phase throughout the carbon substrate [7]. In general, chemical treatments can be used to increase the dispersion of copper, and thermal treatments tend to decrease it. The contribution by these seemingly opposing effects to carbon gasification by Cu will be addressed below.

Copper Adsorption on Carbon. Anchoring metal precursors onto carbon by adsorption is thought to be neccessary in order to attain the highest possible metal dispersion [13]. Copper acetate dissociates in dilute aqueous solutions to yield mainly hydrated Cu^{+2} ions; these ions are stable below pH=6, and precipitate as hydroxide at high pH unless they are complexed by, e.g., NH_3, in which case they form a pH-dependent mixture of $[Cu(NH_3)_n(H_2O)_{6-n}]^{+2}$ ammine complexes ($1 \leq n \leq 5$) [16]. On the other hand, carbon surfaces can be pretreated to contain various kinds and amounts of surface functional groups [11-13] which differ in their chemical and thermal properties. For instance, low-temperature

oxidative treatments produce a mixture of strongly and weakly acidic oxygen complexes (discernible by neutralization with bases of increasing strength [11,14,15]) which decompose upon TPD according to their thermal strength to yield primarily CO_2 and CO (see Table 1) at relatively low and high temperatures, respectively. Increasing the pH of a carbon slurry leads to an increase in the number of dissociated, negatively charged functional groups, which can then act as anchors for metal cations [13]. Consequently, it was confirmed that the uptake of copper by carbon increases with increasing pH in the range $2.5 \leq pH \leq 11.5$ [11]. Figure 1 shows the adsorption isotherms of copper on selected pretreated carbons (see Table 1) at pH = 11.5. Relative to the untreated sample (CU), it is seen that the removal of oxygen functionalities by heat pretreatment (sample CH) lowers the copper adsorption capacity, while the introduction of functional groups by mild preoxidation (samples CA and CN) increases it.

The role of functional group dissociation in promoting metal ion sorption on carbon can be conveniently illustrated using electrophoretic mobility (EM) diagrams [13]. Figure 2 shows a typical EM diagram for a microporous, mildly oxidized carbon. It is shown that the pH of zero mobility, IEP (above which the net external surface charge of the carbon is negative), is over one pH unit lower than the point of zero net surface charge, PZC (determined by mass titration). This is taken as an indication that typical oxidative treatments or subsequent air exposure of microporous carbons leads to an inhomogeneous surface charge distribution, with the external (geometric) surface being enriched in negatively charged groups when IEP < PZC [13-15]. Hence, the observed increase in reactivity with increasing pH (Figure 2) can be attributed to an increase in the sorption of the Cu precursor leading to a higher catalyst dispersion. Figure 2 shows a maximum (and only three times higher) reactivity at pH = 8.5. Since the 5% Cu/C catalysts used to generate Figure 2 were made by ion exchange without filtering, the nonadsorbed copper probably forms larger, less active catalyst particles when the dried Cu/C samples are preheated to reaction conditions. However, the large surface area and the microporosity of these materials [12] preclude an extensive agglomeration and growth of copper particles [15], i.e., an extreme loss in reactivity. This is in agreement with XPS experiments, which indicate an external surface enrichment in Cu particles [9], particularly after heat treatment. The apparent maximum reactivity, also observed for samples prepared by incipient wetness using solutions of preadjusted pH [11], can arise from two factors. First, upon drying to remove the excess solvent, the concentration of ions (e.g., OH^-, Cu ammines) remaining occluded increases, thereby forcing further adsorption to take place in order to regain equilibrium. Since competition for sorption sites by NH_4^{+1} can be neglected, especially above pH = 9.25 [16], a maximum copper adsorption in the pH range 9-10 is to be expected [17]; above pH = 10 the contribution by hydroxides becomes measurable [16], and their precipitation facilitates Cu agglomeration upon heating. Second, the adsorption mechanisms of the predominant Cu species at different pH values may differ [18]. Attempts to desorb Cu from portions of dried (in vacuum at 313 K) batches ion exchanged at pH = 8.5, by washing with distilled water, failed. However, traces of copper could be desorbed from the samples prepared at pH = 11.5. In both cases, the strong adsorption suggests that some ligand exchange may have taken place. However, the exchange sites at both pH values differ; at pH = 11.5, more weakly acidic sites are activated for copper adsorption, but since the carbon surface becomes more negatively charged, the density of positive ions held electrostatically around these negative charges increases. (This effect is accompanied by the shrinkage of the diffuse portion of a hypothetical "double layer" surrounding the carbon surface [19].) The net result is the saturation of the carbon surface with positive charges which must repel each other and hence limit the access of the desired adsorbing cations to some negatively charged surface sites. Table 1 includes the estimated adsorption ratios of Cu to CO_2-evolving and to total acidic (NaOH-titratable) surface groups. The role of individual surface functional groups in promoting Cu dispersion and reactivity is addressed in detail in an accompanying paper [20].

Copper Dispersion on Carbon. The growth in average Cu crystallite diameter (measured by XRD) with heat pretreatment temperature is best illustrated in Figure 3. In all cases, heating the freshly prepared Cu/C catalysts in inert flowing gas (N_2) leads to Cu crystallite growth. Whereas the growth of Cu crystallites in samples CU and CH is comparable, that on sample CN is much less pronounced, despite the latter's lower surface area [12]. Since the main difference between samples CU and CH is the higher CO evolution yield of sample CU (Table 1), it follows that CO-evolving groups do not contribute directly to the adsorption or subsequent dispersion of Cu cations. (In contrast, $PtCl_6^{-2}$ [21] and $HMo_2O_7^{-1}$ [10] anion adsorption and subsequent metal dispersion were reported to be enhanced by the presence of CO-evolving groups.) On the other hand, CO_2-evolving groups appear to correlate better with copper adsorption. The amount of CO_2 evolved upon TPD is believed to be related to the

number of carboxyl-type ($-COO^{-1}$) groups present on a carbon surface, with one (plus one CO) or two CO_2 molecules being desorbed from two adjacent [21] or distant [21,22] carboxyl functionalities, respectively. Indeed, for the calcium carbon system (Ca^{+2})/CO_2 ratios of 0.5-1.25 have been taken as an indication that each cation adsorbs onto two negatively charged carboxyl groups [21]. In our case, Cu/CO_2 ratios of 0.32-0.87 (Table 1) could also be interpreted along these lines. However, since $NaHCO_3$ is believed to selectively neutralize the carboxyl groups on a 1:1 ratio [23], the poor agreement between Cu and $NaHCO_3$ uptakes (Table 1) suggests that in addition to carboxyl groups there are other (non CO-desorbable) surface groups which also participate in the copper adsorption process. Evidence in favour of the obvious choice, i.e., lactones [23], is presented in an accompanying report [20].

Gasification Reactivity of Cu/C Catalysts. Broadly speaking, the surface chemistry of carbons is related to their oxygen content [22], which can be adjusted by subjecting the carbons to selected chemical pretreatments [12]. Figure 4 shows the influence of the oxygen content of chemically pretreated Saran carbons on the gasification reactivity of the Cu/C catalysts (extrapolated when necessary to 623 K), after subjecting the catalysts to selected heat pretreatments. Following low temperature (623 K) heat pretreatments, a maximum reactivity is observed at intermediate oxygen contents. This is consistent with the observation that moderate (i.e., neither too mild nor too severe) oxidative pretreatments are most successful in producing homogeneously charged (IEP = PZC) carbon surfaces [12], because even though sample CA adsorbs less copper than, e.g., sample CN (Table 1), its adsorbed copper is more uniformly distributed (i.e., internally as well as externally) throughout each carbon particle. However, the resistance to Cu agglomeration over the surface of sample CA is inadequate and hence sample CA experiences a more severe loss of reactivity compared to all other samples (Figure 5). For all samples the normalized reactivity (at 623 K) is most severely affected by heat treatments in the range 623-923 K (Figure 5). TPD experiments indicate that the primary effect of heat pretreatments of the carbons alone in the temperature range 623-923 K is the desorption of CO_2-evolving (e.g., carboxyl and lactone) surface groups [12,22]. Hence the introduction (by chemical pretreatment) of CO_2-evolving groups prior to copper adsorption enhances not only the Cu dispersion but also the gasification reactivity of the carbon.

Figure 5 also shows that the removal of further (mainly CO-evolving) surface groups via heat pretreatments in the range 923-1223 K has less bearing on the magnitude of the loss of gasification reactivity. Nonetheless, Figure 4 suggests that the remaining (CO-evolving) groups do play a role in enhancing the magnitude of the reactivity. Since these groups are not likely to act as metal precursor adsorption sites, their role in securing a higher reactivity can be explained by recalling that the thermally stable groups remaining after each heat treatment can act as diffusion barriers to the agglomeration of Cu particles [24], in which case the higher reactivities of carbons with higher initial oxygen contents can be ascribed to their higher Cu dispersion after heat treatment.

The kinetics of the gasification process are also affected by both chemical and thermal pretreatments. Figure 6 shows that for all carbons thermal treatments of Cu/C catalysts increase the apparent activation energies (E_{ACT}) of the reaction. (An analogous behaviour is observed when using nonporous carbon black substrates [11].) The increase is more significant for the samples with the highest initial oxygen content. Samples with the lowest initial oxygen content yield E_{ACT} values approaching those of the high-temperature (1223 K) heat treated catalysts, thereby suggesting that the decrease in E_{ACT} values is related to the initial oxygen content of the carbons. Therefore, in addition to enhancing the dispersion of Cu by serving as diffusion barriers to its migration, thermally stable carbon-oxygen complexes can also be more difficult to gasify than reactive intermediates [25]. If so, oxygen-rich samples would readily yield highly dispersed catalyst particles upon thermal loss of the unstable Cu anchors, but their catalytic activity would be less temperature-sensitive than that of similar catalysts on oxygen-lean carbons, whose edges would be more susceptible to the exothermic formation of readily desorbable intermediates. This interpretation is consistent with (a) an apparent compensation effect observed for the catalysts heat treated to low temperatures [9,11], (b) the faster deactivation of (initially) oxygen-rich samples [11], and (c) a higher oxygen partial pressure dependence for the gasification of Cu/C samples with the least initial oxygen content [11].

CONCLUSIONS

Both chemical and thermal treatments play a crucial role in determining the gasification behaviour of Cu/C catalysts. Chemical pretreatments can be applied in order to enhance the concentration of CO_2-desorbable surface groups, which promote copper adsorption, catalyst dispersion, and Cu/C gasification reactivity. Thermal treatments lead to the agglomeration (and consequent reactivity loss) of the catalyst, particularly for carbons with low initial oxygen content. In both cases, the effects can be related to the influence of surface oxygen complexes on the reaction. Thermally unstable (moderately to strongly acidic, e.g., carboxyl and lactone) oxygen functional groups can favour gasification reactivity by acting as desorbable anchors for metal precursors. On the other hand, thermally stable groups appear to serve both as diffusion barriers to metal agglomeration (a desirable effect) and as stable reaction intermediates which are less readily gasified by the catalyst (an undesirable effect).

REFERENCES

1. D.W. McKee, in "Chemistry and Physics of Carbon" (Edited by P.L. Walker, Jr., and P.A. Thrower), Vol. 16, Marcel Dekker, New York (1981), p. 1.
2. D.W. McKee, *Carbon* **8**, 131 (1970).
3. J.W. Patrick and A. Walker, *Carbon* **12**, 507 (1974).
4. C. Moreno-Castilla, A. Lopez-Peinado, J. Rivera-Utrilla, I. Fernandez-Morales and F.J. Lopez-Garzon, *Fuel* **66**, 113 (1987).
5. A.J. Lopez-Peinado, J. Rivera-Utrilla, F.J. Lopez-Garzon, I. Fernandez-Morales and C. Moreno-Castilla, *Fuel* **65**, 1419 (1986).
6. T. Ganga Devi, M.P. Kannan and G.N. Richards, *Fuel* **69**, 1440 (1990).
7. L.R. Radovic, P.L. Walker, Jr. and Jenkins, *J. Catal.* **82**, 382 (1983).
8. C.A. Leon y Leon and L.R. Radovic, Proc. 20th Biennial Conf. on Carbon, Santa Barbara, CA (1991), p. 482.
9. C.A. Leon y Leon and L.R. Radovic, Proc. Int. Carbon Conf., Paris, France (1990), p. 44.
10. C.A. Leon y Leon and L.R. Radovic, Proc. 20th Biennial Conf. on Carbon, Santa Barbara, CA (1991), p. 84.
11. C.A. Leon y Leon and L.R. Radovic, in preparation.
12. C.A. Leon y Leon, J.M. Solar, V. Calemma, K. Osseo-Asare and L.R. Radovic, *Carbon*, Submitted (1991).
13. J.M. Solar, C.A. Leon y Leon, K. Osseo-Asare and L.R. Radovic, *Carbon* **28**, 369 (1990).
14. C.A. Leon y Leon, A.W. Scaroni and L.R. Radovic, *J. Colloid Interface Sci.*, Submitted (1991).
15. C.A. Leon y Leon and L.R. Radovic, Proc. 19th Biennial Conf. on Carbon, University Park, PA (1989), p. 42.
16. P. Duby, "The Thermodynamic Properties of Aqueous Inorganic Copper Systems," International Copper Research Association (1977).
17. N. Kovtyukhova and G. Karpenko, Proc. Int. Carbon Conf., Paris, France (1990), p. 680.
18. J. Wieber, F. Kulik, B.A. Pethica and P. Zuman, *Colloids Surfaces* **33**, 141 (1988).
19. J. O'M. Bockris and A.K.N. Reddy, "Modern Electrochemistry," Vol. 2, Plenum Press, New York (1977), Chapter 7.
20. C.A. Leon y Leon and L.R. Radovic, "Influence of Oxygen Functional Groups on the Performance of Carbon-Supported Catalysts," ACS Preprints, Div. Fuel Chem., New York (1991), in print.
21. A. Linares-Solano, C. Salinas-Martinez de Lecea and D. Cazorla-Amoros, *Energy & Fuels* **4**, 469 (1990).
22. B.R. Puri, in "Chemistry and Physics of Carbon" (Edited by P.L. Walker, Jr.), Vol. 6, Marcel Dekker, New York (1970), p. 191.
23. H.P. Boehm, E. Diehl, W. Heck and R. Sappok, *Angew. Chem. Internat. Edit.* **3**, 669 (1974).
24. P. Ehrburger, O.P. Majahan and P.L. Walker, Jr., *J. Catal.* **43**, 61 (1976).
25. L.R. Radovic, A.A. Lizzio and H. Jiang, in "Fundamental Issues in Control of Carbon Gasification Reactivity" (Edited by J. Lahaye and P. Ehrburger), Kluwer, The Netherlands (1991), p. 235.

Table 1. Features of Some Chemically Modified Saran Carbons Used as Cu Catalyst Supports.

Sample[a]	%O (wt.)	TPD [mmol/g][b] CO_2	CO	SN [mmol/g][b] $NaHCO_3$	NaOH	Cu ads.[c] [mmol/g]	Cu/CO_2 [mol/mol]	Cu/NaOH [mol/mol]
CH	0.8	0.09	0.30	0.01	0.09	0.03	0.36	0.37
CU	1.6	0.12	0.74	0.01	0.11	0.04	0.34	0.36
CP	5.6	0.91	1.69	0.35	2.07	---	---	---
CA	12.0	1.03	5.42	0.81	2.70	0.90	0.87	0.34
CN	20.8	4.11	4.78	0.58	2.03	1.26	0.32	0.62

[a] Pretreatments: CH, heat-treated in N_2 at 1223 K; CU, untreated; CP, oxidized in H_2O_2 at 373 K; CA, oxidized in air at 673 K (25% burnoff); CN, oxidized in HNO_3 at 363 K.

[b] TPD: Temperature Programmed Desorption; SN: Selective Neutralization (with bases).

[c] Amount of copper withdrawn from solution at pH=11.5 (adjusted using NH_4OH).

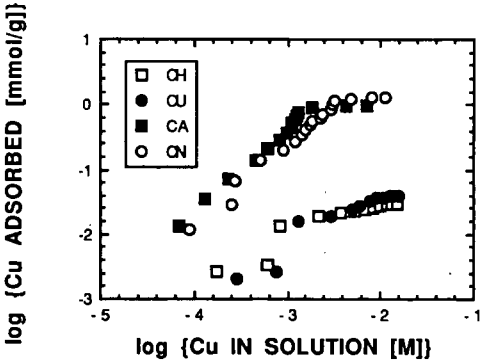

Figure 1. Influence of Chemical Pretreatment on the Adsorption of Copper by Saran Carbons (pH=11.5).

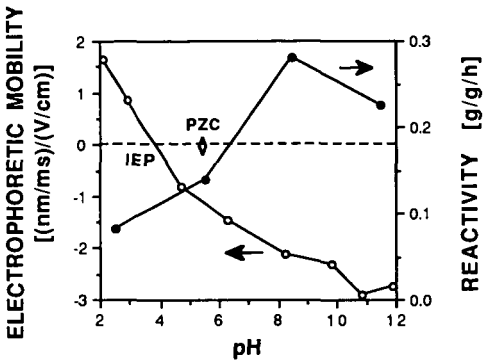

Figure 2. Relevance of Carbon Surface Charge to its Copper-Catalyzed Gasification Reactivity (at 573 K) in 0.1 MPa Air.

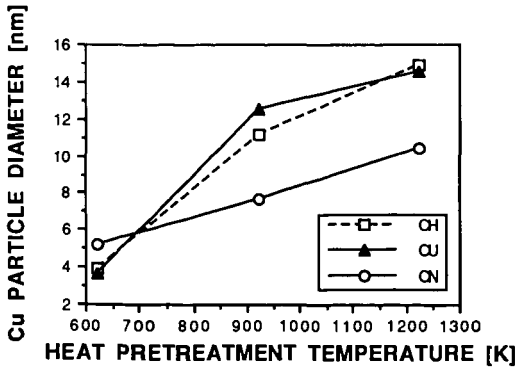

Figure 3. Variation in Average Cu Crystallite Diameter with Heat Pretreatment Temperature of Cu/Saran Catalysts.

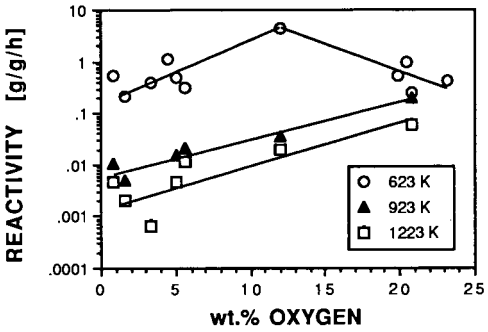

Figure 4. Effect of Carbon Surface Chemistry (% Initial Oxygen Content) on the Gasification Reactivity (at 623 K) of Cu/Saran Catalysts in 0.1 MPa Air, Following Heat Pretreatment at Different Temperatures (Indicated in the Figure).

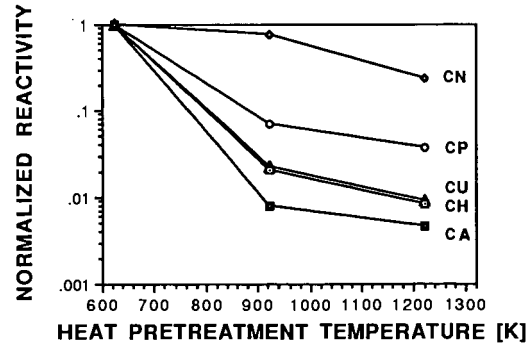

Figure 5. Normalized Loss in Gasification Reactivity (With Respect to Most Active Samples at 623 K) in 0.1 MPa Air for Cu/C Catalysts Differing in Chemical Pretreatment (see Table 1).

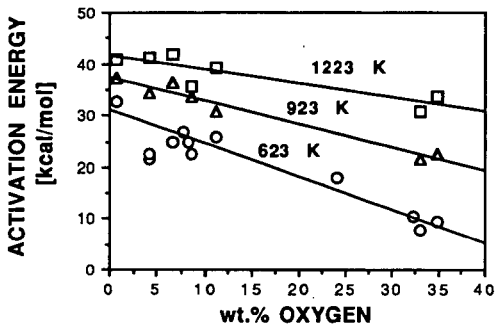

Figure 6. Effect of Carbon Surface Chemistry (% Initial Oxygen Content) on the Apparent Acivation Energy of the Gasification Reaction of Cu/Saran Catalysts in 0.1 MPa Air, Following Heat Pretreatment at Different Temperatures (Indicated in the Figure).

FURTHER EVIDENCE ON THE MECHANISM OF THE CO_2 CARBON GASIFICATION CATALYZED BY CALCIUM: TPD AFTER $^{13}CO_2$ CHEMISORPTION

Cazorla-Amorós, D., Linares-Solano, A., Salinas-Martínez de Lecea, C.
Departamento de Química Inorgánica e Ingeniería Química
Universidad de Alicante. Alicante, Spain.

Meijer, R. and Kapteijn, F.
Department of Chemical Engineering
University of Amsterdam. The Netherlands.

Keywords: Calcium catalyst, reaction mechanism

INTRODUCTION

Previous studies [1-7] have analyzed the use of the CO_2 chemisorption on the field of the carbon-gas reactions catalyzed by calcium. The results clearly show that this technique allows to understand its catalytic activity and to gain insight into the mechanism of the reaction. Important aspects of these studies are: 1) The chemisorption of CO_2 at 573 K (5-30 min) on carbons containing calcium is restricted to the surface of the CaO particles and therefore, can be used to determine the area (and dispersion) of the catalyst particles [1, 2, 3]. 2) Temperature programmed desorptions (TPD) of calcium-carbon samples after CO_2 chemisorption give information about the calcium-carbon contact, which is responsible for the catalytic activity [4, 5]. 3) Quantification of such contact provides the number of catalytic active sites (CAS) of the catalyst, which is used to normalize the CO_2 and steam reactivities of samples with different calcium loading or with different calcium sintering degrees, and to obtain kinetic parameters of interest with respect to the mechanism of the carbon-gas reaction catalyzed by calcium [6, 7].

Information about the mechanism of the reaction have been deduced from TPD of calcium-carbon samples previously contacted with CO_2 using the following reasonings: **i)** During the increase in temperature in a TPD run, a redistribution of the CO_2 is produced among the CaO particles. **ii)** The CO_2 diffuses from the external surface to the calcium-carbon contact yielding to the formation of $CaCO_3$-C species. **iii)** The decomposition of these species, which is produced at a higher temperature, takes place through the catalyst-carbon contact, by means of a two steps gasification mechanism [5,7]:

$$CaCO_3\text{-}C \rightarrow CaO\text{-}C(O) + CO \quad (1)$$
$$CaO\text{-}C(O) \longrightarrow CaO\text{-}C + CO \quad (2)$$

Accordingly to this mechanism, two types of CO should be evident; one coming from $CaCO_3$ and the other from the oxidized carbon atom. In other words, the reactive CO_2 molecule ($^*CO_2$) which proceeds from $CaCO_3$ through its contact with the carbon should give rise to two types of CO. Two types of CO have also been distinguished recently from TPD experiments in the case of potassium [8].

From the above mentioned studies -CO_2 chemisorption and TPD- it was not possible to distinguish these two types of CO because, under the experimental conditions used, they appeared very close. Changing the experimental conditions, as it has been done recently with TPD under vacuum [9], or using isotopically labelled molecules, as done in this paper and in a previous one [10], the two steps of the mechanism of the carbon gasification and the two different CO can be clearly distinguished.

The present paper deals with a series of TPD experiments performed in carbon samples with different calcium loadings and obtained after submitting these samples to a chemisorption process with $^{13}CO_2$ at different temperatures.

EXPERIMENTAL

Samples

The samples used have been extensively described elsewhere [1, 11]. In short, this study concerns with a high purity carbon, obtained from a phenol-phormaldehyde resin oxidized by HNO_3 to create oxygenated surface groups. Calcium is added by means of ionic-exchange or impregnation using a calcium acetate solution. The nomenclature of the samples is the following: A2 (corresponding to the oxidized carbon) followed by I or II, in order to distinguish between impregnation and ionic exchange, and by a number, indicating the amount of calcium loaded.

TPD after $^{13}CO_2$ interaction. Experimental procedure

The experimental procedure used to obtain the TPD spectra after interaction with $^{13}CO_2$ consists of the following steps: i) heating of the calcium-carbon sample in He up to 1223 K at 20 K/min heating rate; ii) cooling of the sample in He atmosphere to the treatment temperature (T_t) (i.e. 573 K or 773 K); iii) when the T_t is stabilized, He is switched to Ar; iv) Ar is switched to $^{13}CO_2$ and the contact with $^{13}CO_2$ is maintained for 1-1.5 minutes; v) TPD in He (20 K/min) up to 1223 K. The flow rates used were 30 ml/min (25°C, 1 atm).

All data are obtained by MS analysis and all signals are corrected for fragmentation and MS sensitivity.

RESULTS AND DISCUSSION

TPD after $^{13}CO_2$ interaction

Figure 1 presents the TPD spectra obtained after $^{13}CO_2$ chemisorption at 573 K on samples A2-II-2.9 and A2-I-1.3; Figure 2 shows the same experiment but after $^{13}CO_2$ treatment at 773 K on sample A2-I-1.3. In all the TPD runs, the evolution of ^{12}CO, ^{13}CO, $^{12}CO_2$ and $^{13}CO_2$ with temperature has been followed. The plot of the total CO and CO_2 evolution for the sample A2-II-2.9 (Figure 3) is similar to the TPD spectrum obtained from this sample after $^{12}CO_2$ chemisorption at 573 K [4], using a different coupled MS-reactor system, which shows the reproducibility of these experiments.

Figures 1 and 2 show that the TPD spectra consist on two $^{13}CO_2$ peaks and one $^{12}CO_2$ peak, together with a ^{13}CO peak and a ^{12}CO one. The baseline for the ^{12}CO does not recover the starting value and an increase in the ^{12}CO signal at temperatures higher than 1123 K is observed. This amount released at temperatures higher than 1123 K is independent of the calcium content, as can be deduced from the comparison of the TPD spectra of the samples A2-II-2.9 and A2-I-1.3 (Figure 1). In a previous publication [4] it was pointed out that the CO evolution profile observed at high temperatures corresponds to the decomposition of relatively stable oxygenated surface groups from the carbon itself, which may need temperatures higher than 1300 K for a total decomposition [12, 13]. This interpretation is confirmed by comparing Figures 1 and 2. In fact, the TPD spectrum of Figure 2 has been obtained after that of Figure 1b using the same sample, whereby, the sample has been submitted

to an additional heat treatment that produces a decrease in the number of surface C(O) complexes evolved at high temperatures.

In spite of the fact that the global TPD spectrum (Figure 3) is similar to the resulting after $^{12}CO_2$ treatment, it is obvious that the use of $^{13}CO_2$ allows us to obtain additional information about the calcium-carbon interaction. In this sense: i) three CO_2 peaks (two $^{13}CO_2$ and one $^{12}CO_2$) can be distinguished (Figures 1 and 2), whereas a two peak CO_2 profile is observed in Figure 3; ii) two CO peaks are differentiated (one ^{13}CO and one ^{12}CO). This last point constitutes the most relevant aspect of the results of these TPD experiments, because it is in agreement with the two steps mechanism previously proposed from the analysis of TPD runs. These TPD were obtained in He after contacting $^{12}CO_2$ [4] and from the same kind of experiments but performed under vacuum [9]. This mechanism consists of two steps (reactions (1) and (2)), the ^{13}CO proceeding from the decomposition of active $Ca^{13}CO_3$, that is to say, $Ca^{13}CO_3$ in the interface of contact with carbon (step (1) of the mechanism) and the ^{12}CO coming from the decomposition of the oxidized carbon sites (CaO-C(O)) of the CaO-carbon interface (step (2) of the mechanism). As this second process constitutes the determining step of the gasification mechanism, the ^{12}CO is released at higher temperatures than the ^{13}CO, as it is observed in Figures 1 and 2.

The interpretation of the different CO_2 peaks that appear in a TPD experiment, requires a more detailed analysis. It seems clear that the first $^{13}CO_2$ results from the surface or bulk calcium carbonate decomposition (inactive catalyst, which is not in contact with the carbon). This argument is in agreement with previous results [4, 5] in which was observed an increase in the amount of this first CO_2 with calcium loading. This assignment is also confirmed by the shift observed in the peak maximum to higher values with increasing the CO_2 treatment temperature (Figure 1b and 2). When T_t is higher than 573 K, the bulk calcium carbonate formation starts and hence, the CO_2 uptake increases. During a TPD experiment, this bulk $CaCO_3$ decomposes partially to the gaseous phase, increasing the CO_2 contribution of the first $^{13}CO_2$ peak, and shifting the peak temperature to higher values (Figures 1b and 2). It must be emphasized that this reasoning is in apparent contradiction with TPD experiments previously presented [4], obtained in a sample with a 3.7 Ca wt% (A2-I-3.7). In these experiments, the amount of CO_2 related to the first peak remains constant with T_t, while the total CO evolved increases with T_t, indicating that the bulk $CaCO_3$ decomposition is produced mainly through the interface. The discrepancy in the behaviour perhaps is due to the different initial dispersion of the samples studied (0.49 for the A2-I-1.3 and 0.60 for the A2-I-3.7). In any case, a more detailed study is necessary with labelled molecules to make clear this point.

In relation to the two CO_2 peaks ($^{13}CO_2$ and $^{12}CO_2$) that appear at temperatures close to the CO ones (^{13}CO and ^{12}CO respectively), the following possibility can be proposed to explain their origin:

The ^{13}CO, originated from the dissociation of the $Ca^{13}CO_3$ of the interface and the ^{12}CO, released during the decomposition of the oxidized carbon sites (CaO-C(O)), can react with oxidized carbon sites while leaving the porous network of the carbon and/or while leaving the CaO-carbon interface. Therefore, some $^{13}CO_2$ or $^{12}CO_2$ can be attributed to the following secondary reactions:

$$^{12}CO + CaO\text{-}C(O) \rightarrow CaO\text{-}C + {}^{12}CO_2 \qquad (3)$$
$$^{13}CO + CaO\text{-}C(O) \rightarrow CaO\text{-}C + {}^{13}CO_2 \qquad (4)$$

However, from the argument proposed we are unable to explain all of the experimental results. In fact: i) TPD experiments performed under high vacuum after CO_2 chemisorption at 573 K [9], show

only two CO_2 peaks whose maxima do not coincide with any of the two CO peaks observed in these experiments; this result indicates that there is some CO_2 that is not produced from secondary and/or parallel reactions. It must be pointed out that under high vacuum conditions, no secondary reactions of CO are observed. ii) The ratio CO/CO_2 calculated from TPD experiments of samples with different calcium sintering degree, decreases with increasing calcium sintering [4, 5]; in this case, should secondary reactions take place, this ratio should be constant. These two results indicate another possibility.

Some $^{13}CO_2$ of the second peak may also come from $Ca^{13}CO_3$ decomposition that is in contact with the carbon. This decomposition is produced without dissociation of the $^{13}CO_2$ molecule:

$$^{13}CaCO_3\text{-}C \rightharpoonup CaO\text{-}C + {}^{13}CO_2 \qquad (5)$$

Considering these arguments, it is possible to explain the origin of the different CO_2 peaks observed in the TPD experiments obtained after $^{13}CO_2$ treatment.

Mechanism of the reaction

From the above results it is possible to confirm the mechanism by which the CO_2 chemisorbed on the CaO reaches, during a TPD experiment, the catalyst-carbon contact and to strengthen the previously proposed mechanism for the carbon-gas reactions catalyzed by calcium [4,5].

$^{13}CO_2$ contact with the calcium-carbon samples.

a) T_t = 573 K

When the calcium-carbon sample, previously heat treated in He up to 1223 K, is contacted with $^{13}CO_2$ at T_t = 573 K, the CO_2 interaction is restricted to the CaO molecules on the surface of the particle [2,3]. At this temperature no dissociation of the $^{13}CO_2$ molecule is found as shown in Figure 4a, in which Ar flow is switched to $^{13}CO_2$ for 1.5 minutes and then to Ar. Of course when the CaO is highly dispersed, as it occurs in the sample A2-II-2.9 (in which the dispersion degree is 0.56), the catalyst should be as small particles (cluster) where the differentiation between surface and catalyst-carbon interface could not be justified. In any case, particle or cluster, the CO_2 interaction can be presented as:

$$CaO + {}^{13}CO_2 \rightharpoonup Ca^{13}CO_3 \quad \text{(surface of the particles)}$$
$$CaO\text{-}C + {}^{13}CO_2 \rightharpoonup Ca^{13}CO_3\text{-}C \quad \text{(interface of the cluster)}$$

b) 573 K < T_t < 823 K.

In this temperature range bulk carbonation occurs [3-5] and, as it is shown in Figure 4b, a small ^{13}CO peak from $Ca^{13}CO_3$ decomposition is found. Interestingly, the corresponding ^{12}CO from carbon gasification is not found, indicating the dissociation of the CaO-C(O) species does not takes place. Temperatures higher than 823 K are needed to produce the CaO-C(O) complexes evolution, as shown in the TPD experiments of Figures 1 and 2. This type of results are noteworthy because they also allow to distinguish the two types of CO above mentioned. If the dissociation of the $Ca^{13}CO_3$ takes place without evolution of ^{12}CO, it is clear that the $^{13}CO_2$ in this temperature range reaches the interface catalyst-carbon in agreement with previous findings [4,5]. The processes involved are:

$$CaO + {}^{13}CO_2 \rightleftharpoons Ca^{13}CO_3 \quad \text{(bulk and surface processes)}$$
$$CaO\text{-}C + {}^{13}CO_2 \rightleftharpoons Ca^{13}CO_3\text{-}C$$
$$Ca^{13}CO_3\text{-}C \rightleftharpoons CaO\text{-}C(O) + {}^{13}CO$$

c) T_t > 823 K.

At temperatures higher than 823 K the $^{13}CO_2$ reaches the interface and, because the temperature is high enough, in addition to its dissociation, there is also the gasification of carbon and hence the evolution of the oxygen carbon complexes (CaO-C(O)).

$$Ca^{13}CO_2\text{-}C \rightleftharpoons CaO\text{-}C(O) + {}^{13}CO$$
$$CaO\text{-}C(O) \longrightarrow CaO\text{-}C + CO$$

TPD after $^{13}CO_2$ chemisorption at 573 K.

a) During heating in He of a calcium-carbon sample which has been submitted to a chemisorption process in $^{13}CO_2$ at 573 K, the $^{13}CO_2$ previously chemisorbed on the surface of the CaO particle is being redistributed. The $^{13}CO_2$ reaches and occupies the calcium-carbon interface and part remains on the external surface.

b) As the heating proceeds, the $Ca^{13}CO_3$ on the surface of the particle (which is not in contact with the carbon), decomposes giving $^{13}CO_2$. Part of this $^{13}CO_2$ may interact with active carbon sites producing oxidized carbon atoms C(O) and ^{13}CO. It could be observed in Figures 1 and 2 that parallel to the appearance of the $^{13}CO_2$ there is also a shoulder in the ^{13}CO peak.

$$Ca^{13}CO_3 \text{ (surface)} \rightleftharpoons CaO \text{ (surface)} + {}^{13}CO_2$$
$${}^{13}CO_2 + C_f \rightleftharpoons {}^{13}CO + C(O)$$

c) At higher temperatures the active $CaCO_3$ in the catalyst-carbon contact, which could form an intermediate CaO-*CO_2-C, decomposes giving:

$$Ca^{13}CO_3\text{-}C \rightleftharpoons CaO\text{-}C(O) + {}^{13}CO$$

Most of the ^{13}CO peak of the Figures 1 and 2 comes from this reaction. Using TPD experiments in vacuum [9], it has been observed that this process is strongly affected by pressure (a shift of $\approx$ 100 K in the peak temperature is observed), indicating that this step is mainly in equilibrium. This fact is in agreement with the first step of the widely accepted mechanism of the carbon-gas reaction [14-16].

$$CO_2 + C_f \rightleftharpoons C(O) + CO$$

d) At higher temperatures (as shown in Figures 1 and 2) the decomposition of the oxidized carbon atoms in contact with the catalyst takes place, giving rise to the ^{12}CO peak.

$$CaO\text{-}{}^{12}C(O) \longrightarrow CaO\text{-}C + {}^{12}CO$$

e) Both the $^{13}CO_2$ and the $^{12}CO_2$ produced may also be ascribed to a secondary and/or parallel reactions between the large number of ^{13}CO released and oxidized carbon atoms.

$$^{13}CO_2 + CaO\text{-}C(O) \rightleftharpoons CaO\text{-}C + {}^{13}CO_2$$
$$^{12}CO_2 + CaO\text{-}C(O) \rightleftharpoons CaO\text{-}C + {}^{13}CO_2$$

f) Part of the $CaCO_3$ in contact with the carbon (maybe the perimeter of the contact zone) decomposes at slightly higher temperatures giving rise to part of the second $^{13}CO_2$ peak of Figures 1 and 2, which is superimposed with the $^{13}CO_2$ formed from the secondary and/or parallel reactions (point e). The CO_2 released as a consequence of this decomposition is clearly distinguished in the TPD experiments performed under vacuum [9].

CONCLUSIONS

TPD experiments performed in carbon samples with different calcium loadings which were previously contacted with $^{13}CO_2$ at 573 K and 773 K, have allowed to distinguish clearly two types of CO produced: ^{13}CO as a consequence of the dissociation of the CO_2 coming from active $CaCO_3$ decomposition at the catalyst-carbon contact- and ^{12}CO coming from carbon gasification -via decomposition of the oxidized carbon sites-. These two CO peaks of similar intensities confirm the following steps of the mechanism of the CO_2 gasification of carbon catalyzed by calcium:

$$Ca^{13}CO_3 \rightleftharpoons CaO\text{-}C(O) + {}^{13}CO$$
$$CaO\text{-}C(O) \longrightarrow CaO\text{-}C + {}^{12}CO$$

ACKNOWLEDGEMENTS

The authors thanks to the DIGCYT (project PB-88-0295), to the MEC for Diego Cazorla's Thesis grant and to the Department of Chemical Engineering of the University of Amsterdam.

REFERENCES

1. C. Salinas-Martínez de Lecea, M. Almela-Alarcón and A. Linares-Solano, Fuel, **69**, 21, (1990).
2. A. Linares-Solano, M. Almela-Alarcón and C. Salinas-Martínez de Lecea, J. Catal., **125**, 401, (1990).
3. D. Cazorla-Amorós, J.P. Joly, A. Linares-Solano, A. Marcilla-Gomis and C. Salinas-Martínez de Lecea, Accepted in J. Phys. Chem.
4. D. Cazorla-Amorós, A. Linares-Solano, C. Salinas-Martínez de Lecea and J.P. Joly, Carbon, **29**, 361, (1991).
5. A. Linares-Solano, C. Salinas-Martínez de Lecea, D. Cazorla-Amorós and J.P. Joly, Fundamental Issues in Control of Carbon Gasification Reactivity, (Eds. J. Lahaye and P. Ehrburger), NATO ASI Series E192, p. 409, Kluwer Academic Publishers, 1991.
6. D. Cazorla-Amorós, C. Salinas-Martínez de Lecea, A. Linares-Solano and A. Marcilla-Gomis, International Symposium on Carbon, New Processing and New Applications, Tsukuba, Tanso, Vol. 1, 4-8 Nov., p. 356, (1990).
7. D. Cazorla-Amorós, A. Linares-Solano, A.F. Marcilla-Gomis and C. Salinas-Martínez de Lecea, submitted to Energy & Fuels.
8. R. Meijer, M. Weeda, F. Kapteijn and J.A. Moulijn, Accepted in Carbon.
9. D. Cazorla-Amorós, A. Linares-Solano, C. Salinas-Martínez de Lecea, T. Kyotani, H. Yamashita and A. Tomita, in preparation.
10. F. Kaptéijn, R. Meijer, B. van Eck and J.A. Moulijn, Fundamental Issues in Control of Carbon Gasification Reactivity, (Eds. J. Lahaye and P. Ehrburger), NATO ASI Series E192, 221,

Kluwer Academic Publishers, 1991.
11. A. Linares-Solano, M. Almela-Alarcón, C. Salinas-Martínez de Lecea, Am. Chem. Soc. Division of Fuel Chemistry, **34(1)**, 136, (1989).
12. J. Wang, B. McEnaney, XIX Biennial Conference on carbon, Pennsylvania, U.S.A., p. 590, (1989).
13. B. McEnaney, Fundamental Issues in Control of Carbon Gasification Reactivity, (Eds. J. Lahaye and P. Ehrburger), NATO ASI Series E192, 175, Kluwer Academic Publishers, 1991.
14. F. Kapteijn and J.A. Moulijn, Carbon and Coal Gasification, (Eds. J.L. Figueiredo and J.A. Moulijn), NATO ASI Series E 105, 291, Martinus Nijhoff, 1986.
15. H. Freund, Fuel, **64**, 657, 1985.
16. H.J. Mühlen, K.H. van Heek and H. Jüntgen, Fuel, **64**, 994, (1985).

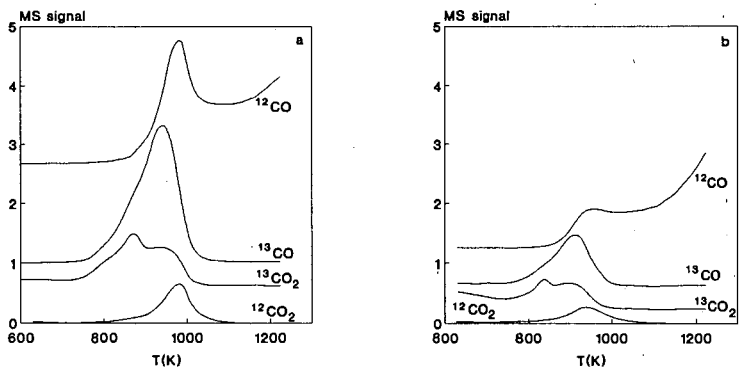

Figure 1. TPD-MS spectra obtained after $^{13}CO_2$ chemisorption at 573 K on samples: a) A2-II-2.9 and b) A2-I-1.3.

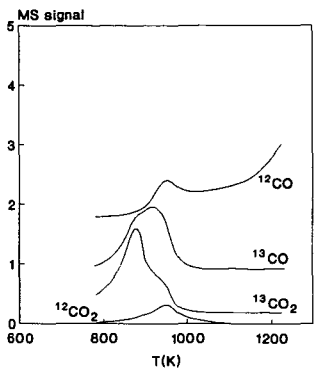

Figure 2. TPD-MS spectrum obtained after $^{13}CO_2$ treatment at 773 K on sample A2-I-1.3.

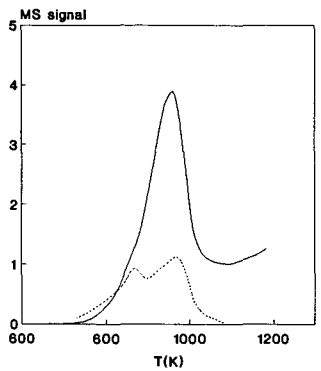

Figure 3. Total CO and CO_2 evolutions after $^{13}CO_2$ chemisorption at 573 K on sample A2-II-2.9 (—, CO; ---, CO_2).

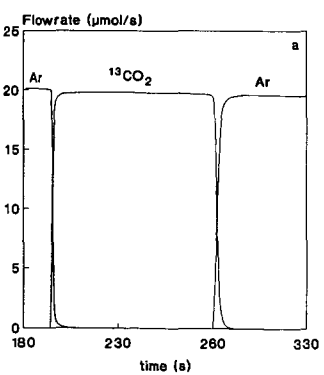

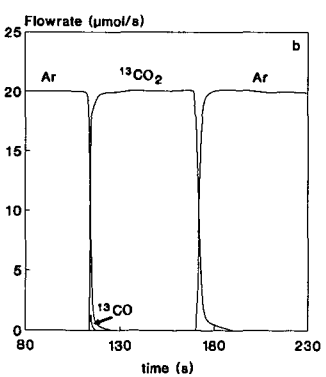

Figure 4. a) $^{13}CO_2$ chemisorption at 573 K on sample A2-II-2.9; b) $^{13}CO_2$ chemisorption at 773 K on sample A2-II-2.9.

CATALYSIS OF CHAR GASIFICATION IN O_2 BY CaO and $CaCO_3$

C.H. Bartholomew, R. Gopalakrishnan and M. Fullwood
BYU Catalysis Laboratory, Department of Chemical Engineering and
Advanced Combustion Engineering Research Center
Brigham Young University
Provo, UT 84602

Keywords: CaO catalysis; $CaCO_3$ catalysis; Coal char oxidation, catalysis of

ABSTRACT

Catalysis by CaO and $CaCO_3$ of the oxidation of a well-defined, high purity synthetic char, Spherocarb, was investigated at low reaction temperatures using thermal gravimetric analysis (TGA). Oxidation rates were likewise measured for fresh, demineralized, and Ca-impregnated samples of a high temperature char prepared in a flat-flame burner at about 1300 K from Beulah Zap coal. Spherocarb and demineralized Zap char were impregnated with Ca using aqueous impregnation and ion-exchange techniques. The resulting kinetic parameters for Spherocarb indicate significant catalytic effects--up to a 100 fold increase in reaction rate for $CaCO_3$ and 3,000 in the case of CaO. The oxidation rates of CaO-catalyzed Spherocarb and Beulah Zap char are the same within experimental error, suggesting that the high reactivity of the Zap char is due in large part to catalysis by CaO.

INTRODUCTION

Char oxidation is a complex heterogeneous process which often governs the overall rate of combustion. Oxidation rates are partially governed by surface properties of the char and reactions catalyzed by minerals within the char matrix. To date studies on catalytic effects of inorganic minerals on char oxidation have been relatively few, and many important questions regarding effects and mechanisms of mineral catalysis, and the relevance of laboratory temperature data to actual operating conditions remain unanswered.

The objectives of this ongoing study are to address some of these questions by (1) studying rates and mechanisms of CaO catalysis of the oxidation of synthetic chars and rank representative demineralized coal chars, (2) determining active sites, surface functional groups, and surface mineral phases in these chars, and (3) investigating effects of surface area and catalyst dispersion.

This paper reports TGA measurements showing the effects of CaO and $CaCO_3$ catalysis on low temperature oxidation rates of Spherocarb, a well-defined, high purity synthetic char and of a Beulah Zap char prepared in air at high temperature in a flat-flame burner.

EXPERIMENTAL

Oxidation rates of pure Spherocarb and CaO loaded Spherocarb prepared by aqueous impregnation (1.2% CaO) and ion exchange (2.8% CaO) with a solution containing an excess of calcium acetate [1] were measured using a thermogravimetric (TGA) system described elsewhere [2]. We designate the samples prepared by aqueous impregnation and ion exchange methods as 1.2% CaO(aq)/Spherocarb and 2.8% CaO(ion)/Spherocarb respectively. Spherocarb samples (Analabs, Inc.; particle diameter of 120 microns) were burned off to 50% of the initial weight at a temperature in the intrinsic rate regime of 748 K in 10% oxygen prior to preparation of the calcium-containing samples to facilitate the penetration of the Ca acetate or Ca hydroxide into the pores. Critical temperature data (temperatures for 6.5 % per minute burnoff) were initially obtained in 10% oxygen (in nitrogen) by heating 2 mg samples at 40 K/min to 1223 K. Thereafter, rates of oxidation were measured isothermally in 10%

oxygen to various stages of burnoff in the neighborhood of the critical temperature and in the region of 150-200 K below the critical temperature.

The dispersion of CaO particles on Spherocarb was measured following the procedure of Radovic et al. [3], and Solano et al. [4] using selective CO_2 chemisorption at 573 K in a TGA apparatus. Samples containing calcium were decomposed at 1173 K for 10 minutes in nitrogen flow, cooled to 573 K and after 10 minutes, exposed to flowing CO_2 in nitrogen for about 30 minutes. From the weight of CO_2 chemisorbed values of surface area (S_{CaO}), crystallite diameter (d), and percentage dispersion (D) of CaO were estimated using the equations of Radovic et al. [3].

Surface areas were determined from nitrogen adsorptions carried out at 77 K, using procedures and a flow adsorption system described previously [5]. Nitrogen adsorption isotherms were analyzed using the BET equation, and an area for the nitrogen molecule of 0.162 nm^2 was used to obtain surface areas.

High temperature Beulah-Zap (Zap) char was prepared by devolatilization in a flat flame burner of 200-230 mesh particles of the Argonne premium coal. The details of this apparatus have been described previously [6]. Feed gas consisted of 8.6% methane, 72% nitrogen, and 19.4% oxygen. The flame temperature at the collection probe was found to be 1251 K, and the residence time of the particles in the burner was 130 ms.

The Zap char was demineralized using concentrated acids (37 wt.% HCl and 49 wt.% HF). One gram of char was placed into a beaker and 200 ml of concentrated HCl was added. The beaker was heated to 333 K and stirred for two hours. Following HCl treatment, the char was washed 4 times using 1 liter of 365 K water for each wash. The HCl treatment was performed on the char 3 times, following which the same treatment was performed using HF. Following the final acid treatment the char was washed 8 times using 1 liter/wash of distilled water at 365 K and dried in a vacuum oven at 383 K overnight.

RESULTS AND DISCUSSION

Spherocarb . BET surface areas from nitrogen adsorption of untreated Spherocarb and 50% burned-off Spherocarb were determined to be 895±7 and 1039 m^2/g respectively; the value for the untreated Spherocarb compares favorably with values of 864 and 965 m^2/g reported by Waters et al. [7] and Dudek et al. [8]. In these two previous studies [7,8] surface area was observed to increase up to a conversion of 10-15% and then monotonically decrease with increasing conversion (reaching 650-660 m^2/g at 65-80% conversion); however conversion temperatures in these studies ranged from 780 to above 1300 K. In the present investigation conversion in the intrinsic rate regime at 748 K (10% oxygen) caused a 16% increase in surface area. This result suggests that densification/graphitization processes [9] are important at higher oxidation temperatures (above 750 K).

Arrhenius plots of oxidation rates for preburned (to 50%) and untreated Spherocarb are plotted in Fig. 1. The rates at any given temperature and activation energies (153 and 150 kJ/mol respectively) are the same within experimental error. Accordingly, the low temperature burnoff treatment at 748 K to open up pores for Ca impregnation does not affect the intrinsic reactivity of the Spherocarb char. The oxidation rate of Spherocarb at 667 K corrected to 21% oxygen (assuming an oxygen order of 0.6) is 2.8 μg/gs in very good agreement with a value of 2.3 μg/gs determined by Hurt et al. [10]. The activation energies from this study of 150-153 kJ/mole for oxidation of Spherocarb are in excellent agreement with the value of 153 kJ/mole determined for Spherocarb from the data of Hurt et al. [10] but somewhat lower than the value of 184 kJ/mol reported by Waters et al. [7] for Spherocarb and

very near values of 167-170 kJ/mole reported for oxidation of various synthetic mineral-free carbons [11,12]. Accordingly, the rate data and activation energies are valid for the intrinsic surface oxidation of carbon and are not influenced by pore diffusional or film mass transfer resistances.

Critical temperatures (6.5% wt. loss/min corrected for ash) for unloaded Spherocarb, 1.2% CaO(aq)/Spherocarb and 2.8% CaO(ion)/Spherocarb were found to be 968, 906 and 797 K respectively, indicating a large catalytic effect.

Rate data plotted in Arrhenius form are shown in Figure 2 for unloaded Spherocarb, 1.2% CaO(aq)/Spherocarb at 55 burnout and 2.8% CaO(ion)/Spherocarb at 50% burnout after pretreatment at 823 or 973 K. From the Arrhenius plots preexponential factors and activation energies were obtained for the unloaded Spherocarb and the two different catalytic loadings, one after pretreatment at two different temperatures (see Table 1). The activation energies for unloaded, 1.2% CaO(aq)/Spherocarb and 2.8% CaO(ion)/Spherocarb samples after pretreatment at 823 and 978 K are 150, 121, 96, and 139 kJ/mole respectively in the temperature range of 570-900 K, the magnitude of these values again indicating that the rates are probably not influenced by pore diffusional resistance in this range of conditions, since values of 125-200 are reported for mineral-catalyzed coal char combustion [13], although a value of only 64 kJ/mole was reported for Ca-impregnated char [14].

Table 1. Activation Energies and Pre-Exponential factors of oxidation of CaO-Loaded and Unloaded Synthetic and Zap Char Samples in 10% oxygen

Sample	Ea (kJ/mole)	Pre-Exponential (g/gsample s)
2.8% CaO(ion)/Spcb (823 K)	139	3.0×10^8
2.8% CaO(ion)/Spcb (973 K)	96	0.19×10^4
1.2% CaO(aq)/Spherocarb	121	3.6×10^4
Unloaded Spherocarb	150	99×10^4
Zap Char	112	1.4×10^6
1.86% CaO/Zap	117	6.9×10^6
Zap, demineralized	151	3.3×10^8

Rates calculated at 600 K from Figure 2 indicate that the 1.2% CaO(aq)/Spherocarb sample is more reactive than the unloaded sample by a factor of about 12 while 2.8% CaO(ion)/Spherocarb pretreated at 823 K is more reactive by a factor of about 100 (Table 2). This enhancement in rate is consistent with that of up to two orders of magnitude reported by Levendis et al. for CaO catalysis at low temperatures [14]; however, the 2.8% CaO(ion)-/Spherocarb pretreated at 973 K is 30 times more active than these other Ca-containing chars with a rate enhancement factor relative to the uncatalyzed sample of 2800. Apparently, the pretreatment temperature has a dramatic effect on activity. As will be shown later, the significantly higher activity after pretreatment at 973 K is due to the presence of CaO while $CaCO_3$ is present after pretreatment at the lower temperature. A smaller but still significant factor is the method of preparation; this is probably because the aqueous impregnation technique results in a dispersion that is inferior to that obtained by other techniques such as ion exchange [14].

TEM and SEM studies of unloaded and CaO loaded Spherocarb samples were also conducted to determine the distribution of CaO in the samples. The TEM results were inconclusive regarding the dispersion of CaO in the micro and mesopores of the carbon. However, the SEM pictures provided strong evidence that the aqueous impregnation deposits copious quantities of CaO on the exterior of the carbon spheres, while the ion exchange

technique provides a uniform dispersion and greater penetration of pores, especially into partially burned-out Spherocarb. Indeed, the extent of loading, dispersion, and surface area of CaO are greater for samples prepared by ion exchange than those prepared by an aqueous impregnation method (Table 3). Thus, smaller size crystallites of CaO are formed during the ion exchange process leading to better dispersion and higher surface area. Calcium loading by ion exchange probably allows calcium ions to enter into micro and mesopores of Spherocarb possibly accounting for its higher intrinsic reactivity (per surface area of CaO; see Table 2).

Table 2. Catalytic Effects of Ca in Oxidation of Spherocarb at 600 K

Sample	10^6 rate (g/gchar s)	10^4 rate (g/gCaO s)	10^6 rate (g/m^2CaO s)
2.8% CaO (ion -exch.) /Spherocarb (973 K)	237	85	
2.8% CaO (ion -exch.) /Spherocarb (823 K)	8.3	3.0	2.7
1.2% CaO (aq.-impr.) /Spherocarb	1.0	0.83	0.62
Ca-Free Spherocarb	0.085	-	-

Table 3. Effect of Method of Calcium Loading on CaO Dispersion

Sample	S_{CaO} (m^2/g CaO)	d (nm)	D (%)
1.2% CaO(aq)/Spherocarb	134	11.5	10.8
2.8% CaO(ion)/Spherocarb	180	8.5	14.5

The substantially higher reactivity of the 2.8% sample pretreated at higher temperature suggests the possible formation of a new catalytic phase. Indeed, TGA experiments of complete burning of 1.2% CaO(aq)/Spherocarb, 2.8% CaO(ion)/Spherocarb and pure calcium acetate performed in 10% O_2/90% N_2 atmosphere by ramping slowly from room temperature to 1173 K show that calcium acetate decomposes in two stages (Table 4). Comparison of weight changes observed from TGA experiments and values calculated assuming $CaCO_3$ and CaO as intermediate and final product respectively agree very well. This indicates that calcium in Spherocarb exists as $CaCO_3$ at temperatures below 823 K and CaO above this pretreatment temperature. Thus, CaO has substantially higher catalytic activity than $CaCO_3$.

Beulah Zap. BET surface areas from nitrogen adsorption of Zap char and demineralized Zap char were determined to be 322 and 348 m^2/g respectively. The value for the Zap char prepared with a residence time of 130 ms is somewhat higher than the value of 229 m^2/g reported by Hecker et al. [2] for a residence of time of 104 ms; however, this is expected since surface area of chars prepared in the flat flame burner increases very significantly with increasing residence time [2]. The larger surface area for the demineralized char is consistent with removal by acid treatment of mineral matter from micro or mesopores or pore entrances, since it is the micro and mesopores that account for most of the surface area of chars [5].

Table 4. Stoichiometry of Decomposition of Calcium Acetate by TGA

Experimental(TGA)			Calculated	
	Raw data (wt.%)	after water correction (wt.%)		(wt.%)
$Ca(Ac)_2$	100.000		$Ca(Ac)_2$	100.000
Water	5.400			
1st decomposition	60.167 (724 K)	63.601	$Ca(Ac)_2 \rightarrow CaCO_3$	63.331
2nd decomposition	33.658 (1048 K)	35.579	$Ca(Ac)_2 \rightarrow CaO$	35.476

*values in the parentheses are the temperatures of maximum decomposition rate

Arrhenius plots of rate data are shown in Fig. 3 for oxidation of Zap, 1.86% CaO/Zap (prepared by ion exchange), and demineralized Zap chars. It is evident that the reactivities of Zap and 1.86% CaO/Zap chars are very close while that of the demineralized Zap is much lower, suggesting that the high reactivity of Zap is due to the presence of Ca minerals. Activation energies for the three Zap chars are summarized in Table 1. The value of 112 kJ/mol for untreated Zap char is in excellent agreement with the value of 113 kJ/mol reported by Hecker et al. [2] for a Zap char prepared under very similar conditions in a flat-flame burner. The value of 151 kJ/mol for demineralized char is the same within experimental error as the value determined for pure Spherocarb (see Table 1), suggesting that oxidation of the demineralized char occurs by the same mechanism as the synthetic, mineral-free char.

Fig. 4 compares rate data in Arrhenius form for oxidation of catalyzed and uncatalyzed Spherocarb with those for Zap and demineralized Zap chars. The data for Zap and 2.8% CaO/Spherocarb fall nearly along the same line while rates for demineralized Zap are lower than for Zap but higher than those for uncatalyzed Spherocarb. Again, these results strongly suggest that the higher reactivity of Zap relative to demineralized Zap is due to the presence of CaO minerals in the Zap char. These results are quite consistent with data reported by Radovic et al. [15] for Zap, demineralized Zap, and CaO-catalyzed Zap pyrolysis chars prepared at a relatively high residence time (0.3 s) at 1275 K; in this latter study [15] the demineralization and CaO exchange were done on the coal. These workers likewise observed similar reactivities for Zap and CaO-catalyzed Zap chars, while that for the demineralized char was substantially lower. Apparently, significant differences in pretreatment of the coal and preparation of the chars do not affect the qualitative results, although quantitatively they are different.

CONCLUSIONS

1. The intrinsic reactivity of Spherocarb, a relatively mineral free synthetic char, is not affected by 50% oxidation at 748 K in 10% oxygen. In other words, there is no evidence of graphitization or densification under these conditions. However, there is a significant (16%) increase in BET surface area as a result of this mild oxidation treatment.

2. Kinetic parameters obtained in this study indicate a significant catalytic effect of CaO involving at least a 2800-fold increase in oxidation rate of Spherocarb compared to a 100-fold increase in rate for $CaCO_3$.

3. Ion exchange results in better dispersion and penetration of calcium into Spherocarb than other methods investigated in agreement with previous studies of synthetic chars.

4. The higher reactivity of Zap relative to demineralized Zap or uncatalyzed Spherocarb is due in large part to the presence of Ca minerals in the form of CaO.

ACKNOWLEDGEMENTS

This work was sponsored by the Advanced Combustion Engineering Research Center (ACERC). Funds for ACERC are provided by the National Science Foundation, the State of Utah, 26 industrial participants, and the U. S. Department of Energy. The authors gratefully acknowledge technical assistance by Professor W. C. Hecker, Mr. W. D. Hyde, Mr. W. E. White, Mr. K. M. McDonald, Mr. M. M. Painter, and Mr. R. F. Cope.

REFERENCES

1. Hengel, T. D., and Walker, P. L., Jr, *Fuel*, 63 (1984) 1214.

2. Hecker, W. C., McDonald, K. M., Jackson, C. D., and Cope, R. F., paper presented at the First International Conference on Combustion Technologies for a Clean Environment, Vilamoura, Portugal, Sept., 3-6, 1991.

3. Radovic, L.R., Walker, P.L.Jr, and Jenkins, R.G., *J. Catal.*, 82 (1983) 382.

4. Linares-Solano, A., Almela-Alarcon, M., and Salinas-Martinez de Lecea, C., *J. Catal.*, 125 (1990) 401.

5. White, W. E., Bartholomew, C. H., Hecker, W. C., and Smith, D. M., *Adsorption Sci. & Techn.*, in press.

6. Hyde, W. D., *Effect of Preparation Reactor and Parent Coal Rank on Coal Char Reactivity*, M. S. Thesis, Brigham Young University, 1990.

7. Waters, B. J., Squires, R. G., and Laurendeau, N. M., *Comb. Sci. & Tech.*, 62 (1988) 187.

8. Dudek, D. R., Longwell, J. P., and Sarofim, A. F., *Energy & Fuels*, 3 (1989) 24-28.

9. Hurt, R. H., Dudek, D. R. Longwell, J. P., and Sarofim, A. F., *Carbon*, 26 (1988) 433-449.

10. Hurt, R. H., Sarofim, A. F., and Longwell, J. P., "The Role of Microporous Surface Area in Gasification of Uncatalyzed Carbon," submitted, 1991.

11. Felder, W., Madronich, S., and Olson, D. B., *Energy & Fuels*, 2 (1988) 743-750.

12. Levendis, Y. A. Flagan, R. C., and Gavalas, G. R., *Combust. & Flame*, 76 (1989) 221-241.

13. Suuberg, E. M., Wojtowicz, M., and Calo, J. M., 22nd Internat. Symp. on Combustion.

14. Levendis, Y. A., Nam, S. W., Lowenberg, M., Flagan, R. C., and Gavalas, G. R., *Energy and Fuels*, 3 (1989) 28.

15. Radovic, L. R., Walker, P. L., Jr., and Jenkins, R. G., *Fuel*, 62 (1983) 209.

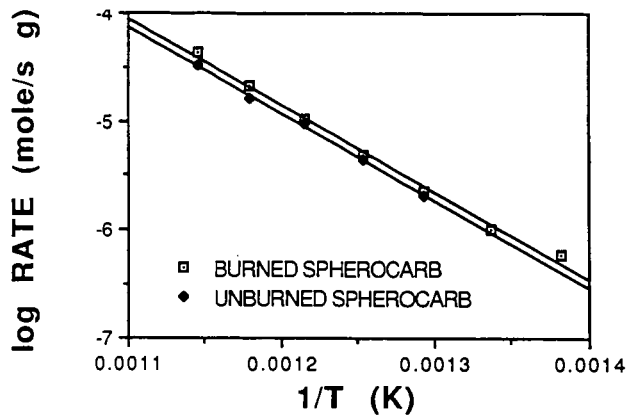

Figure 1. Arrhenius plots of oxidation rates of Spherocarb and partially oxidized Spherocarb (50% conversion at 748 K in 10% oxygen in nitrogen).

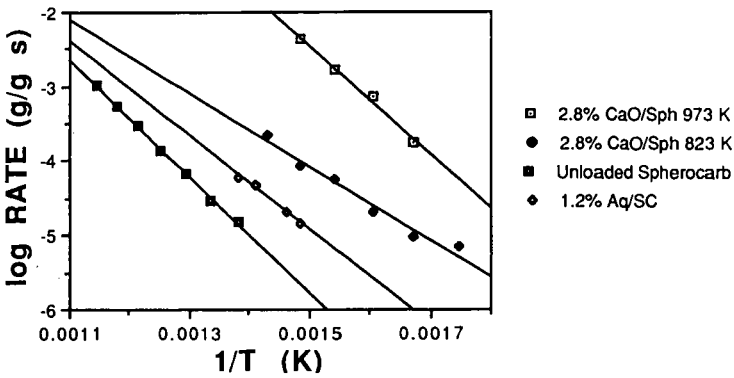

Figure 2. Arrhenius plots of oxidation rates for 2.8% CaO(ion)/Spherocarb (pretreated at 823and 973 K), 1.2% CaO(aq)/Spherocarb, and uncatalyzed Spherocarb in 10% oxygen.

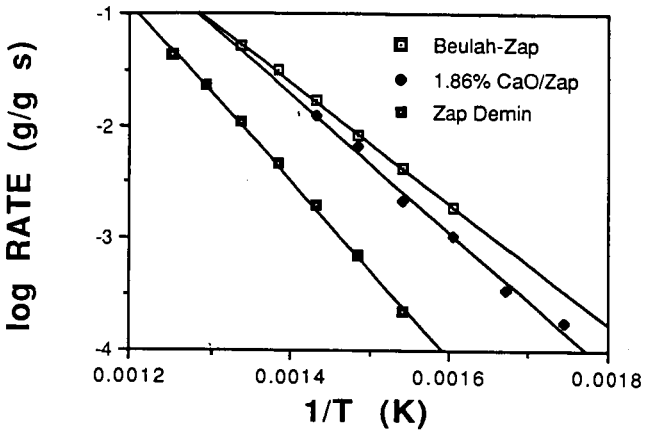

Figure 3. Arrhenius plots of oxidation rates for Zap, 1.86% CaO/Zap (prepared by ion exchange), and demineralized Zap chars in 10% oxygen.

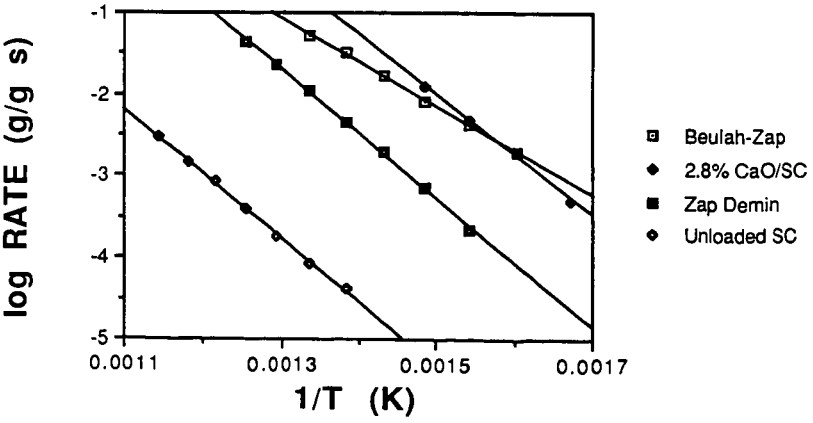

Figure 4. Arrhenius plots of oxidation rates for catalyzed and uncatalyzed Spherocarb and for Zap and demineralized Zap chars in 10% oxygen.

Potassium-Catalysed Carbon Gasification in CO_2 studied by Transient Techniques.

F. Kapteijn, R. Meijer, S.C. van Eck and J.A. Moulijn*
Department of Chemical Engineering, University of Amsterdam
Nieuwe Achtergracht 166, 1018 WV, Amsterdam, The Netherlands
* *present address: Department of Chemical Technology, University of Delft*

Keywords: transient kinetics, labelled CO_2, potassium-catalysed gasification

ABSTRACT

The K_2CO_3/carbon system has been studied under gasification conditions applying transient techniques, *i.e.* temperature programmed desorption and step-response experiments, in combination with labelled CO_2 ($^{13}CO_2$ and $C^{18}O_2$). Detailed information on the mode of catalytic action of potassium, the composition of the catalytically active alkali species and the rate of the different processes, is obtained.

Step-response experiments reveal that the potassium/carbon system is very dynamic. Upon a gas phase step change from a reactive to an inert gas phase at 1000 K the effluent gas composition is strongly affected by secondary reactions of desorbed species with the alkali catalyst on the carbon surface. The composition of the catalytically active alkali species changes with increasing gasification temperature. At 1000 K it can be represented by a cluster composed of several potassium phenolate species and contains chemisorbed CO_2 and reactive oxygen, whereas at 1200 K merely highly reactive potassium phenolate species are present. From step-response and temperature programmed desorption experiments it can be concluded that during gasification in CO_2, gas phase CO is inserted into the carbon matrix.

A model proposed for the mechanism of the potassium-catalysed gasification of carbon in CO_2 can adequately describe the observed transient and steady state behaviour taking into account that during steady state gasification in CO_2 carbon-oxygen intermediates of different stability are present which, depending on temperature, simultaneously desorb on exposure to an inert.

INTRODUCTION

Potassium-catalysed gasification is usually kinetically described by a two step model, in which the oxidation/reduction cycle (eq. 1) represents all (faster) steps preceeding gasification (eq. 2) [1].

$$CO_2 + C_f \underset{k_{-1}}{\overset{k_1}{\rightleftharpoons}} CO + C(O) \qquad (1)$$

$$C(O) \xrightarrow{k_2} CO \qquad (2)$$

Kinetic studies [1-3] have shown that addition of alkali catalysts increases the steady state concentration of carbon-oxygen intermediates and does hardly affect the equilibrium ($K_1=k_1/k_{-1}$) and intrinsic rate constant (k_2).

By applying labelled molecules [4-6] it was concluded that oxygen exchange between H_2O,H_2 and CO_2,CO is catalysed by the alkali catalyst and occurs without involvement of carbon-oxygen intermediates. The catalytically active site is envisaged as an alkali cluster M_xO_y (*), anchored to the carbon surface via plenolate groups. This cluster can contain chemisorbed CO_2 (CO_2-*), up to CO_2/M_a = 0.3 [3,4,7-9], which is present at gasification temperatures. This CO_2 is easily exchanged with gas phase CO_2 through eq. 4 [10].

A model for the potassium-catalysed gasification of carbon in CO_2 can be represented by eqs. (1,2,4-7), in which *, O-* and CO_2-* represent the different states of the catalytically active alkali cluster, and C_f and C(O) the carbon sites active for gasification.

$$^{\circ}CO_2 + CO_2\text{-}* \rightleftharpoons {}^{\circ}CO_2\text{-}* + CO_2 \qquad (4)$$

$$CO_2 + * \rightleftharpoons CO_2\text{-}* \quad (5)$$

$$CO_2\text{-}* \rightleftharpoons CO + O\text{-}* \quad (6)$$

$$O\text{-}* + C_f \rightleftharpoons * + C(O) \quad (7)$$

Temperature programmed desorption (TPD) and step-response experiments (SRE) in principle provide information on the reaction, intermediates and rates of elementary processes, especially when labelled molecules are applied [4,11-13]. Application of $^{13}CO_2$ enables us to distinguish between CO originating from gas phase reactant (^{13}CO) and CO from the carbon (CO), $C^{18}O_2$ to trace the behaviour of the oxygen in the system under study.
In this paper the results are presented of applying ^{13}C and ^{18}O labelled CO_2 in TPD and SRE experiments, that were designed to obtain detailed mechanistic information on the reactions taking place during catalysed CO_2 gasification and the role of the catalyst.

EXPERIMENTAL

Throughout this paper all labelled species are addressed with a prefix, *viz.* ^{18}O and ^{13}C, whereas in all cases C and O without prefix refer to ^{12}C and ^{16}O. Experimental details can be found elsewhere [14].
All gases used are of HP or UHP grade and are purified (O_2 and/or H_2O removal) before being fed to the gas mixing sections. $^{13}CO_2$ and $C^{18}O_2$ (MSD isotopes; 99.3 % ^{13}C and 90-91 % ^{18}O pure, respectively) were used as received. The ^{16}O in the $C^{18}O_2$ feed is present as $CO^{18}O$ (≈ 20% of the total CO_2).
The catalysed gasification in CO_2 was studied with 50-200 mg samples of K_2CO_3/Norit RX extra (K/C_i = 0.019). The alkali-metal content of fresh and used samples was determined by ICP-AES.
In step-response experiments (SRE) CO_2/Ar mixtures that flow through the sample at gasification temperatures are exchanged with an Ar flow and *vice versa* and the response of the sample on this change is followed continuously by a PC controlled MS. The raw MS data are corrected for background levels, fragmentation contributions (CO_2 to CO) and MS sensitivity for the different molecules, and converted into molar flowrates of the gaseous species leaving the reactor.
For the TPD experiments the samples were pretreated by TPD of the fresh sample (reduction) and exposed to a reactive gas mixture at different temperatures. The TPD patterns were obtained in a helium flow of 20 $\mu mol.s^{-1}$ at a heating rate of 10 $K.min^{-1}$ up to 1200 K, followed by an isothermal period of 30 minutes at 1200 K. The desorption rates of CO and CO_2 are expressed as (mol desorbed).(mol K actually present)$^{-1}.s^{-1}$. Simultaneously GC analysis was performed to quantify the (labelled) CO and CO_2 production rates monitored by the MS.

RESULTS AND DISCUSSION

Upon introduction of Ar after $^{13}CO_2$ exposure at 1000 K (figure 1A) a fast declining $^{13}CO_2$, CO_2 and ^{13}CO production, reaching the baseline within 50 seconds, and a tailing CO production, lasting up to 5 minutes, is observed. The composition of the product gas in the initial period is strongly influenced by fast CO_2 and oxygen exchange reactions, by which part of the primary desorption products ($^{13}CO_2$ and CO) are converted into CO_2 or ^{13}CO. Figure 1B shows after correction for oxygen exchange reactions the primary desorption rates of CO (amu 28+44), ^{13}CO (amu 29-44) and $^{13}CO_2$ (amu 45+44). Amounts are given in table 1.

Upon reintroduction of $^{13}CO_2$ (figure 1C) chemisorption and sample oxidation is observed. Sample oxidation can be deduced from the data in figure 1C by considering that under steady state conditions CO and ^{13}CO are produced in a 1:1 ratio (corrected for oxygen exchange with $^{13}CO_2$). Chemisorption amounts can be calculated by comparing the total carbon in the product gas molecules with that of a blanc run with an inert SiC sample (figure 1D). After approximately 50 seconds steady state gasification and oxygen exchange conditions are reached. Variation of the time span in argon at 1000 K before exposure to $^{13}CO_2$,Ar did not have any significant influence on these results.

In figure 2 the response curves for a gas phase step change from 10% $^{13}CO_2$,Ar to Ar and *vice versa* at respectively 1100 and 1200 K are shown, with an analogous data treatment.
At 1200 K all $^{13}CO_2$ is converted, resulting in equal CO and ^{13}CO production rates, whereas at 1100 K also $^{13}CO_2$ and CO_2 are present under steady state conditions. Upon a gas phase step

change to Ar no $^{13}CO_2$ or CO_2 is produced at both temperatures. However, it is striking that together with CO and in the absence of $^{13}CO_2$ a considerable amount of ^{13}CO desorption is observed. Reintroduction of $^{13}CO_2$ at 1100 K shows both a CO overshoot due to gasification and a ^{13}CO overshoot due to oxidation. At 1200 K steady state gasification conditions are directly restored without any overshoot and no $^{13}CO_2$ or CO_2 is detected in the product gas. All $^{13}CO_2$ is converted. However, a mass balance calculation shows that upon reintroduction of $^{13}CO_2$ at 1200 K a certain amount of ^{13}C is not accounted for in the product gas, suggesting an incorporation in the sample.
Similarly to the uncatalysed gasification [15] the CO release can only be well described by two parallel desorption processes. Therefore it is proposed that, apart from the catalytic clusters, two types of carbon–oxygen complexes are present, in semiquinone structures and in carbonylic structures. The former can be converted in to the more reactive latter species on armchair edges of the carbon [15]. A schematic picture is given below. Left are indicated reaction on the zig–zag edge and right on the armchair edge.

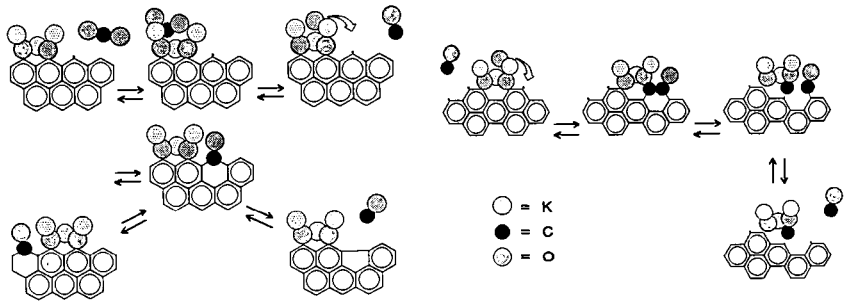

The main desorption products in a TPD after exposure to 10% $^{13}CO_2$,Ar at 673 to 1000 K are $^{13}CO_2$, released between 500 to 900 K, followed by CO above 900 K (figure 3). Additionally, between 700 and 1000 K, smaller amounts of CO_2 and ^{13}CO are observed. After exposure at 1000 K also a small amount of ^{13}CO above 1000 K is observed (figure 3C). This amount increases if the sample has been exposed to a higher partial pressure of $^{13}CO_2$.
Apparently the reduced sample is only partially reoxidised by CO_2 at 673 K, and increasingly more at higher temperatures. Therefore, the CO_2 desorption amounts decrease with exposure temperature, whereas the CO release increases. The latter is ascribed to the reduction of the potassium oxide in the cluster by the carbon or the decomposition of the phenolate groups. The small CO evolution around 950–1000 K is ascribed to decomposition of chemisorbed CO_2 into CO and O*. This is the unlabelled CO_2 since the $^{13}CO_2$ had already been replaced by fast exchange.
During TPD oxygen exchange takes place when $^{13}CO_2$ and CO are both present (around 900 K). TPD confirms the SRE experiments that some ^{13}CO is inserted in the sample, probably in the carbon, analogously to the uncatalysed case.

A TPD pattern obtained after $C^{18}O_2$ exposure at 673 K (figure 4A) shows $C^{18}O_2$ and $CO^{18}O$ desorption below 1000 K and a CO and $C^{18}O$ release spread over a wide temperature range. After $C^{18}O_2$ exposure at 1000 K (figure 4B) the CO and $C^{18}O$ desorbed is much larger and mainly takes place above 1000 K, in agreement with fig. 3. After gasification in $C^{18}O_2$ and subsequently in CO_2, the TPD pattern (figure 4C) shows low temperature CO_2 desorption and CO has become the main desorption product above 1000 K, whereas still a small amount of $C^{18}O$ desorption is observed. Compared to fig. 3C it is obvious that chemisorbed $C^{18}O_2$ must have been exchangedrapidly with CO_2, but that part of the ^{18}O in the sample is hard to exchange (fig. 4B and C).
SRE experiments with CO_2 and $C^{18}O_2$ indicate that the oxygen in the potassium cluster can be exchanged (1000 K) within 5 minutes ($^{18}O/K = 1$) by direct exchange of CO_2 with chemisorbed $C^{18}O_2$ and exchange of oxygen in the cluster with chemisorbed CO_2, yielding $C^{18}OO$.

Also in figures 4 the shoulder in the CO release, around 950–1000 K can be ascribed to decomposition of strongly chemisorbed CO_2.

In summary the step–response and temperature programmed desorption experiments, using labelled CO_2, have revealed the following principal phenomena. The active potassium oxide cluster still contains chemisorbed CO_2 at 1000 K, not above 1100 K. This chemisorbed CO_2 is easily exchanged with gas phase CO_2, and can exchange oxygen present in the cluster. It can decompose upon formation of CO and reactive oxygen in the cluster. The amount of oxygen in the cluster decreases with increasing temperature. This oxygen reacts with the carbon where it forms surface complexes, that can decompose to CO, which represents the gasification step. Two surface complexes are distinguished that decompose at different rates. The CO desorption is reversible and accounts for the incorporation of CO in the sample. All these phenomena will contribute to the gasification rate.

ACKNOWLEDGEMENT

These investigations have been executed within the framework of the Dutch National Coal Research Programme (NOK), which is managed by the Project Office for Energy Research (NOVEM) and financed by the Ministry of Economic Affairs.
The financial support of SON–NWO for purchasing the labelled CO_2 is gratefully acknowledged.

REFERENCES

1. Kapteijn F., Peer O. and Moulijn J.A., *Fuel*, 65, 1371 (1986).
2. Kelemen S.R. and Freund H., *J. Catal.*, 102, 80 (1986).
3. Koenig P.C., Squires R.G., and Laurendeau N.M., *J. Catal.*, 100, 228 (1986).
4. Cerfontain M.B., Meijer R., Kapteijn F., and Moulijn J.A., *J. Catal.*, 107, 173 (1987).
5. Saber M.S., Falconer J.L. and Brown L.F., *J. Catal.*, 90, 65 (1984).
6. Mims C.A. and Pabst J.K., *ACS Div. Fuel Chem. Prep.*, 25, 258 and 263 (1980).
7. Ratcliffe C.T., *ACS Div of Fuel Chem. Prepr.*, 30, 330 (1985).
8. Mims C.A., and Pabst J.K., *J. Catal.*, 107, 209 (1987).
9. Meijer R., Sibeijn M., van Dillen M.R.B., Kapteijn F. and Moulijn J.A., *I & E C Research* in press.
10. Cerfontain M.B., *Ph.D. Thesis Univ. of Amsterdam*, The Netherlands (1986).
11. Kapteijn F., and Moulijn J.A., in *Carbon and Coal Gasification: Science and Technology*, eds. J.L. Figueiredo and J.A. Moulijn, Nijhoff Publ., Dordrecht, 291 (1986).
12. Cerfontain M.B., Kapteijn F. and Moulijn J.A., *Carbon*, 26, 1, 41 (1988).
13. Cerfontain M.B., Agalianos D. and Moulijn J.A., *Carbon*, 25, 351 (1987).
14. Meijer R.,*Ph. D. Thesis, Univ. of Amsterdam*, The Netherlands, 1991.
15. F. Kapteijn, R. Meijer and J.A. Moulijn, ACS meeting New York, aug. 1991.

Table 1. Desorption products (μmol) after a gas phase step change from 10% $^{13}CO_2$,Ar to Ar at different temperatures. F_t = 20 μmol.s^{-1}, K_a = 115 μmol

	CO	^{13}CO	CO_2	$^{13}CO_2$
T = 1000 K	9.8	4.8	2.8	8.0
T = 1100 K	6.5	2.3	-	-
T = 1200 K	19	8.5	-	-

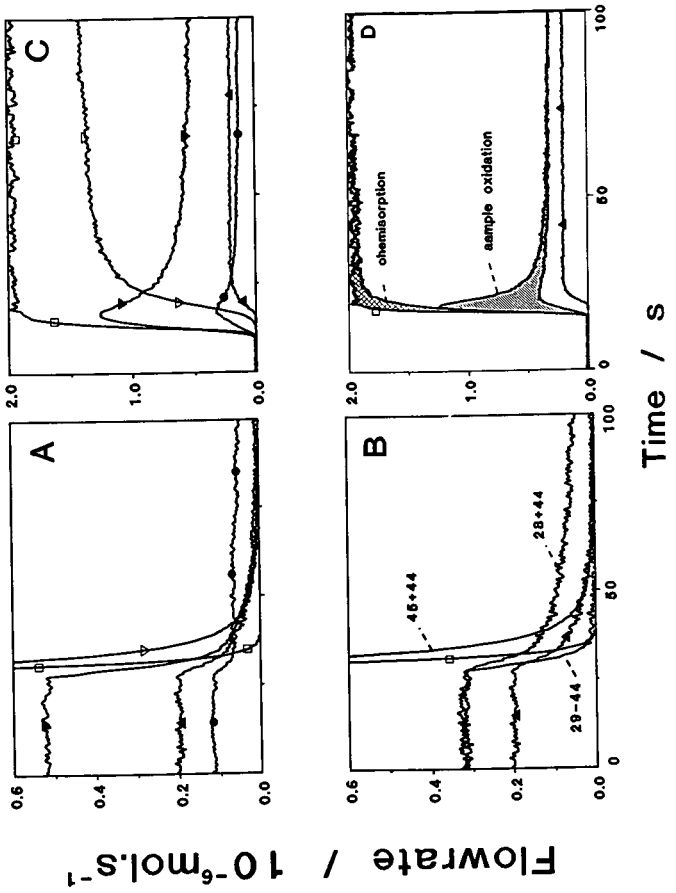

Figure 1 : Response curves for a gas phase step change from 10% $^{13}CO_2$,Ar to Ar (A,B) and *vice versa* (C,D) at 1000 K.
(A and C represent the measured signals, B and D the converted data (see data handling).

Key: CO; ^{13}CO; $C^{18}O$; CO_2; $^{13}CO_2$; $CO^{18}O$; $C^{18}O_2$, blanc run.

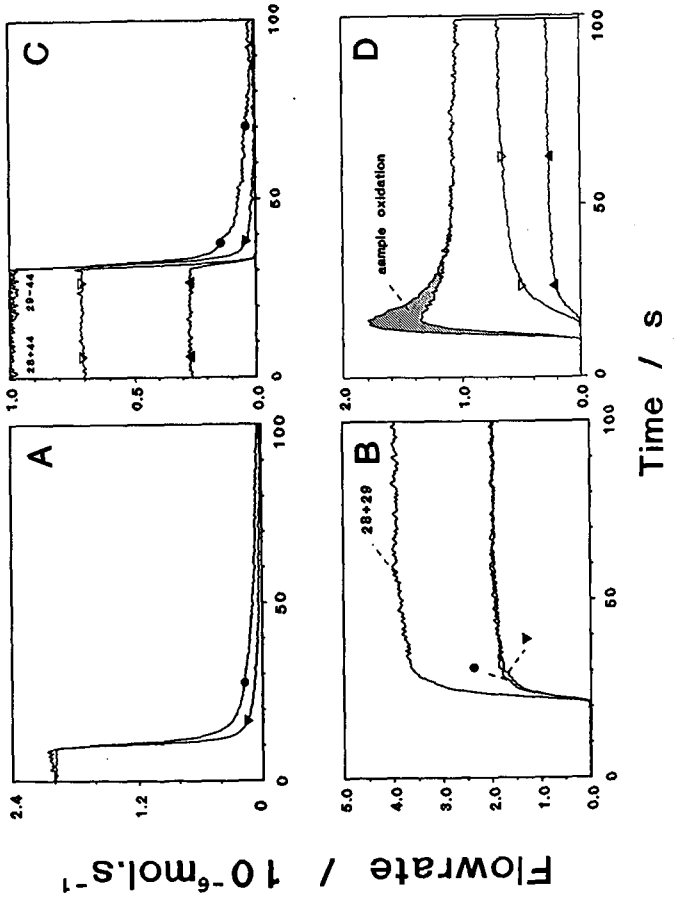

Figure 2 : Response curves for a gas phase step change from 10% $^{13}CO_2$,Ar to Ar (A,C) and *vice versa* (B,D) at different temperatures (key as in figure 1).
A,B. T = 1200 K; C,D T = 1100 K.

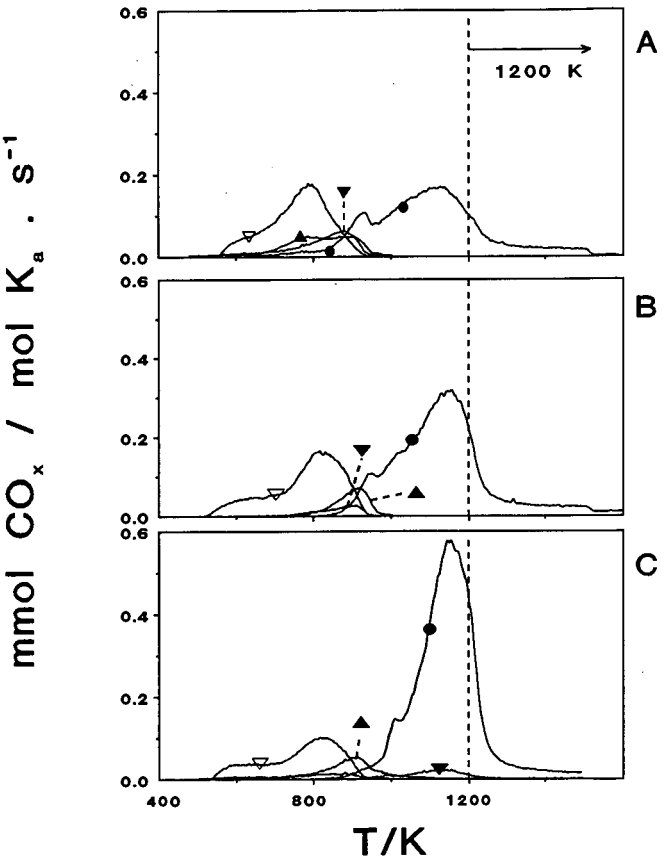

Figure 3 : TPD patterns obtained after exposure in 10% $^{13}CO_2$,Ar at: A. 673 K; B. 873 K; C. 1000 K (key as in figure 1)

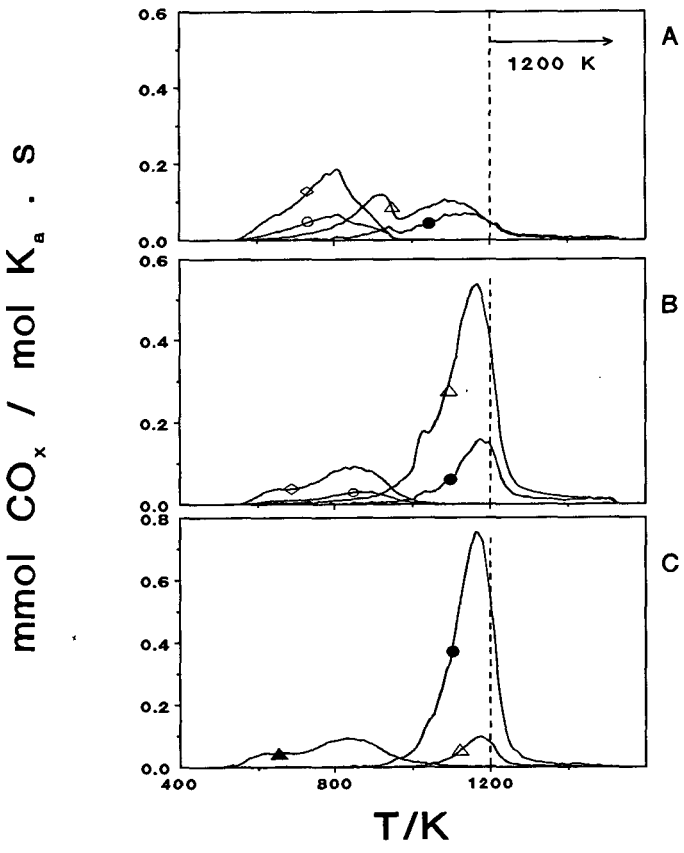

Figure 4 : TPD patterns obtained after different sample treatments:
A. $C^{18}O_2$ @ 673 K
B. $C^{18}O_2$ @ 1000 K
C. $C^{18}O_2$ @ 1000 K ⟶ CO_2 @ 1000 K (key as in figure 1)

NATURE AND STRUCTURE OF CALCIUM SPECIES DISPERSED ON CARBON: XANES AND EXAFS STUDY

Cazorla-Amorós, D., Linares-Solano, A., Salinas-Martínez de Lecea, C.
Departamento de Química Inorgánica e Ingeniería Química
Universidad de Alicante. Alicante, Spain.

Yamashita, H., Takashi, K., Tomita, A.
Institute for Chemical Reaction Science
Tohoku University. Sendai, Japan 980.

Keywords: Calcium catalyst, structure and dispersion, XANES and EXAFS.

INTRODUCTION

In a previous publication (1) the thermal behavior of calcium-carbon samples with different metal contents has been analyzed by temperature programmed desorption (TPD). The main purpose of that study was to investigate the nature and structure of calcium species dispersed on the carbon.

The most relevant aspects deduced from such study can be summarized as follow: 1) All the proton from carboxylic groups, present in the carbon surface, are ion-exchanged by Ca^{2+} ions with a 2/1 stoichiometry. 2) For calcium contents lower than the saturation of available carboxylic groups on the carbon, the ion-exchanged calcium has its coordination sphere completed with H_2O and CO_2 molecules with a coordination number of six, indicative of having an atomic distribution through the carbon matrix. 3) For high levels of calcium loading, exceeding the saturation, the ion-exchanged calcium acts as a nucleation site where crystals of calcium acetate (precursor used) grow.

TPD is not a technique which provides direct information on the structure of the analyzed species, therefore, a complementary study with an spectroscopic technique able to supply such information will be very convenient to confirm the conclusions above mentioned.

X-ray absorption fine structure spectroscopy (XAFS) has gained a great utility in the field of catalysis due to the specific information which can be obtained concerning local structure and bonds of the element examined (2-10). This technique gives information on atomic distances, coordination number and disorder degree from the interaction of the emitted electrons with the atomic environment of the absorbing atom (EXAFS) as well as information about the electronic structure and the symmetry of the atom from the multiple scattering (shape resonances) of the excited electron (XANES).

This paper presents the XANES and EXAFS results obtained with calcium-carbon samples containing different metal contents. The samples have been submitted to heat treatments at different temperatures under an inert atmosphere. The objective is to analyze the evolution of the local structure and the calcium dispersion in samples with calcium contents below and above the saturation of carboxylic groups on the carbon. The effect of pH during the ion-exchange process is also analyzed.

EXPERIMENTAL

Sample preparation was fully described in previous publications (1, 11). Briefly, a char from phenol-formaldehyde polymer resin (A) has been oxidized with HNO_3 (A2). Calcium has been introduced by

ion-exchanged with 1.5 M calcium acetate solution (the pH was not controlled) (A2-II-2.9) and at pH=10 (A2-II-4.1). Impregnation has been used to obtain other calcium contents. The impregnated samples were not washed. All calcium samples were dried at 383 K under vacuum. In the nomenclature II stands for ion-exchange and I for impregnation, and the calcium loading (wt %) is also included.

Samples have been treated in He at a flow rate of 60 ml/min at a heating rate of 20 K/min to reach different temperatures (603, 823 and 1223 K). Once the final temperature is reached, the sample is cooled down under the same atmosphere and sealed. Wafers for XAFS experiments were prepared under inert atmosphere pressing an homogeneous mixture of calcium-carbon sample and polyethylene in a ratio 2/1. Finally The samples were sealed with a polyethylene film to prevent air contact during handling.

The X-ray absorption experiments were performed at the Photon Factory in the National Laboratory for High Energy Physics (KEK-PF) Tsukuba (Japan). A Si (111) double crystal was used to monochromatize the X-ray from the 2.5-GeV electron storage ring, and the Ca K-edge absorption spectra were recorded in the transmission mode at room temperature in a range of photon energy extending from 3940 to 4720 eV. Special attention was paid to eliminate the photons from higher-order diffraction using double mirror system. Fourier Transformation was performed on k^3-weighted EXAFS oscillation, $k^3\chi(k)$, in the range of 4-10 $Å^{-1}$. The physical basis and numerous applications of XAFS spectroscopy have been discussed elsewhere (5,6,8).

RESULTS AND DISCUSSION

Reference compounds

Figure 1 presents XANES spectra and Fourier transformation of the EXAFS oscillations (FT-EXAFS) of several calcium compounds used as references. The most relevant aspects to consider are:

XANES spectra

a) Calcium oxide exhibits a pre-edge peak (I) at ≈ 4043 eV.
b) Calcium carbonate exhibits a sub-peak (II) at ≈ 4059 eV. The pre-edge peak is much less intense than in the calcium oxide.
c) Calcium acetate exhibits only one broad main peak without any sub-peak.

The pre-edge peak evolution, which is not present in the calcium acetate spectrum, is determined by the presence of different anions in the compounds: O^{2-}, CO_3^{2-}, CH_3COO^-. Differences in ionic character and symmetry originate different modification in the valence orbital of the calcium.

Fourier transform of EXAFS oscillation

A) Calcium oxide exhibits Ca-O peaks corresponding to distances ≈ 2.0 Å (uncorrected for phase shift) and Ca-Ca at ≈ 3.0 Å due to neighboring oxygen and calcium atoms respectively. Peaks appearing at higher distances correspond to Ca^{2+} and O^{2-} ions in more distant neighbor shells in the calcium oxide crystal.
B) Calcium carbonate exhibits Ca-O peaks at ≈ 1.9 Å and Ca-Ca at ≈ 3.7 Å.
C) Calcium acetate exhibits only a Ca-O peak at ≈ 2.0 Å.

Again, anions difference is the responsible of change in local atomic arrangement from one compound

to another.

Sample A2-II-2.9

Figure 2 shows the XAFS spectra (XANES and FT-EXAFS) corresponding to sample A2-II-2.9 treated at 603 K (Figure 2a, A) and 1223 K (Figure 2b, B).

According to TPD results in Figure 3 and to the interpretation given elsewhere (1), a heat treatment at 603 K does not produce carboxylic groups decomposition which occurs around 700 K. A heat treatment at 603 K only produces H_2O and CO_2 evolution. The former coming from H_2O in the carbon itself and in the coordination sphere of calcium. The second arising from CO_2 chemisorbed on calcium ion-exchanged. This interpretation is fully confirmed by XAFS results as will shall discuss now. XANES spectrum (Figure 2a) presents a broad main peak without any shoulder. FT-EXAFS oscillations exhibit only one Ca-O peak at $\approx$ 2.0 Å and no Ca-Ca peak is present. Comparing these spectra with those of reference compounds a large similarity is found with calcium acetate. This indicates that calcium is still linked to carboxylic groups at 603 K, in agreement with published results (1, 2).

The presence of a small pre-edge peak (III) in XANES spectrum (Figure 2a) indicates that coordination of oxygen atoms around calcium atom is somewhat distorted from an ideal octahedral symmetry (3, 4, 10). The evolution of H_2O and CO_2 from the coordination sphere of calcium during heat treatment at 603 K can explain this distortion.

Sample treatment at 1223 K produces important modifications in XAFS spectra. XANES spectrum (Figure 2b) shows the presence of a new pre-edge peak around 4043 eV (I) in addition to a shoulder around 4065 eV. The intensity of the pre-edge peak (III) slightly decreases in relation to that of sample treated at 603 K. FT-EXAFS spectrum (Figure 2B) presents a Ca-O peak $\approx$ 2.0 Å beside a very weak Ca-Ca peak, indicating that most of the calcium species are highly dispersed and/or forming amorphous small cluster with spectra characteristics similar to those of CaO (Figure 1 a, A) (3). These results are also in good agreement with previous results in which a high calcium dispersion was found when this sample was submitted to a similar heat treatment. Using CO_2 chemisorption the dispersion was 55 % (12).

Sample A2-II-4.1

This sample has been prepared by ion-exchange with a controlled pH of 10 unlike sample A2-II-2.9 which has been prepared by the same procedure but with the pH proper of the calcium acetate solution in contact with the carbon.

Figure 4 presents the TPD spectrum of sample A2-II-4.1. The most relevant aspect to be observed is the presence of a CO_2 peak at around 1050 K which does not appear in the TPD profile of sample A2-II-2.9 (Figure 3). This CO_2 peak presumably come from the $CaCO_3$ formed during sample preparation and not from calcium acetate, since no peak of mass 43 (characteristic of acetate) is present (1). Working at a high pH values, calcium carbonation is very probable and this will explain the above suggestion. The amount of calcium forming carbonate can be quantified from the CO_2 + 1/2 CO corresponding to this second peak. The amount obtained by this method is 0.5 wt%, therefore, the calcium ion exchanged would be 3.6 wt% which is in good agreement with the maximum calcium exchange capacity (3.5 wt%) of carbon A2 (1, 11).

XANES and FT-EXAFS spectra of sample A2-II-4.1 treated at 1223 K, appearing in Figure 5, present characteristics of CaO as in sample A2-II-2.9, but the peak intensity for the Ca-Ca peak is quite larger in the former indicating that part of the calcium is present as CaO particles with an structural order at longer range than the first coordination shell.

The disappearance of the pre-edge peak at ≈ 4040 eV indicates a smaller distortion of the calcium coordination sphere (in respect to that of sample A2-II-2.9) which again confirms the existence of a longer range order in CaO beyond the first coordination sphere. Probably, this increase in particle size from sample A2-II-2.9 to A2-II-4.1 is due to the presence of $CaCO_3$ formed during the sample preparation, as mentioned before.

Samples A2-I-6.0 and A2-I-9.4

Calcium content in these samples is larger than the maximum ion-exchange capacity of the carbon (3.5 wt%). According to the interpretation previously mentioned (1, 11), calcium in excess appears as calcium acetate crystals over the ion-exchanged one. These conclusions arise from the TPD study on these samples as well as from TG-DTA and XRD (11). TPD spectra present a peak of mass 43 at around 730 K coming from the calcium acetate decomposition and peaks of CO_2 and CO at ≈ 1030 K produced in the $CaCO_3$ decomposition (1).

To distinguish between different steps in calcium acetate decomposition, samples have been treated at different temperatures before XANES and FT-EXAFS spectra were recorded. Sample A2-I-6.0 has been treated at 823 and 1223 K, the results appear in Figure 6. Sample A2-I-9.4 has been treated at 603, 823 and 1223 K and the spectra are shown in Figure 7.

Heat treatment up to 603 K produces CO_2 and H_2O evolution from: a) the carbon (adsorbed H_2O), b) the calcium acetate (H_2O of crystallization) and c) the ion-exchanged calcium (CO_2 and H_2O coordinated). Calcium acetate remain unchanged.

From XANES and FT-EXAFS spectra similar conclusions are obtained. Figure 7 a, A shows the presence of only one broad peak in XANES spectrum and a quite intense Ca-O peak in FT-EXAFS similar to those of calcium acetate. Furthermore, the pre-edge peak (III) at ≈ 4040 eV is smaller than that for sample A2-II-2.9 treated at the same temperature (Figure 2 a, A) indicating a higher order at longer distance.

Spectra obtained after a treatment at 823 K exhibits characteristics of $CaCO_3$ in agreement with previous results (1, 11). It is interesting to observe the decrease of the pre-edge peak (at ≈4030 eV) from the spectrum of sample A2-I-6.0 to that of A2-I-9.4 which is indicative of a higher order at longer distance presents in $CaCO_3$ particle for the second sample. This observation is confirmed with the fact that Ca-Ca peak intensity is much higher for sample A2-I-9.4 than A2-I-6.0.

Finally, a heat treatment at 1223 K produces $CaCO_3$ decomposition to yield CaO (1, 11). This is also observed in Figures 6 b, B and 7 c, C. The spectra exhibit clearly the CaO characteristics. By comparison of FT-EXAFS results of samples heat treated up to 1223 K as a function of calcium content it is clear that as the calcium content increases the spectra look more similar to those of bulk calcium oxide. Therefore the CaO particle size increase in agreement with previous results (1, 11). Calcium dispersion was found to decrease from 0.55 (sample A2-II-2.9)to 0.35 (sample A2-I-9.4).

CONCLUSIONS

Sample with calcium content below the ion-exchange capacity of the carbon has, after heat treatment, most of the calcium species highly dispersed forming amorphous small cluster of CaO. Increasing pH, during ion-exchange, the calcium loading increases, however, a partial carbonation occurs leading to a particle size increase after heat treatment.

XANES and FT-EXAFS results in samples heat treated up to 1223 K clearly show that as calcium content increases the spectra look more similar to those of bulk calcium oxide indicating an increase in in CaO particle size.

XANES and FT-EXAFS study fully confirms previous conclusions obtained in the TPD study carried out in these samples.

REFERENCES

1. Linares-Solano, A., Salinas-Martínez de Lecea, C., Cazorla-Amorós, D., Joly, J. P. and Chacosset, H. Energy & Fuels **4**, 467-474 (1990).
2. Huggins, F. E.., Huffman, G. P., Lytle F. W. and Greegor, R. B. Proc. Int. Conf. Coal Science, Pittsburgh PA, USA, p.679, (1983).
3. Huggins, F. E., Huffman, G. P., Shah, N. Jenkins, R. G., Lytle, F. W. and Greegor, R. B. Fuel, **67**, 938, (1988).
4. Huggins, F. E., Shah, N., Huffman, G. P., Lytle, F. W., Greegor, R. B. and Jenkins, R. G. Fuel, **67**, 1663, (1988).
5. Sinfelt, J. H., Via, G. H. and Lytle, F. W. Catal. Rev. Sci.-Eng., **26**(1), 81, (1984).
6. Lytle, F. W., Greegor, R. B., Margnes, E. C., Biebesheimer, V. A., Sandstrom, D. R., Horsley, J. A., Via, G. H. and Sinfelt, J. H. Catalyst Characterization Science. Surface and Solid State Chemistry, Eds. M.L. Deviney y J.L. Gland, ACS, Washington, D.C., p.253, (1985).
7. Claisen, B. S., Topsøe, H., Candía, R., Villadsen, R., Lengeler, B., Als-Nielsen J. Christensen, F. J. Phys. Chem., **85**(25), 3869, (1981).
8. Chiu, N. S., Bauer S. H. and Johnson, M. F. L. J. Catal., **89**, 226, (1984).
9. Chiu, N. S., Bauer S. H. and Johnson, M. F. L. J. Catal., **98**, 32, (1986).
10. Yamashita, H. and Tomita, A. Photon Phactory Activity Report, #8, (1991).
11. Salinas-Martínez de Lecea C., Almela-Alarcón, M. and Linares-Solano, A. Fuel, **69**, 21, (1990).
12. Linares-Solano, A., Almela-Alarcón, M. and Salinas-Martínez de Lecea, C. J. Catal., **125**, 401, (1990).

ACKNOWLEDGEMENTS

The authors thank to the DGICYT (proyect PB-88-0295), to the MEC for the fellowship of D. Cazorla to travel to Tohoku University and to the Institute for Chemical Reaction Science, Tohoku University.

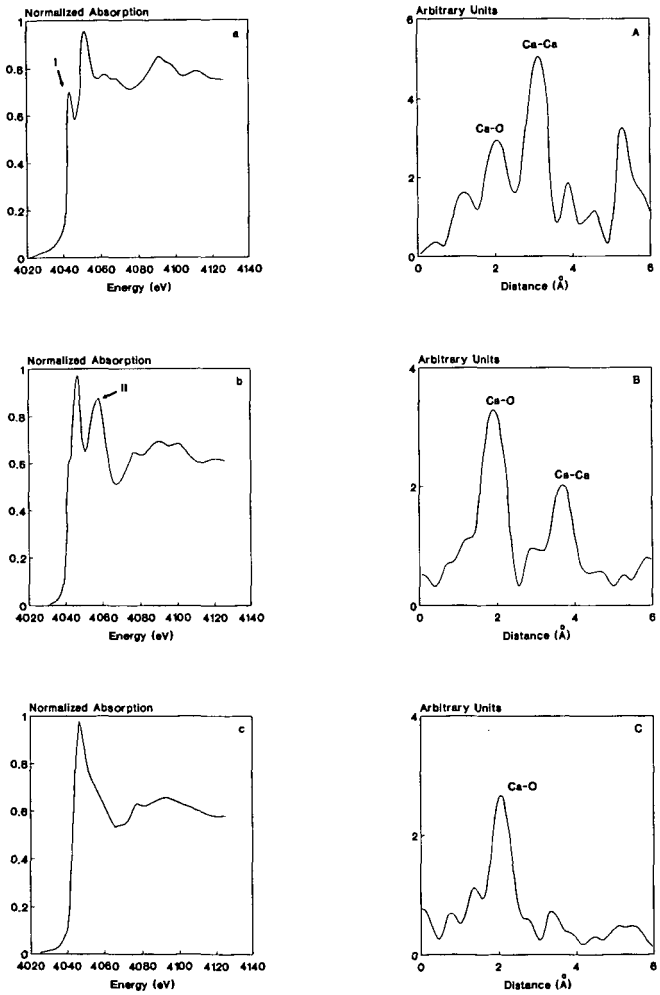

Figure 1. XANES spectra (a, b, c) and FT-EXAFS (A, B, C) of reference compounds: a, A) calcium oxide; b, B) calcium carbonate and c, C) calcium acetate.

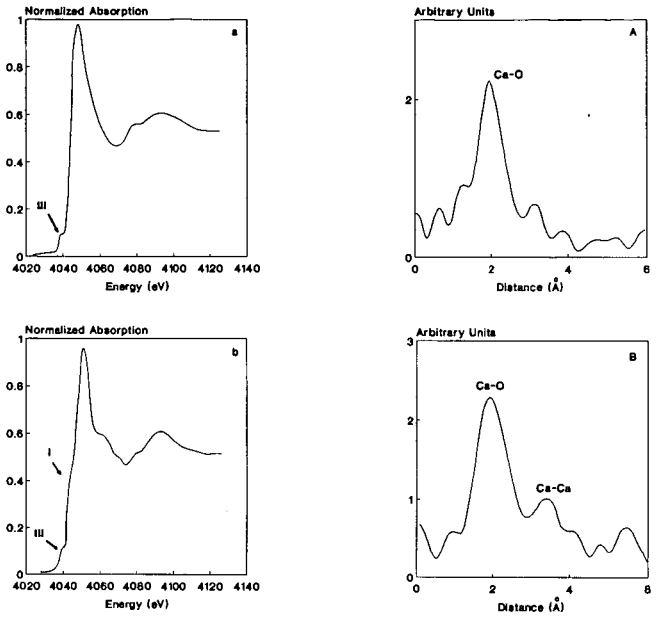

Figure 2. XANES spectra (a, b) and FT-EXAFS (A, B) of sample A2-II-2.9 after heat treatment at: a, A) 603K and b, B) 1223K.

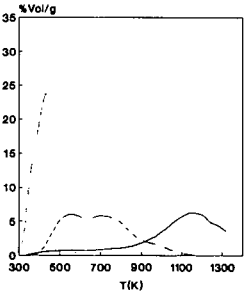

Figure 3. TPD spectrum of sample A2-II-2.9 (···, H_2O; —, CO; ---, CO_2).

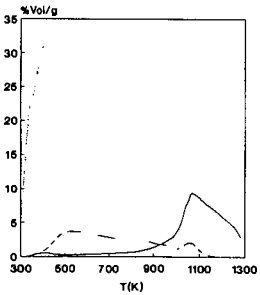

Figure 4. TPD spectrum of sample A2-II-4.1 (···, H_2O; —, CO; ---, CO_2).

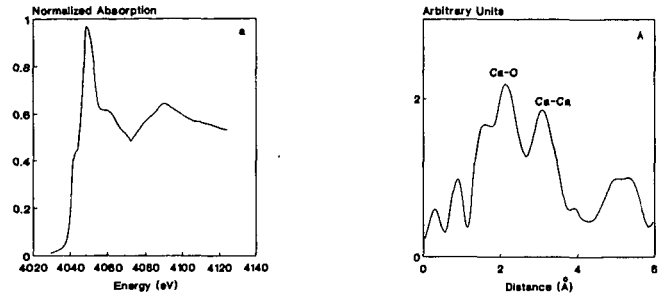

Figure 5. XANES spectra and FT-EXAFS of sample A2-II-4.1 after heat treatment at 1223 K.

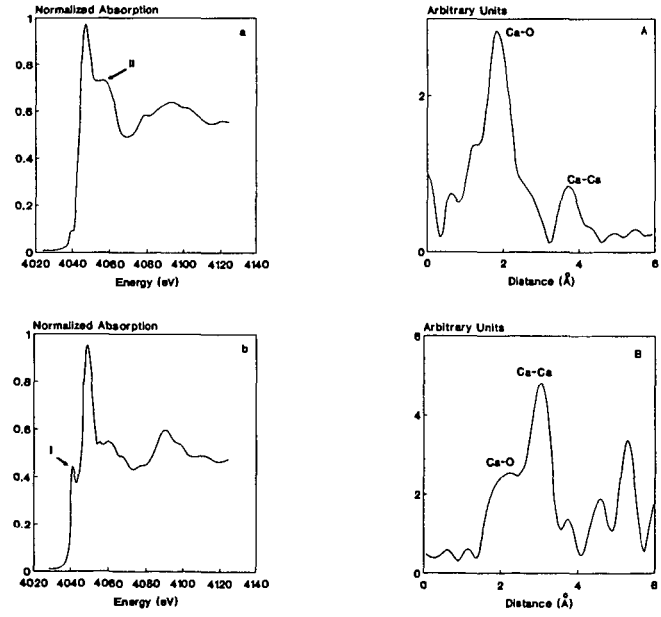

Figure 6. XANES spectra (a, b) and FT-EXAFS (A, B) of sample A2-I-6.0 after heat treatment at: a, A) 823 K and b, B) 1223 K.

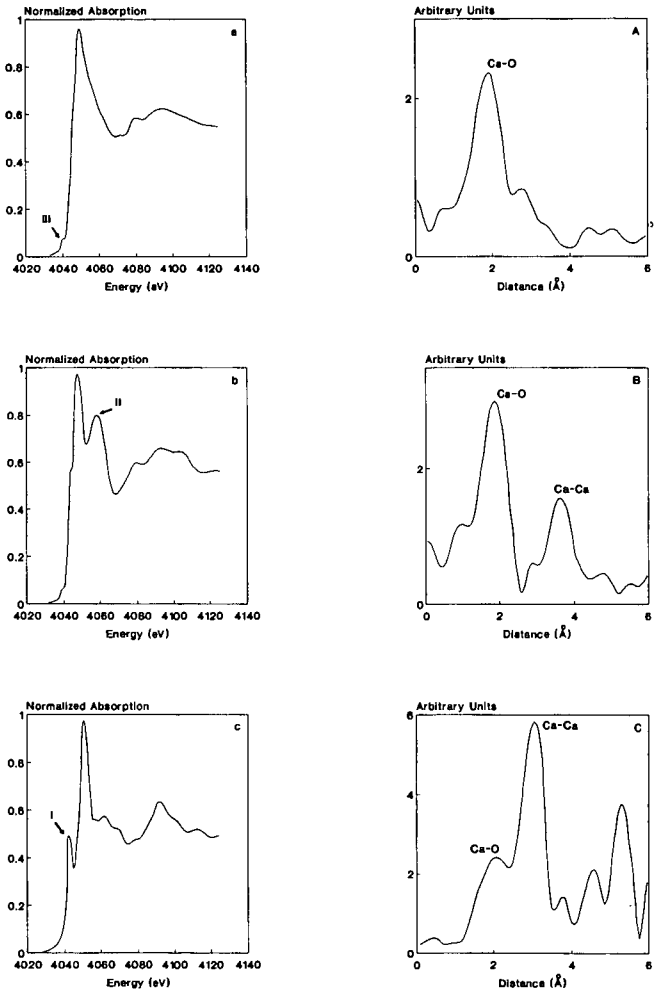

Figure 7. XANES spectra (a, b, c) and FT-EXAFS (A, B, C) of sample A2-I-9.4 after heat treatment at: a, A) 603 K; b, B) 823 K and c, C) 1223 K.

INFLUENCE OF OXYGEN FUNCTIONAL GROUPS ON THE PERFORMANCE OF CARBON-SUPPORTED CATALYSTS

C.A. Leon y Leon and L.R. Radovic

Fuel Science Program, Department of Materials Science and Engineering
The Pennsylvania State University, University Park, PA 16802

Keywords: Oxygen Functional Groups, Carbon-Supported Copper, Gasification Catalysts

INTRODUCTION

Efficient catalyst supports are materials capable of increasing the dispersion (or *percentage exposed*) of a catalyst by virtue of their physical (e.g., high surface area) and chemical (e.g., ion exchange) properties [1,2]. Numerous reports dealing with how these properties affect the performance of a variety of supported catalysts have led in many cases to improvements in their preparation [2]. The development of carbon-supported catalysts has not paralleled that of, e.g., metal oxide supports, mainly because the much richer surface chemistry of carbons complicates their characterization. Paradoxically, their rich surface chemistry makes carbons very attractive, yet poorly exploited, support materials [3]. Indeed, the open literature is very scarce in reports dealing with systematic variations of carbon properties in relation to catalyst performance [3-6]. Such variations are difficult to attain because the treatments that change the chemistry of a carbon can also change its physics, and vice versa. However, by carefully following the physical and chemical changes that accompany selected oxidative and/or thermal treatments of highly pure carbons, it has become possible to produce materials with similar oxygen content and equivalent surface areas, which nonetheless differ substantially in their specific oxygen functional group content. These supports have been loaded with a number of metals and exposed to different reaction conditions (e.g., carbon gasification in 0.1 MPa air) in order to test their performance [7]. The aim of this paper is to illustrate how the surface chemistry of carbons can be tailored to enhance the performance of carbon-supported catalysts, using the copper-catalyzed gasification of carbon as an example.

EXPERIMENTAL

Carbon Supports. For clarity, only selected results for a highly pure polymer-derived microporous carbon (Saran 928, Dow) are presented in this report; further details and results on meso- and nonporous carbons will be given elsewhere [7]. Batches of the starting material were subjected to pyrolysis (in N_2) and/or oxidation (in air, H_2O_2 or HNO_3) treatments at different conditions (i.e., different temperatures, reactant concentrations and exposure times) in order to modify their surface properties [7-9]. Changes in physical properties were followed by N_2 and CO_2 adsorption [8,9], X-ray diffraction (XRD) [8,9], and others [7], while chemical modifications were monitored via acid/base neutralizations [8-10], temperature-programmed desorption (TPD) [8,9], electrophoresis [3,8], mass titration [8] and X-ray photoelectron spectroscopy (XPS) [7,9], among others [7,11]. The three samples chosen (henceforth referred to as CA, CN and CB) were found to resemble each other the most in terms of their physical properties, while differing substantially in their surface chemistry. Samples CA, CN and CB were prepared by oxidation in boiling concentrated H_2O_2 for 15 min, oxidation in dry flowing dry air at 673 K for 3 h, and oxidation in air at 673 K for 24 h followed by pyrolysis in N_2 at 923 K for 3 h, respectively [8,11]. The active surface area, ASA (at 373 K), and the uncatalyzed gasification reactivities of each support in 0.1 MPa flowing air were measured on a modified TGA-7 apparatus (Perkin-Elmer) under diffusion-free reaction conditions [9,12].

Carbon-Supported Copper Catalysts. Samples CA, CN and CB were impregnated with aqueous (pH ca. 5.3) copper acetate (Fisher) by incipient wetness to yield 5% Cu catalysts (dry carbon basis). In addition, the adsorption capacity for Cu ammines at pH = 11.5 was determined using a Cu^{+2} ion selective electrode (Orion) coupled to a Fisher Accumet 925 pH meter [9]. The resulting catalysts were characterized by XPS, XRD and oxygen chemisorption at 373 K [12], and their gasification reactivity in 0.1 MPa air was evaluated as described above for the supports alone.

RESULTS AND DISCUSSION

Surface Chemistry and Physics of the Supports Used. Both TPD (Table 1) and ultimate analyses [7] indicated that carbons CA, CN and CB have similar oxygen contents. In all cases, the difference PZC-IEP fell within 1.6-2.3 pH units (Table 1), indicating (as discussed elsewhere [8,9]) that the external (geometric) surface of these materials is enriched in negative surface charges relative to their internal (porous) surface. However, the IEP and PZC values do not reflect the large differences in surface chemistry observed by contact angle measurements [11] or by oxygen functional group analysis (see Figure 1). Indeed, large differences in their oxygen functional group content are evidenced by their CO/CO_2 evolution ratios (mol/mol) upon TPD (Table 1). Since CO_2- and CO-evolving groups are thought to be produced primarily by the decomposition of strongly acidic (carboxyl, lactone) and weakly acidic (phenol, carbonyl) oxygen complexes [13-15], the CO/CO_2 evolution ratios can be taken as a measure of surface acidity, with lower ratios representing more strongly acidic surfaces [7,11]. Therefore, CO/CO_2 ratios have been used throughout this report as indicators of the differences in functional group quality among these samples.

Before examining Figure 1 in detail, let us consider the structural differences among samples CA, CN and CB. The corresponding changes in equivalent surface areas are shown in Figure 2. The three samples exhibited very similar N_2 isotherms at all partial pressures [7], with BET equivalent surface areas in the range 848-886 m^2/g. In a recent report dealing with Pt dispersion over an unspecified microporous carbon black and its H_2- and H_2O_2-treated derivatives, it was assumed that the observed similarity in N_2 isotherm shapes and in BET surface areas (between 895 and 956 m^2/g) indicated that differences in Pt dispersion were not related to the physical properties of the supports used, but to their oxygen functional group content [16]. Figure 2 shows that N_2 isotherms alone do not suffice to neglect any physical differences among microporous samples. Indeed, sample CA, pretreated with H_2O_2, has a significantly higher (and reproducible) Dubinin-Radushkevich (DR) surface area than that of samples CN and CB (Figure 2). Even though the actual physical meaning of equivalent surface areas of microporous materials is open to question [17,18], N_2 and CO_2 equivalent surface areas provide complementary information about the structure of a carbon [17]. Accordingly, sample CA appears to differ from samples CN and CB in that it contains a number of narrow micropores inacessible (within reasonable time) to N_2 at 77 K [17]. These narrow micropores, either generated or opened by the H_2O_2 pretreatment, are also likely to offer litlle access to hydrated metal ions in solution. Hence, for catalyst preparation purposes the accessible surface areas of samples CA, CN and CB can be taken to be of comparable magnitude [16].

In light of the above observations, it is possible to estimate the distribution of specific functional group types from the data in Figure 1 and using the following assumptions [10,13-15]:

- NaOH titrates carboxyl, lactone and phenolic groups [10];
- $NaHCO_3$ titrates carboxyl groups only [10];
- CO desorption arises from phenolic and carbonyl groups only [15]; and
- CO_2 desorption arises from carboxyl and lactone groups only [15];

The individual content of each surface group type can then be calculated from [13,15]:

- Carboxyl groups = groups titrated with $NaHCO_3$;
- Lactone groups = groups desorbed as CO_2 minus those titrated with $NaHCO_3$;
- Phenol groups = groups titrated with NaOH minus those desorbed as CO_2; and
- Carbonyl groups = groups desorbed as CO plus CO_2 minus those titrated with NaOH.

The calculated functional group contents are listed in Table 2. Because of the numerous assumptions involved in their estimates, the numbers in Table 2 must be regarded as qualitative only [13,15]. Nonetheless, Table 2 shows that the increase in surface acidity with decreasing CO/CO_2 evolution ratio is likely to be due to increases in the concentrations of both carboxyl ($pKa \approx 4.4$) and lactone ($pKa \approx 8.2$) groups [19]. The apparent absence of phenolic groups in sample CA is probably related to the diffusion-limited accessibility of NaOH to some phenol group-containing narrow micropores (Figure 2). In all cases the total oxygen coverages [20] amounted to ca. 12-17% of the N_2-BET surface areas.

Surface Chemistry vs. Uncatalyzed Carbon Gasification. Carbon supports can undergo thermal degradation when exposed to high temperatures and/or reactive environments. Because most carbons have already experienced heat treatments during their preparation, thermal degradation below, e.g., 773 K, is relatively minor in inert or reducing conditions, but can be important in oxidizing environments. Figure 3 shows the influence of oxygen functional groups on the uncatalyzed rate of gasification of the supports. The gasification reactivity of the carbon supports was found to increase with increasing surface acidity. A similar increase (ca. 20%) in active surface area, ASA [21], was also determined. (Indeed, a remarkably similar turnover frequency, or reactivity per active site, of ca. 5 s^{-1} is yielded by all supports at these conditions.) Clearly, the total surface areas (Figure 2) fail to correlate with either reactivity or ASA variations, as expected because (a) the surfaces probed by adsorbates at low temperatures ($\leq$ 298 K) are not necessarily related to the surfaces remaining at reaction conditions (i.e., after high temperature treatments), particularly if the desorbable oxygen content of the carbons is high, and (b) only a portion of the surface (the most reactive [20-23]) participates directly in the gasification process. Figure 3 suggests that the thermal treatment of surfaces rich in acidic (carboxyl, lactone) groups produces more active sites than that of surfaces rich in CO-desorbing (carbonyl, phenol) oxygen complexes. Mechanistic interpretations of Figure 3 will be addressed at length elsewhere [7].

Surface Chemistry vs. Copper Adsorption and Distribution. Metal sorption onto a support is considered necessary in order to attain a high catalyst dispersion [2,3]. Carbon materials are more flexible than most conventional (e.g., metal oxide) supports in that their surfaces can be modified to contain different kinds and amounts of surface sites [7-9], as discussed above. In an accompanying report [9] preliminary evidence suggesting the participation of lactone-type groups (in addition to carboxyl groups) to the sorption of copper by modified Saran carbons was presented. Further evidence can be gathered from Tables 1 and 2. Table 1 lists the amounts of copper taken up (primarily as Cu^{+2} ammine complexes [9]) by each support at pH = 11.5. These amounts are proportional to, but clearly exceed, the estimated carboxyl group content of each support (Table 2). Since the maximum possible stoichiometry (at equilibrium) for site-specific adsorption of divalent cations on dissociated carboxyl anions is 1:1 (i.e., $\{\text{-COO}^{-}\text{---}[Cu(NH_3)_n(H_2O)_{6-n}]^{+2}\text{---}(OH)^{-}\}$; $1 \leq n \leq 5$), carboxyl groups alone cannot accomodate all the adsorbed copper. Oxygen functional groups with intermediate (lactone-type) or lower (phenolic-type, pKa $\approx$ 10 [19]) acid strength could also serve as adsorption sites. If both lactone and carboxyl groups participated in the copper adsorption process, at equilibrium a constant Cu/CO_2 ratio could be expected, with Cu/CO_2 = 1 resulting from a either 1:1 exchange or the decomposition of adjacent carboxyl sites [9,10,24], and $Cu/CO_2 \approx 0.5$ resulting from a 1:2 exchange on adjacent sites [10]. Similar arguments can be raised about the Cu/NaOH ratio, if carboxyl, lactone and phenol groups participated simultaneously in the adsorption process. As shown in Table 1 and elsewhere [9] the Cu/CO_2 ratios for modified Saran chars fluctuate between 0.32 and 0.87, with values > 0.5 corresponding to air- (vs. liquid phase-) oxidized carbons. Cu/NaOH ratios, on the other hand, are in some instances very low (see Table 1; the exception, i.e., that of sample CA, is again related to the limited accessibility of NaOH to some of its phenol group-containing narrow micropores, as mentioned earlier). These data can be understood by postulating that copper cations interact with oxygen complexes on carbons in order of decreasing acidity, i.e., carboxyl > lactone > phenol. Once most accessible dissociated carboxyl groups are populated, additional copper cations begin to adsorb onto dissociated lactones and, subsequently, onto dissociated phenol groups. (The transition between each group range is not sharp but rather smooth, judging from the corresponding copper adsorption isotherms [7,9].) Table 1 suggests that both carboxyl and lactone groups participate in Cu^{+2} ammine adsorption at pH = 11.5, giving Cu/CO_2 ratios close to 0.5, i.e., one divalent cation for every two negatively charged groups (or $Cu/CO_2 > 0.5$ for surfaces presumably containing some isolated sites). Phenol groups appear to contribute little towards copper adsorption at these conditions. For samples CA, CN and CB, copper saturation uptakes of ca. 2.0, 1.1 and 0.3 wt.% were determined, indicating that it is not the total oxygen content of a carbon (Table 1) but its quality (Table 2) that controls the cation adsorption process.

Drying the samples containing an excess (5 wt.%) Cu leaves in all cases well dispersed metal precursors; these yield no copper XRD patterns and block a portion of the micropores, since the BET and DR surface areas decrease upon loading by ca. 60 % and 30-50 %, respectively [7]. Figure 4 shows that the XPS ratios of the dried samples approach in all cases that of the salt (acetate) used for their preparation. The most significant difference among the dried samples was an upwards shift in

binding energy with increasing support acidity (Table 1). (In agreement with this, higher Cu loadings of nonacidic carbons were found to produce XRD patterns consistent with the formation of Cu^{+1} species [25].) Unsurprisingly, sintering the catalysts (in N_2 at 623 K) reduced the Cu/C XPS ratios to values ca. 5 times higher than bulk catalyst values (Figure 4), suggesting a significant external surface enrichment by Cu in all cases. In spite of this external surface enrichment by Cu, the dispersion (or fraction exposed) of Cu on each catalyst was estimated to be relatively high, and to go through an apparent maximum for carbons of intermediate surface acidity (Figure 5). Figure 5 suggests that maximizing Cu adsorption (Table 1) does not necessarily lead to the highest Cu dispersion; indeed, as discussed below the thermal stability of the adsorbed complex must also be taken into consideration.

Influence of Surface Functional Groups on the Copper-Catalyzed Gasification of Carbon. Besides promoting a high and stable initial catalyst dispersion, oxygen functional groups can affect the sintering behaviour, the degree of reduction, the volatility, etc., of a supported metal. In the case of the catalyzed gasification of carbon, the support itself is a reactant, and the oxygen complexes are deemed to participate as reaction intermediates. Since Cu-catalyzed gasification rates exceed uncatalyzed rates by 10^2-10^3 [9], the initial surface chemistry of the support (Figure 3) has little bearing on the former other than its influence on the state of the catalyst at reaction conditions. Figure 6 shows that for low sintering temperatures the most active catalyst is the one with the highest Cu dispersion (Figure 5). In contrast, after sintering the catalysts at $\geq$ 923 K the most acidic supports provided the highest reactivity. Hence, the most adequate surface chemistry for Cu/C catalysts is seen to depend strongly on the conditions of its utilization. Sintering up to 923 K, which causes primarily the decomposition of CO_2-evolving groups [8], is accompanied by a drastic drop in reactivity, in particular for the least acidic carbons (Figure 7). Further sintering up to 1223 K, which parallels the desorption of CO-evolving groups [8], causes minor losses in reactivity, in particular for the most acidic carbons, whose small Cu particles are only then free to migrate and lose dispersion by their coalescence.

CONCLUSIONS

Oxygen functional groups influence virtually all stages of utilization of carbon-supported catalysts. The importance of the surface chemistry of carbon supports is strongly dependent on the end use of the catalyst. More than the quantity of oxygen it is the quality (type) of oxygen groups that controls the extent of metal precursor sorption, its distribution throughout the support, the resistance to active phase agglomeration upon drying/reduction, and ultimately the performance of carbon-supported catalysts.

REFERENCES

1. M. Boudart and G. Djega-Mariadassou, in "Kinetics of Heterogeneous Catalytic Reactions," Princeton University Press, Princeton (1984), Ch. 6.
2. J.R. Anderson, "Structure of Metallic Catalysts," Academic Press, New York (1975), Ch. 2.
3. J.M. Solar, C.A. Leon y Leon, K. Osseo-Asare and L.R. Radovic, *Carbon* **28**, 369 (1990).
4. A.J. Bird, in "Catalyst Supports and Supported Catalysts" (A.B. Stiles, Ed.), Butterworths, London (1987), Ch. 5.
5. H. Jungten, *Fuel* **65**, 1436 (1986).
6. P. Ehrburger, *Adv. Colloid Interface Sci.* **21**, 275 (1984).
7. C.A. Leon y Leon and L.R. Radovic, in preparation.
8. C.A. Leon y Leon, J.M. Solar, V. Calemma, K. Osseo-Asare and L.R. Radovic, *Carbon*, Submitted (1991).
9. C.A. Leon y Leon and L.R. Radovic, "Effect of Thermal and Chemical Pretreatments on the Copper-Catalyzed Gasification of Carbon in Air," ACS Preprints, Div. Fuel Chem., New York (1991), in print.
10. (a) H.P. Boehm, E. Diehl, W. Heck and R. Sappok, *Angew. Chem. Internat. Edit.* **3**, 669 (1964); (b) H.P. Boehm, *Advan. Catal.* **16**, 179 (1966).
11. C.A. Leon y Leon, V. Calemma and L.R. Radovic, "Surface Chemical Heterogeneity of Oxidized Carbon Particles," 20th Biennial Conf. on Carbon, Santa Barbara, CA, June 23-28, 1991, p. 30.
12. C.A. Leon y Leon and L.R. Radovic, Proc. Int. Carbon Conf., Paris, France (1990), p. 44.
13. K. Kinoshita, in "Carbon: Electrochemical and Physicochemical Properties," Wiley, New York (1988), Ch. 3.
14. B.R. Puri, in "Chemistry and Physics of Carbon" (P.L. Walker, Jr., Ed.), Vol. 6, Dekker, New York (1970), p. 191.
15. D. Rivin, *Rubber Chem. Technol.* **44**, 307 (1973).
16. C. Prado-Burguete, A. Linares-Solano, F. Rodriguez-Reinoso and C. Salinas-Martinez de Lecea, *J. Catal.* **115**, 98 (1989).
17. F. Rodriguez-Reinoso and A. Linares-Solano, in "Chemistry and Physics of Carbon" (Edited by P.A. Thrower), Vol. 21, Marcel Dekker, New York (1989), p. 1.
18. H. Marsh, *Carbon* **25**, 49 (1987).

19. J.S. Mattson and H.B. Mark, Jr., "Activated Carbon," Marcel Dekker, New York (1971), p. 41.
20. N.R. Laine, F.J. Vastola and P.L. Walker, Jr., *J. Phys. Chem.* **67**, 2030 (1963).
21. I.M.K. Ismail and P.L. Walker, Jr., *Carbon* **27**, 549 (1989).
22. L.R. Radovic, A.A. Lizzio and H. Jiang, in "Fundamental Issues in Control of Carbon Gasification Reactivity" (J. Lahaye and P. Ehrburger, Eds.), Kluwer, the Netherlands (1991), p. 235.
23. G.R. Hennig, in "Proceedings of the 5th Conference on Carbon," Vol. I, Pergamon Press, New York (1962), p. 143.
24. A. Linares-Solano, C. Salinas-Martinez de Lecea and D. Cazorla-Amoros, *Energy & Fuels* **4**, 469 (1990).
25. P. Ehrburger, J.M. Henlin and J. Lahaye, *J. Catal.* **100**, 429 (1986).

Table 1. Features of Modified Saran Carbons Used as Cu Catalyst Supports.

Sample	%O [wt.]	CO/CO_2[a] [mol/mol]	IEP[b]	PZC[b]	B.E.[c] [eV]	Cu ads.[d] [mmol/g]	Cu/CO_2[e] [mol/mol]	Cu/NaOH[e] [mol/mol]
CA	5.0	2.18	3.85	5.74	934.7	0.32	0.43	1.24
CN	4.5	7.29	3.65	5.23	933.7	0.17	0.58	0.14
CB	3.3	13.9	5.25	7.53	932.8	0.04	0.32	0.05

[a] CO/CO_2 evolution ratio upon TPD.
[b] IEP: isoelectric point (by electrophoresis); PZC: point of zero charge (by mass titration).
[c] B.E.: XPS copper $2p_{3/2}$ peak binding energy (freshly dried catalysts).
[d] Amount of copper withdrawn from solution at pH=11.5 (adjusted using NH_4OH).
[e] Ratio of Cu adsorbed to CO_2 evolved (TPD) and acidic groups titrated with NaOH.

Table 2. Estimated Functional Group Content of Modified Saran Carbons.

Sample	Carboxyl		Lactone		Phenol		Carbonyl	
	[mmol/g]	%	[mmol/g]	%	[mmol/g]	%	[mmol/g]	%
CA	0.23	11	0.52	24	0	0	1.37	65
CN	0.05	2	0.25	11	0.96	44	0.93	43
CB	0.01	1	0.12	7	0.69	38	0.99	54

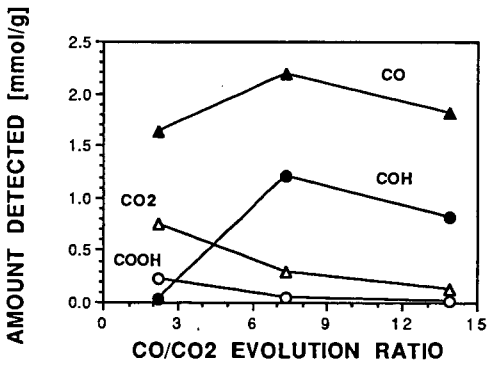

Figure 1. Variation in Oxygen Functional Group Content with CO/CO_2 Evolution Ratio (upon TPD) of Modified Saran Carbons. Triangles: amounts of CO_2 (**CO2**, or carboxyl plus lactone [15]) and of CO (**CO**, or phenol plus carbonyl) evolved upon TPD; Circles: amounts of acidic groups titrated using $NaHCO_3$ (**COOH**, or carboxyl [10]) and NaOH minus $NaHCO_3$ (**COH**, or lactone plus phenol [10]).

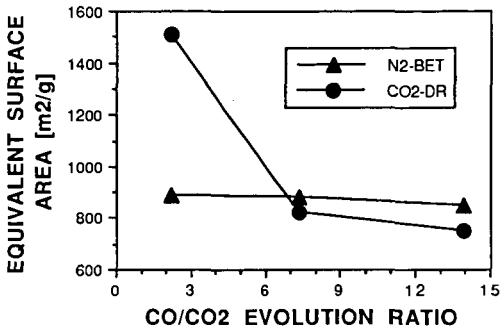

Figure 2. Equivalent Surface Areas of Modified Saran Carbons, Estimated From Volumetric N_2 (77 K) and CO_2 (298 K) Adsorption Isotherms Using the BET and Dubinin-Radushkevich (DR) Equations, respectively.

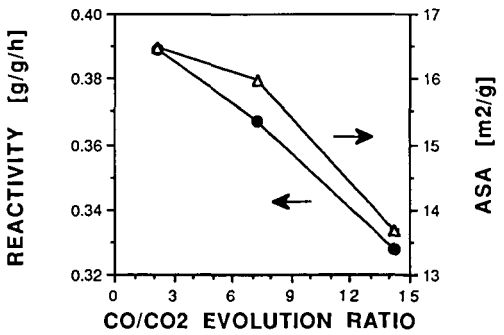

Figure 3. Influence of Oxygen Functional Groups on the Uncatalyzed Gasification Reactivity (773 K, 0.1 MPa air) and on the Active Surface Area, ASA (373 K), of Modified Saran Carbons.

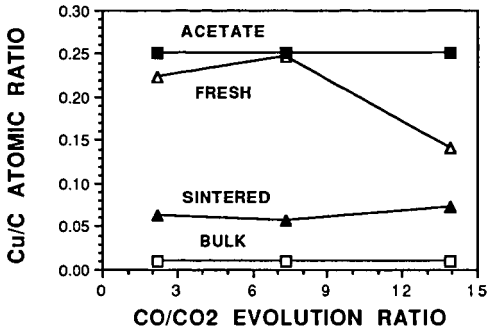

Figure 4. Comparison of Copper-to-Carbon XPS Ratios of Dried and of Sintered (in N_2 at 623 K) 5% Cu/Saran Catalysts With Those of the Precursor Salt (Acetate) and the Bulk Catalysts.

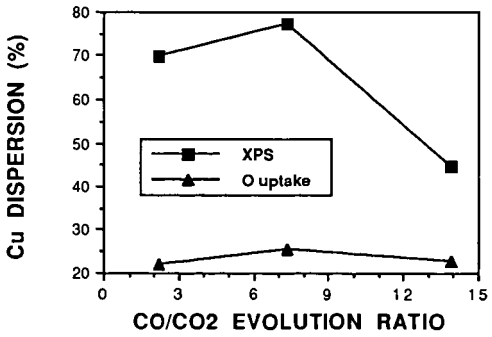

Figure 5. Copper Dispersion Over Modified Saran Carbons After Sintering 5% Cu/Support Catalysts in N_2 at 623 K, Estimated From XPS and Oxygen Chemisorption Data.

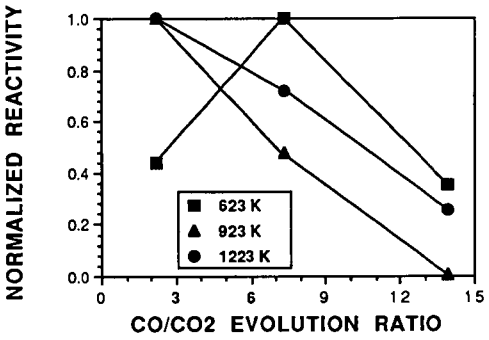

Figure 6. Influence of Carbon Surface Chemistry on the Normalized Gasification Reactivity (in 0.1 MPa air, Extrapolated to 623 K) of 5% Cu/Saran Catalysts Following Heat Pretreatments (in N_2) at Temperatures Shown.

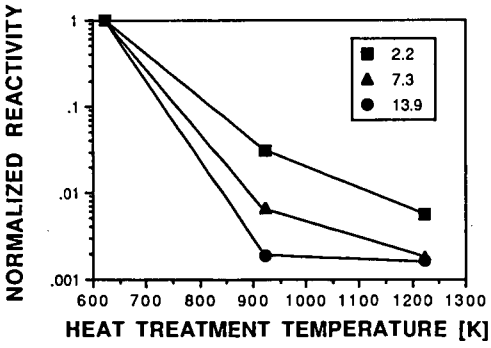

Figure 7. Effect of Heat Pretreatment on the Normalized Gasification Reactivity (in 0.1 MPa air, Extrapolated to 623 K) of 5% Cu/Saran Catalysts for Different Initial Surface Chemistry.